ISSN 0503-1540

Tome 20 *Août* *1982* Numéro 3

La mer

うみ

昭和 57 年 8 月

日 仏 海 洋 学 会

La Société franco-japonaise
d'océanographie
Tokyo, Japon

日仏海洋学会

編集委員会

投稿規定

1. 報文の投稿者は本会会員に限る。
2. 原稿は簡潔にわかりやすく書き，図表を含めて印刷ページで**10ページ以内**を原則とする。原稿（正**1通**，副**1通**）は，（〒101）東京都千代田区神田駿河台2-3　日仏会館内　日仏海洋学会編集委員会宛に送ること。
3. 編集委員会は，事情により原稿の字句の加除訂正を行うことがある。
4. 論文（欧文，和文とも）には必ず約200語の欧文（原則として仏語）の要旨をつけること。欧文論文には欧文の要旨のほかに必ず約500字の和文の要旨をつけること。
5. 図及び表は必要なもののみに限る。図はそのまま版下になるように縮尺を考慮して鮮明に黒インクで書き，論文の図及び表には必ず英文（又は仏文）の説明をつけること。
6. 初校は原則として著者が行う。
7. 報文には1編につき50部の別刷を無料で著者に進呈する。これ以上の部数に対しては，実費（送料を含む）を著者が負担する。

RECOMMANDATIONS A L'USAGE DES AUTEURS

1. Les auteurs doivent être des membres de la Société franco-japonaise d'océanographie.
2. Les notes ne peuvent dépasser dix pages. Les manuscrits à deux exemplaires, dactylographiés sur papier fort, doivent être envoyés au Comité de rédaction de la Société franco-japonaise d'océanographie, c/o Maison franco-japonaise, 2-3, Kanda Surugadai, Chiyoda-ku, Tokyo, 101 Japon.
3. Le Comité de rédaction se réserve le droit d'apporter, le cas échéant, des modifications mineuses aux manuscrits ainsi que de demander aux auteurs de les corriger.
4. Des résumés en langue japonaise ou langue française sont obligatoires.
5. Les figures au trait seront tracées à l'encre de Chine noire sur papier blanc ou sur calque. Les légendes des figures et des tableaux sont indispensables.
6. Les premières épreuves seront corrigées, en principe, par les auteurs.
7. Un tirage à part des articles en cinquante exemplaires est offert gratuitement aux auteurs. Ceux qui en désirent un plus grand nombre peuvent les faire établir à leurs frais.

La mer 20: 131-135, 1982
Société franco-japonaise d'océanographie, Tokyo

A Single Layer Model of the Continental Shelf Circulation in the East China Sea*

Yaochu YUAN**, Jilan SU** and Jingsan ZHAO**

Abstract: A vertically integrated model including the baroclinic effect is proposed to study the circulation. Both winter and summer circulations for two areas in the East China Sea are computed. Numerical computations yield realistic patterns for both circulations. It is concluded that: 1) the vertically integrated model with constant density gives better results for the winter circulation than for the summer circulation when the baroclinic effect is not negligible, 2) the primary driving force of the winter circulation is a prevailing northerly wind field, and 3) the turning and spreading of the Chang Jiang outflow is due to combined effects of the wind field, topography, and baroclinicity, whereas the Taiwan current seems to exert its influence mainly through changing the baroclinic field. In addition, the mechanisms which cause the northward flowing Huang Hai warm current are also analyzed.

1. Introduction

Problems of the current of the East China Sea have been studied by a number of physical oceanographers. GUAN (1957) analyzed the relation between the surface current and the wind fields and presented the properties of the surface current in the China Coast. GUAN (1962) discussed some of the difficulties encountered on the study of the current structure of the near-shore area of the China Sea, and further tried to offer some reasonable explanations to these questions. The properties of the current of the near-shore area of the China Sea are reanalyzed on the basis of his previous works. MAO *et al.* (1963) studied the distributions and variations of the Chang Jiang diluted water and its mixing processes on the basis of the hydrographic data of the area off the mouth of the Chang Jiang River. INOUE (1975) analyzed the general pattern of the bottom current on the continental shelf of the East China Sea. The currents in the East China Sea were analyzed on the basis of the investigation of the drifting paths of current bottles and data obtained by the electro-magnetic current meter (KONDO and TAMAI, 1975).

The aim of this paper is to study the paths by which the Chang Jiang outflow travels through the East China Sea. A vertically integrated model including the baroclinic effect is proposed to study the circulation. Actual topography is used. The area considered ranges from 28°N to 37°30'N or 34°N in the north-south direction. It is bounded on the west by the Chinese coast and on the east by either the Korean coast or the 127°E longitude. Input along the boundary includes: 1) net discharges from both Chang Jiang and Qiantang Jiang; 2) Korean, Huang Hai, and Zhejiang nearshore currents; 3) the Kuroshio, Taiwan warm current and Huang Hai warm current. For the summer circulation the effect of the Huang Hai cold water is also modeled.

Numerical computations yield realistic patterns for both summer and winter circulations. In the winter circulation, the flow pattern is produced by the combined effect of the topography and prevailing northerly wind field. In the summer circulation, the turning and spreading of the Chang Jiang outflow is due to combined effect of wind field, topography, and baroclinicity, whereas the Taiwan current seems to exert its influence mainly through changing the baroclinic field. In addition, the mechanisms which cause the Huang Hai warm current are also analyzed for both summer and winter.

* Received August 31, 1981
Presented at the First JECSS Workshop, June 1981 (cf. La mer **20**: 37-40, 1982).
** Second Institute of Oceanography, National Bureau of Oceanography, Hangzhou, China

2. Governing Equations

The circulation is asumed to be steady, and the integrated forms of momentum and continuity equations are

$$f\vec{k}\times\vec{U}=-g\nabla(\zeta+\zeta_a)-\vec{R}+\frac{1}{\rho H}(\vec{\tau}_w-\vec{\tau}_b),$$
$$\nabla\cdot(H\vec{U})=0, \quad (1)$$

where $\vec{U}$ is the average velocity vector given by

$$\vec{U}=\left(\frac{1}{H}\int_{-H}^{0}u\,dz,\ \frac{1}{H}\int_{-H}^{0}v\,dz\right). \quad (2)$$

$\vec{R}$ is

$$\vec{R}=\left(\frac{g}{\rho H}\int_{-H}^{0}dz\int_{z}^{0}\frac{\partial\rho}{\partial x}\,dz,\ \frac{g}{\rho H}\int_{-H}^{0}dz\int_{z}^{0}\frac{\partial\rho}{\partial y}\,dz\right). \quad (3)$$

∇ is the horizontal gradient operator in a right-hand Cartesian coordinate system with the z axis directed opposite to $\vec{g}$, g stands for the gravitational acceleration, f is the Coriolis parameter, $\vec{k}$ is the unit vector in the z-direction, ρ is the density, H represents the water depth, ζ is the free surface elevation, ζ_a is the atmospheric pressure divided by ρg, $\vec{\tau}_w$ stands for the wind stress vector, and $\vec{\tau}_b$ stands for the bottom stress vector.

We assume that $\vec{\tau}_b$ satisfies a quasi-linear model:

$$\vec{\tau}_b=\rho B\vec{U}, \quad (4)$$

in which $B=b/H$, b is a resistance coefficient.

By (1), we may introduce the stream function ψ:

$$\vec{U}=-\frac{1}{H}\vec{k}\times\nabla\psi. \quad (5)$$

By the preceding equations, we may obtain the equation for the stream function ψ:

$$\frac{\partial}{\partial x}\left(\frac{b}{H^3}\frac{\partial\psi}{\partial x}\right)+\frac{\partial}{\partial y}\left(\frac{b}{H^3}\frac{\partial\psi}{\partial y}\right)+f\left(\frac{1}{H^2}\frac{\partial H}{\partial x}\frac{\partial\psi}{\partial y}-\frac{1}{H^2}\frac{\partial H}{\partial y}\frac{\partial\psi}{\partial x}\right)=\frac{\partial}{\partial y}\left(\frac{1}{H}\frac{\tau_{wx}}{\rho}\right)-\frac{\partial}{\partial x}\left(\frac{1}{H}\frac{\tau_{wy}}{\rho}\right)+F, \quad (6)$$

in which

$$F=\frac{g}{\rho}\frac{1}{H^2}\left(\frac{\partial H}{\partial y}\int_{-H}^{0}z\frac{\partial\rho}{\partial x}dz-\frac{\partial H}{\partial x}\int_{-H}^{0}z\frac{\partial\rho}{\partial y}dz\right). \quad (7)$$

In the right-hand side of (6), the first term stands for the interaction effect of the topography and the wind stress, and the second term stands for the interaction effect of the topography and baroclinicity. It is clear that if the density gradient diverts to the right side of the gradient of the water depth, then it produces a torque which in turn produces positive vorticity in the flow, and vice versa.

For the boundary conditions, we require that $\psi=$const. at the coast and specify the net discharges for Chang Jiang and Qiantang Jiang. At the open boundaries the values for ψ may be determined by referring to some summer and winter data. It should be noted that the mass flux through all the boundaries satisfies the continuity condition.

3. Computational Results and Conclusions

The computational results are shown in Figures 1 to 9.

Numerical computations yield realistic patterns for both summer and winter circulations. The following conclusions are obtained.

The vertically integrated model with constant density gives better results for the winter circulation than for the summer circulation where baroclinic effect is not negligible.

The primary driving force of the winter circulation is the prevailing northerly wind field and the flow pattern is produced by the combined effect of the topography and the wind field. The Chang Jiang plume flows southward due to the prevailing northerly wind field. The northern part of the East China Sea is a semi-enclosed basin. Therefore, under a northerly wind a flow pattern similar to that in an enclosed basin such as a lake is produced, namely, two opposite gyres separated by flows opposing the wind in between. Because of the topographic effect, the western gyre is stronger than the eastern gyre and the northward flowing current,

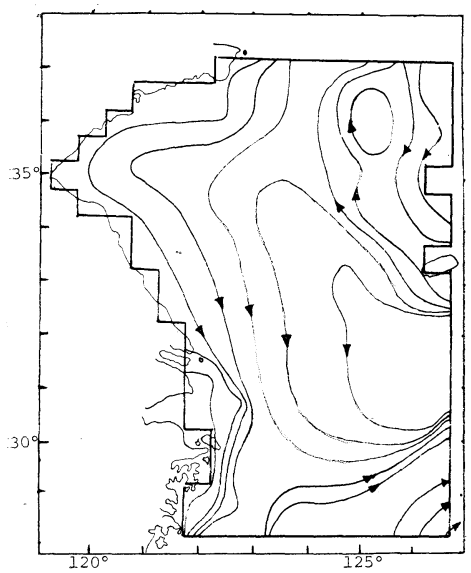

Fig. 1. Winter circulation, NW wind (9 m/sec), actual topography, no baroclinic effect, $k=7.5$ ($k=b/A_v$, A_v is the vertical kinematic eddy viscosity coefficient).

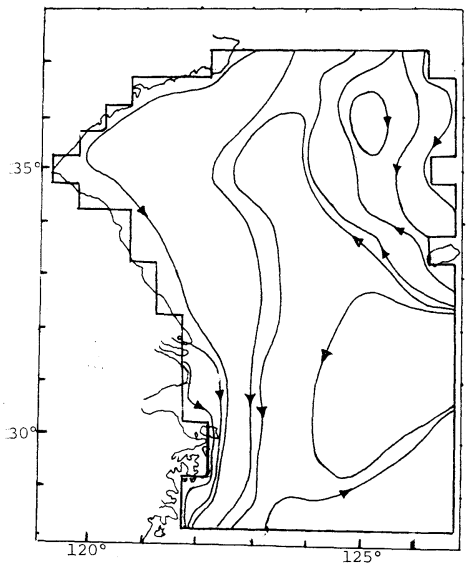

Fig. 2. Winter circulation, N wind (9 m/sec), actual topography, no baroclinic effect, $k=7.5$.

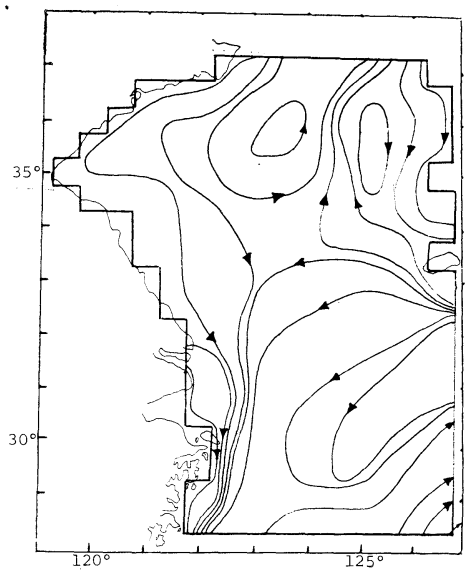

Fig. 3. Winter circulation, NE wind (9 m/sec), actual topography, no baroclinic effect, $k=7.5$.

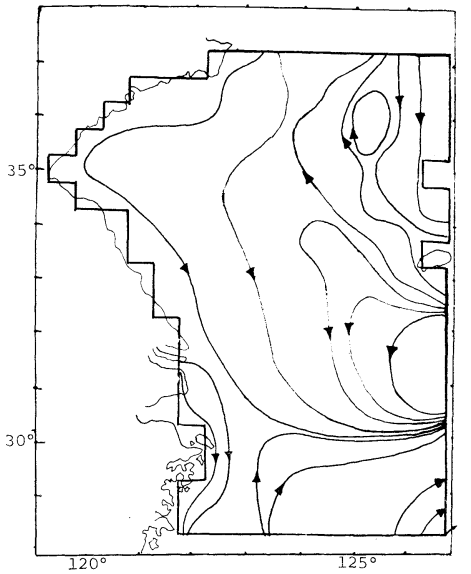

Fig. 4. Winter circulation, NW wind (9 m/sec), actual topography, no baroclinic effect, $k=15$.

the Huang Hai warm current, is located on the eastern part of the basin. In addition, the baroclinic effect also favors the northward penetration of the Huang Hai warm current. Because the density gradient diverts to the left side of the gradient of the water depth, it produces a torque which results in a clockwise flow.

In the summer circulation, the turning of the Chang Jiang outflow is due to combined effects of the wind field, topography, and baroclinicity.

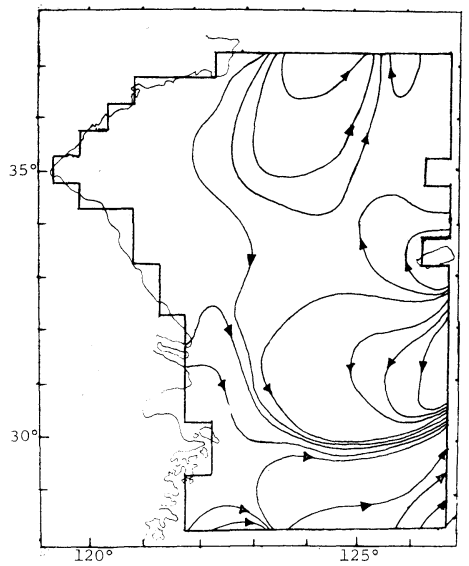

Fig. 5. Winter circulation, $\vec{\tau_w}=0$. Others as in Fig. 1.

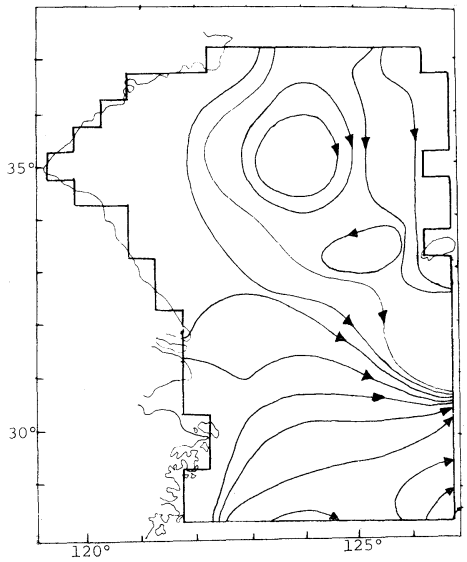

Fig. 6. Summer circulation, SW wind (6m/sec), actual topography. The Huang Hai cold water is modeled (modeling area: 34°15′N-36°15′N, 122°45′E-124°45′E). Wind speed (6 m/sec), no baroclinic effect in other areas, $k=15$.

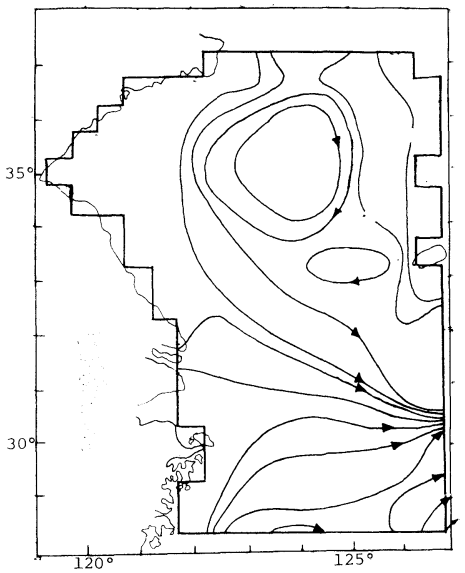

Fig. 7. Summer circulation, $k=7.5$. Others as in Fig. 6.

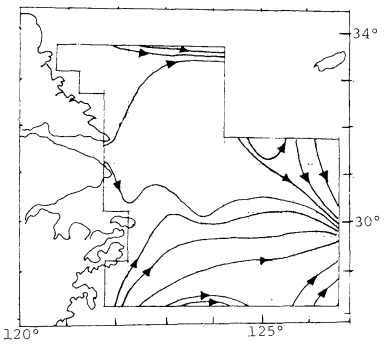

Fig. 8. Summer circulation. The baroclinic effect is considered (T. S. data in June 1977). SE wind (6 m/sec), actual topography, $k=15$.

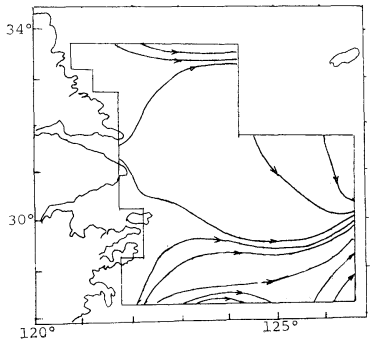

Fig. 9. Summer circulation. No baroclinic effect. Others as in Fig. 8.

From actual data, in the near-shore section the density gradient diverts to the right of the gradient of the water depth, and produces a torque generating a counterclockwise flow. The spreading of the Chang Jiang outflow depends on four factors, namely; 1) the wind field, 2) the interaction of the topography and baroclinicity, 3) the net discharge of Chang Jiang and the strength of the Taiwan warm current, which seem to exert their influence mainly through changing the baroclinic field, and 4) the strength of the cyclonic circulation in Huang Hai. We also find that the mechanisms which make the Huang Hai warm current flowing northward in summer are, 1) the existence of the cold water in the north, which induces a cyclonic circulation, 2) the combined effect of the topography and baroclinicity which is also present in the winter.

References

GUAN, B.-X. (1957): A preliminary study of the relation of the surface current and the wind fields in the China Coast. Oceanol. Limnol. Sinica, **1**, 95-115.

GUAN, B.-X. (1962): Some problems concerning the study of the current structure of the near-shore area of the China Sea. Oceanol. Limnol. Sinica, **4**, 121-141.

INOUE, N. (1975): Bottom current on the continental shelf of the East China Sea. Mar. Sci., **7**, 12-18.

KONDO, M. and K. TAMAI (1975): On the currents in the East China Sea. Mar. Sci., **7**, 27-33.

MAO, H., GAN, Z. and LAI, S. (1963): A preliminary study of the Chang Jiang diluted water and its mixing processes. Oceanol. Limnol. Sinica, **5**, 183-206.

東シナ海の大陸棚上の海水循環に関する一層モデル

Yaochu YUAN, Jilan SU and Jingsan ZHAO

要旨: 傾圧効果をもたせながら運動方程式を鉛直方向に積分した二次元モデルで，東シナ海の大陸棚上の循環を調べた。夏と冬についての計算結果は，どちらも観測結果とかなりよく合う。密度が一定とした計算では，冬のほうがよく合う。夏は傾圧効果が大きくなるからである。冬の循環を駆動するおもな力は北風である。長江からの川の水のひろがりは，風と地形と傾圧性の総合的効果によってきまる。台湾海流のおもな影響は，傾圧場を変えることである。さらに，黄海暖流が北に流れる機構も解析した。

La mer 20: 136-140, 1982
Société franco-japonaise d'océanographie, Tokyo

The Calculation of Three-Dimensional Ocean Current by Finite Element Method*

Yaochu YUAN** and Kulrong HE**

Abstract: The present method is a development of a paper "Application of finite element method to the calculation of the Kuroshio Current in the eastern area of Taiwan". Starting from equations of motion including the pressure gradients, the Coriolis force and the friction due to the vertical eddy viscosity, we obtain a solution of the velocity components as well as the surface elevation.

1. Introduction

In recent years, applications of finite element method to problems in fluid mechanics and physical oceanography have been reported (ODEN *et al.*, 1974; GALLAGHER *et al.*, 1975; PLATZMAN, 1978). We presented a paper (YUAN *et al.*, 1980) "Application of the finite element method to the calculation of the Kuroshio Current in the eastern area of Taiwan". The present method is a development of that paper. We consider the wind stress, frictional force due to vertical turbulent motion, pressure gradient, Coriolis force, gravitational force. We obtain an approximate solution of the velocity components u and v, while the surface elevation ζ is solved by finite element method. We have computed the Kuroshio Current in the eastern area of Taiwan, with $A_z=1$, 10, 100, 300 (g/cm/sec), wind velocity $V_w=5$ m/sec. The computational results show that the current due to the density gradient is predominant in this computational area.

2. Basic Equations and Solution

After the above references to the various forces, in a right-hand cartesian coordinate system with the z axis directed opposite to g, the basic equations can be given by

$$\left.\begin{aligned} A_z\frac{\partial^2 u}{\partial z^2}+f\rho v&=\frac{\partial p}{\partial x},\\ A_z\frac{\partial^2 v}{\partial z^2}-f\rho u&=\frac{\partial p}{\partial y},\\ -\rho g&=\frac{\partial p}{\partial z},\\ \frac{\partial u}{\partial x}+\frac{\partial v}{\partial y}+\frac{\partial w}{\partial z}&=0, \end{aligned}\right\} \quad (1)$$

and the boundary conditions:

$$\left.\begin{aligned} Z=\zeta:\quad A_z\frac{\partial u}{\partial z}&=T_x,\\ A_z\frac{\partial v}{\partial z}&=T_y,\\ Z=H:\quad u=v&=0. \end{aligned}\right\} \quad (2)$$

We can obtain the exact solution of the velocity components u and v. They are:

$$\left.\begin{aligned} u=&\frac{(T_x-T_y)\left[\mathrm{sh}\,\alpha z\cos\alpha(2H-z)-\mathrm{sh}\,\alpha(2H-z)\cos\alpha z\right]}{2aA_zM}\\ &+\frac{(T_x+T_y)\left[\mathrm{ch}\,\alpha(2H-z)\sin\alpha z-\mathrm{ch}\,\alpha z\sin\alpha(2H-z)\right]}{2aA_zM}\\ &-\frac{g}{a^2A_z}\frac{N_3-N_2}{M}\int_\zeta^H\left[\mathrm{ch}\,\alpha(H-z)\cos\alpha(H-z)\frac{\partial\rho}{\partial x}-\mathrm{sh}\,\alpha(H-z)\sin a(H-z)\frac{\partial\rho}{\partial y}\right]dz\\ &-\frac{g}{2a^2A_z}\int_\zeta^z\left[\mathrm{ch}\,\alpha(z-z')\cos\alpha(z-z')\frac{\partial\rho}{\partial y}+\mathrm{sh}\,\alpha(z-z')\sin\alpha(z-z')\frac{\partial\rho}{\partial x}\right]dz' \end{aligned}\right\} \quad (3)$$

* Received August 31, 1981
Presented at the First JECSS Workshop, June 1981 (cf. La mer **20**: 37-40, 1982).
** Second Institute of Oceanography, National Bureau of Oceanography, Hangzhou, Zhejiang, China

$$+\frac{g}{a^2A_z}\left(\frac{N_1+N_4}{M}\right)\int_\zeta^H\left[\mathrm{ch}\,\alpha(H-z)\cos\alpha(H-z)\frac{\partial\rho}{\partial y}+\mathrm{sh}\,\alpha(H-z)\sin\alpha(H-z)\frac{\partial\rho}{\partial x}\right]dz$$
$$+\frac{N_2-N_3}{a^2A_zM}\left(\frac{\partial p_a}{\partial x}+\rho_0g\frac{\partial\zeta}{\partial x}-g\int_0^H\frac{\partial\rho}{\partial x}dz\right)+\frac{N_1+N_4}{a^2A_zM}\left(\frac{\partial p_a}{\partial y}+\rho_0g\frac{\partial\zeta}{\partial y}-g\int_0^H\frac{\partial\rho}{\partial y}dz\right)$$
$$-\frac{1}{2a^2A_z}\left(\frac{\partial p_a}{\partial y}-\rho_0g\frac{\partial\zeta}{\partial y}-g\int_0^z\frac{\partial\rho}{\partial y}dz'\right),$$

$$v=\frac{(T_x-T_y)\left[\mathrm{sh}\,\alpha(2H-z)\cos\alpha z-\mathrm{sh}\,\alpha z\cos\alpha(2H-z)\right]}{2aA_zM}$$
$$+\frac{(T_x+T_y)\left[\mathrm{ch}\,\alpha(2H-z)\sin\alpha z-\mathrm{ch}\,\alpha z\sin\alpha(2H-z)\right]}{2aA_zM}$$
$$-\frac{g}{a^2A_z}\frac{N_3-N_2}{M}\int_\zeta^H\left[\mathrm{ch}\,\alpha(H-z)\cos\alpha(H-z)\frac{\partial\rho}{\partial y}+\mathrm{sh}\,\alpha(H-z)\sin\alpha(H-z)\frac{\partial\rho}{\partial x}\right]dz$$
$$-\frac{g}{a^2A_z}\frac{N_1+N_4}{M}\int_\zeta^H\left[\mathrm{ch}\,\alpha(H-z)\cos\alpha(H-z)\frac{\partial\rho}{\partial x}-\mathrm{sh}\,\alpha(H-z)\sin\alpha(H-z)\frac{\partial\rho}{\partial y}\right]dz \qquad (4)$$
$$+\frac{g}{2a^2A_z}\int_\zeta^z\left[\cos\alpha(z-z')\,\mathrm{ch}\,\alpha(z-z')\frac{\partial\rho}{\partial x}-\mathrm{sh}\,\alpha(z-z')\sin\alpha(z-z')\frac{\partial\rho}{\partial y}\right]dz'$$
$$+\frac{(N_2-N_3)}{a^2A_zM}\left(\frac{\partial p_a}{\partial y}+\rho_0g\frac{\partial\zeta}{\partial y}-g\int_0^H\frac{\partial\rho}{\partial g}dz\right)-\frac{(N_1+N_4)}{M_a{}^2A_z}\left(\frac{\partial p_a}{\partial x}+\rho_0g\frac{\partial\zeta}{\partial x}-g\int_0^H\frac{\partial\rho}{\partial x}dz\right)$$
$$+\frac{1}{2a^2A_z}\left(\frac{\partial p_a}{\partial x}+\rho_0g\frac{\partial\zeta}{\partial x}-g\int_0^z\frac{\partial\rho}{\partial x}dz'\right),$$

$$a=\sqrt{\frac{f\rho}{2A_z}},$$
$$M=\frac{1}{r}=\cos 2\alpha H+\mathrm{ch}\,2\alpha H,$$
$$N_1=\cos\alpha H\,\mathrm{ch}\,\alpha H\cos\alpha z\,\mathrm{ch}\,\alpha z, \qquad (5)$$
$$N_2=\cos\alpha H\,\mathrm{ch}\,\alpha H\sin\alpha z\,\mathrm{sh}\,\alpha z,$$
$$N_3=\sin\alpha H\,\mathrm{sh}\,\alpha H\cos\alpha z\,\mathrm{ch}\,\alpha z,$$
$$N_4=\sin\alpha H\,\mathrm{sh}\,\alpha H\sin\alpha z\,\mathrm{sh}\,\alpha z.$$

In Eqns. (3) and (4), ζ is unknown and must be determined. By the preceding equations and vertically integrated form of continuity equation, we may obtain ζ equation:

$$\frac{\partial}{\partial x}\left(\beta\frac{\partial\zeta}{\partial x}\right)+\frac{\partial}{\partial y}\left(\beta\frac{\partial\zeta}{\partial y}\right)+\frac{\partial}{\partial x}\left(\alpha\frac{\partial\zeta}{\partial y}\right)-\frac{\partial}{\partial y}\left(\alpha\frac{\partial\zeta}{\partial x}\right)$$
$$=-\frac{1}{\rho_0g}\left[\frac{\partial}{\partial x}\left(\beta\frac{\partial p_a}{\partial x}\right)+\frac{\partial}{\partial y}\left(\beta\frac{\partial p_a}{\partial y}\right)+\frac{\partial}{\partial x}\left(\alpha\frac{\partial p_a}{\partial y}\right)-\frac{\partial}{\partial y}\left(\alpha\frac{\partial p_a}{\partial x}\right)\right. \qquad (6)$$
$$\left.+\mathrm{rot}_z\,m\vec{T}+\mathrm{div}(\mathrm{n}\vec{T})-\left(\frac{\partial D_1}{\partial x}+\frac{\partial D_2}{\partial y}\right)\right],$$

$$m=\frac{1}{2a^2A_z}(1-2r\,\mathrm{ch}\,\alpha H\cos\alpha H),$$
$$n=\frac{1}{a^2A_z}r\sin\alpha H\,\mathrm{sh}\,\alpha H, \qquad (7)$$
$$r=\frac{1}{M},$$

$$\alpha=\frac{\rho_0 g}{A_z}\left[\frac{(\mathrm{sh}\,2aH+\sin 2aH)r}{4a^3}-\frac{H}{2a^2}\right],$$

$$\beta=\frac{\rho_0 g}{4a^3 A_z}r(\sin 2aH-\mathrm{sh}\,2aH),$$

$$\vec{T}=(T_x,\ T_y),$$

$$\mathrm{rot}_z\, m\vec{T}=\frac{\partial(mT_y)}{\partial x}-\frac{\partial(mT_x)}{\partial y},\qquad (8)$$

$$\mathrm{div}(\mathrm{n}\vec{T})=\frac{\partial(nT_x)}{\partial x}+\frac{\partial(nT_y)}{\partial y},$$

$$\frac{\partial D_1}{\partial x}+\frac{\partial D_2}{\partial y}=\left(\frac{\partial F_1}{\partial x}+\frac{\partial F_2}{\partial y}\right)+\left(\frac{\partial F_3}{\partial x}+\frac{\partial F_4}{\partial y}\right)+\left(\frac{\partial F_5}{\partial x}+\frac{\partial F_6}{\partial y}\right),\qquad (9)$$

$$\begin{aligned}\frac{\partial F_1}{\partial x}+\frac{\partial F_2}{\partial x}=&-\frac{\beta}{\rho_0}\int_0^H\left(\frac{\partial^2\rho}{\partial x^2}+\frac{\partial^2\rho}{\partial y^2}\right)dz-\frac{gr^2}{2a^2A_z}\\&\cdot\left[(\mathrm{sh}^2 2aH-\sin^2 2aH)\frac{\partial H}{\partial y}-2\mathrm{sh}2aH\sin 2aH\frac{\partial H}{\partial x}\right]\int_0^H\frac{\partial\rho}{\partial x}dz\\&+\frac{gr^2}{2a^2A_z}\left[(\mathrm{sh}^2 2aH-\sin^2 2aH)\frac{\partial H}{\partial x}+2\mathrm{sh}2aH\sin 2aH\frac{\partial H}{\partial y}\right]\\&\cdot\int_0^H\frac{\partial\rho}{\partial y}dz-\left[\frac{1}{\rho_0}\left(\beta\frac{\partial H}{\partial x}-\alpha\frac{\partial H}{\partial y}\right)-\frac{gH}{2a^2H_z}\frac{\partial H}{\partial y}\right]\frac{\partial\rho}{\partial x}\bigg|_{z=H}\\&-\left[\frac{gH}{2a^2A_z}\frac{\partial H}{\partial x}+\frac{1}{\rho_0}\left(\beta\frac{\partial H}{\partial y}+\alpha\frac{\partial H}{\partial x}\right)\right]\frac{\partial\rho}{\partial y}\bigg|_{z=H},\end{aligned}\qquad (10)$$

$$\begin{aligned}\frac{\partial F_3}{\partial x}+\frac{\partial F_4}{\partial y}=&-\frac{g}{2a^2A_z}\int_0^H dz\int_0^z\mathrm{sh}\,\alpha(z-z')\sin\alpha(z-z')\left(\frac{\partial^2\rho}{\partial x^2}+\frac{\partial^2\rho}{\partial y^2}\right)dz'\\&-\frac{g}{2a^2A_z}\int_0^H\left\{\mathrm{ch}\,\alpha(H-z)\cos\alpha(H-z)\left[\left(\frac{\partial H}{\partial x}\right)\left(\frac{\partial\rho}{\partial y}\right)-\left(\frac{\partial H}{\partial y}\right)\left(\frac{\partial\rho}{\partial x}\right)\right]\right.\\&\left.+\mathrm{sh}\,\alpha(H-z)\sin\alpha(H-z)\left[\frac{\partial H}{\partial x}\frac{\partial\rho}{\partial x}+\frac{\partial H}{\partial y}\frac{\partial\rho}{\partial y}\right]\right\}dz,\end{aligned}\qquad (11)$$

$$\begin{aligned}\frac{\partial F_5}{\partial x}+\frac{\partial F_6}{\partial y}=&-\frac{gr^2}{a^2A_z}\int_0^H\left[\frac{\partial H}{\partial x}\mathrm{ch}\,\alpha(H-z)\cos\alpha(H-z)+\frac{\partial H}{\partial y}\mathrm{sh}\,\alpha(H-z)\sin\alpha(H-z)\right]\\&\cdot\left[\mathrm{sh}\,2aH\sin 2aH\frac{\partial\rho}{\partial x}-(1+\mathrm{ch}\,2aH\cos 2aH)\frac{\partial\rho}{\partial y}\right]dz\\&+\frac{gr^2}{a^2A_z}\int_0^H\left[\frac{\partial H}{\partial x}\mathrm{sh}\,\alpha(H-z)\sin\alpha(H-z)-\frac{\partial H}{\partial y}\mathrm{ch}\,\alpha(H-z)\cos\alpha(H-z)\right]\\&\cdot\left[\mathrm{sh}\,2aH\sin 2aH\frac{\partial\rho}{\partial y}+(1+\mathrm{ch}\,2aH\cos 2aH)\frac{\partial\rho}{\partial x}\right]dz\\&-\frac{gr}{4a^3A_z}\int_0^H\left(\frac{\partial^2\rho}{\partial x^2}+\frac{\partial^2\rho}{\partial y^2}\right)\left[(\mathrm{sh}2aH-\sin 2aH)\,\mathrm{ch}\,\alpha(H-z)\cos\alpha(H-z)\right.\\&\left.-(\mathrm{sh}\,2aH+\sin 2aH)\,\mathrm{sh}\,\alpha(H-z)\sin\alpha(H-z)\right]dz+\frac{gr}{2a^2A_z}\int_0^H\left\{\left[\mathrm{ch}\,\alpha(H-z)\right.\right.\\&\left.\left.\cdot\sin\alpha(H-z)\,\mathrm{sh}\,2aH+\mathrm{sh}\,\alpha(H-z)\cos\alpha(H-z)\sin 2aH\right]\left[\frac{\partial H}{\partial x}\frac{\partial\rho}{\partial x}+\frac{\partial H}{\partial y}\frac{\partial\rho}{\partial y}\right]\right.\end{aligned}\qquad (12)$$

$$+\left[\operatorname{sh}\alpha(H-z)\cos\alpha(H-z)\operatorname{sh}2aH-\operatorname{ch}\alpha(H-z)\sin\alpha(H-z)\sin 2\alpha H\right]\left[\frac{\partial H}{\partial x}\frac{\partial\rho}{\partial y}-\frac{\partial H}{\partial y}\frac{\partial\rho}{\partial x}\right]\Big\}dz-\frac{gr}{4a^3A_z}\Big[(\operatorname{sh}2aH-\sin 2aH)\left(\frac{\partial\rho}{\partial x}\Big|_{z=H}\frac{\partial H}{\partial x}+\frac{\partial\rho}{\partial y}\Big|_{z=H}\frac{\partial H}{\partial y}\right)$$
$$-(\operatorname{sh}2aH+\sin 2aH)\left(\frac{\partial\rho}{\partial y}\Big|_{z=H}\frac{\partial H}{\partial x}-\frac{\partial\rho}{\partial x}\Big|_{z=H}\frac{\partial H}{\partial y}\right)\Big].$$

The vertical velocity component W is given by

$$W=-\int_H^z\left(\frac{\partial u}{\partial x}+\frac{\partial v}{\partial y}\right)dz'. \tag{13}$$

3. Finite Element Formulation

Eqn. (6) is equivalent to the following functional relations (Fig. 1):

$$B(\zeta,\eta)=\iint_\Omega\Big\{\frac{1}{\rho_0 g}\Big[\frac{\partial}{\partial x}\left(\beta\frac{\partial p_a}{\partial x}\right)+\frac{\partial}{\partial y}\left(\beta\frac{\partial p_a}{\partial y}\right)+\frac{\partial}{\partial x}\left(\alpha\frac{\partial p_a}{\partial y}\right)-\frac{\partial}{\partial y}\left(\alpha\frac{\partial p_a}{\partial x}\right)\Big]-\operatorname{rot}_z m\vec{T}$$
$$-\operatorname{div}(n\vec{T})+\left(\frac{\partial D_1}{\partial x}+\frac{\partial D_2}{\partial y}\right)\Big\}\eta d\Omega+\int_\Gamma\psi\eta dl, \tag{14}$$

in which

$$B(\zeta,\eta)=\iint_\Omega\beta\left(\frac{\partial\zeta}{\partial x}\frac{\partial\eta}{\partial x}+\frac{\partial\zeta}{\partial y}\frac{\partial\eta}{\partial y}\right)d\Omega$$
$$+\iint_\Omega\alpha\left(\frac{\partial\zeta}{\partial y}\frac{\partial\eta}{\partial x}-\frac{\partial\zeta}{\partial x}\frac{\partial\eta}{\partial y}\right)d\Omega. \tag{15}$$

On the boundary Γ:

$$\psi=\beta\frac{\partial\zeta}{\partial n}+\alpha\frac{\partial\zeta}{\partial s}=\text{specific values}. \tag{16}$$

Note that $\eta(x,y)\in C^{(0)}$, $C^{(0)}$ being continuous function classes. The above functional relations are the starting point for the finite element models. Set

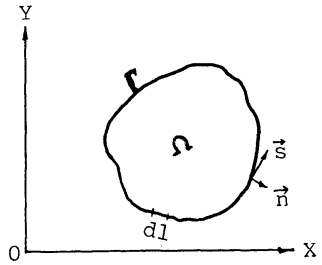

Fig. 1. The region and the boundary.

$$\frac{\partial\zeta}{\partial x}=F,\quad\frac{\partial\zeta}{\partial y}=G. \tag{17}$$

For three-node triangular finite elements, the interpolation functions are the linear functions. $F^{(l)}$, $G^{(l)}$, $\eta^{(l)}$ can be expressed as follows:

$$\left.\begin{aligned}F^{(l)}&=\sum_{i=1}^{M}F_i{}^{(l)}\varphi_i{}^{(l)},\\ G^{(l)}&=\sum_{i=1}^{M}G_i{}^{(l)}\varphi_i{}^{(l)},\\ \eta^{(l)}&=\sum_{i=1}^{M}\eta_i{}^{(l)}\varphi_i{}^{(l)},\end{aligned}\right\} \tag{18}$$

where $\varphi_i{}^{(l)}$ are the linear interpolation functions. Substituting these values into (14), (15) and the following relationship,

$$\iint_\Omega\left(\frac{\partial F}{\partial y}-\frac{\partial G}{\partial x}\right)\eta d\Omega=0, \tag{19}$$

we can obtain $F^{(l)}$, $G^{(l)}$ finite element equations and can then assemble element equations. The global system of F, Q equations (matrix form) are

$$\begin{bmatrix}[A], & [M]\\ [Q_2], & -[Q_1]\end{bmatrix}\begin{bmatrix}[F]\\ [G]\end{bmatrix}=\begin{bmatrix}[\Psi]+[\Psi]\\ [O]\end{bmatrix}, \tag{20}$$

for the expressions of elements of submatrices $[A]$, $[M]$, $[Q_1]$, $[Q_2]$, $[\Psi]$ and $[\Psi]$. The system of equations (20), though not write down here, may be solved numerically.

4. Discussion of Computational Results

We will now proceed the application of our method to the calculation of three-dimensional Kuroshio Current in the eastern area of Taiwan. The area considered ranges from 21°46′N to 25°N in the north-south direction and from 121°E to 125°E in the west-east direction. Hydrographical data refer to CSK and JMA data in July 1966. For simplicity, we may assume that the

current is steady and the wind field is steady and the wind speed is treated as average wind speed which is $V_w=5$ m/sec, the southerly wind field. Thus, the current obtained by our calculation can be used to define an average condition. The coefficient of vertical dynamic eddy viscosity $A_z=1$, 10, 100, 300 g/cm/sec in our calculation. If we consider the friction depth to be about 50~60 meters, A_z should be taken to be 100 g/cm/sec.

The horizontal velocity distributions for each water depth H ($H=0$, 50, 100, 200, 300 m, . .) tend to agree with the realistic flow patterns. The main current is located on the western part of the area, flowing northeastward. The countercurrent exists in the eastern part of the area. It is weaker than the main current. An anticyclonic gyre is formed in the region which ranges from 22°20′N to 24°N in the north-south direction and from 123°10′E to 124°30′E in the west-east direction. The results show that the current due to the density gradient is major (about 90%). Of secondary importance (about 10%) are the current due to wind driving, the current due to the interaction effect of turbulent friction and density gradient and the current due to pressure gradient at bottom. The computational results show also that for the Kuroshio Current the difference between the horizontal velocities computed by four different A_z values is of the order of 10% that is also the case with the horizontal velocities obtained by different wind fields and that the effect of wind stress exerts their influence only in the friction depth.

Our calculation suggests that the finite element method for solving problems with irregular geometries, unequal grids and mixed boundary conditions is better than the finite difference method. Its accuracy is sufficient and its efficiency is acceptable.

References

GALLAGHER, R. H., J. T. ODEN and C. TAYLOR (1975): Finite Elements in Fluids. **1**, 95-131; **2**, 31-54.

ODEN, J. T., O. C. ZIENKIEWICZ and R. H. GALLAGHER (1974): Finite Element Methods in Flow Problems. Univ. of Alabama, Huntsvills Press. 51-100, 103-120.

PLATZMAN, G. W. (1978): Normal modes of the world ocean. Part 1. Design of a finite-element barotropic model. J. Phys. Oceanogr., **8**, 323-343.

YUAN, Y., W. XU and K. HE (1980): Application of the finite element method of the calculation of the Kuroshio Current in the eastern area of Taiwan. Acta Oceanol. Sinica, **2**, 7-19.

Appendix

Symbols are defined as follows;

u, v and w: the components of velocity in the x, y and z directions, respectively.
p: the pressure.
ρ: the density.
g: the gravitational acceleration.
f: the Coriolis parameter.
ζ: the free surface elevation.
H: the water depth ($H<0$).
A_z: the vertical eddy viscosity coefficient.
T_x and T_y: the components of the wind stress vector in the x and y directions, respectively.
P_a: the atmospheric pressure.

有限要素法による三次元海流の計算

Yaochu YUAN and Kulrong HE

要旨: この方法は，前報「台湾東方海域の黒潮への有限要素法の応用」のつづきである。圧力勾配，コリオリの力，鉛直渦動拡散からなる運動方程式の解をまず求め，つぎに，海面のでこぼこを有限要素法を使って求める。この方法を使って台湾東方海域の黒潮を計算した。

La mer 20: 141-150, 1982
Société franco-japonaise d'océanographie, Tokyo

浮遊性やむし *Sagitta nagae* ALVARIÑO の繊毛感覚器官の微細構造*

永沢祥子**, 丸茂隆三**

Ultrastructure of Ciliary Sense Organs of a Pelagic Chaetognath *Sagitta nagae* ALVARIÑO*

Sachiko NAGASAWA** and Ryuzo MARUMO**

Abstract: Chaetognaths have a large number of ciliary sense organs on the body. The function of these organs has been discussed on the analogy of morphological and behavioral aspects for lack of direct evidence by electrophysiological methods.

This paper deals with the ultrastructure of these organs and the base of a lateral fin in *Sagitta nagae*. On the basis of TEM micrographs of *S. nagae* schematic drawings of a sensory cell, a ciliary sense organ and the base of a lateral fin are shown. A sensory cell is composed of a large nucleus, a mitochondrion and more than two processes showing the structure of a cilium. Ciliary sense organs are oriented longitudinally (L) and transversely (T) to the body axis. L organs are smaller than T organs and the numbers of their cilia are 50 to 100 and 200 to 300, respectively. A sensory cell has more than two cilia. Therefore, L organs consist of less than 25 to 50 sensory cells while T organs less than 100 to 150. It was not determined whether the sensory cell of *S. nagae* is of primary type or of secondary one. Many axons are found at the base of a lateral fin of *S. nagae*. These axons are related to the existence of many ciliary sense organs on two pairs of lateral fins. Such a distribution of these organs is peculiar to *S. nagae* because other epipelagic species have just one ciliary sense organ only on the posterior lateral fin.

1. 緒

やむしの体表に分布する多数の繊毛からなる感覚器官は，はじめ触覚に関係していると考えられ，触毛斑 (tangoreceptor) と名づけられた。その後，この器官は機械的な刺激を感じる機械受容器であると考えられるようになった。この器官は fan-shaped tufts, sensory tufts (BIERI, 1966), ciliary tufts, ciliary sense organs, stiff cilia (HORRIDGE and BOULTON, 1967), hairs, sensory spots, fine hair fans (FEIGENBAUM, 1978), ciliary fences (BONE and PULSFORD, 1978) sensory hair fans (SPERO *et al.*, 1979) など，これまでさまざまに呼ばれてきた。ここでは永沢・丸茂 (1978) にしたがって，この器官を繊毛感覚器官 (ciliary sense organs，以後 cso と略記する) と呼ぶことにする。cso は古くから若干の種類についてその分布図が作成されていたが，近年数種のやむしについて新たにより詳細な分布が図示された (永沢・丸茂，1978; FEIGENBAUM, 1978; 永沢，1978)。なかでも底生性やむし *Spadella cephaloptera* の cso については多くの研究者 (HERTWIG, 1880; JOHN, 1933; HORRIDGE and BOULTON, 1967; BONE and PULSFORD, 1978; FEIGENBAUM, 1978) による分布図の作成のみでなく，透過電子顕微鏡 (TEM) により内部構造 (HORRIDGE and BOULTON, 1967; REISINGER, 1970; BONE and PULS-

* 1982年2月12日受理 Received February 12, 1982
** 東京大学海洋研究所 〒164東京都中野区南台1-15-1
Ocean Research Institute, University of Tokyo, Minamidai 1-15-1, Nakano-ku, Tokyo, 164 Japan

FORD, 1978) が，また走査電子顕微鏡 (SEM) により外部構造 (BONE and PULSFORD, 1978) が明らかにされている。SEM の使用により BONE and PULSFORD (1978) は *S. cephaloptera* の体に，従来報告されていなかった形態の2種類の感覚器官を新たに見出し，cso とともにこれら2種の器官について TEM による内部構造の観察も行なった。このように，底生性やむしの cso については TEM および SEM の活用による研究が進んでいる。ただし，これらの研究結果には矛盾する点もあり，これらについては今後さらに検討を加える必要がある。これに対し，浮遊性やむしについては *Sagitta nagae* の cso の外部構造が SEM の使用により明らかにされたが，その内部構造については光学顕微鏡 (LM) による観察があるのみである（永沢・丸茂，1978)。したがって，*S. nagae* の cso の内部構造について詳細に解明し，*S. cephaloptera* の cso と比較するためには TEM による組織学的な研究が必要である。

本研究では，すでに明らかになった cso の外部構造と，これから明らかにしようとしている内部構造の両面から，cso の機能と生態的役割を検討する。

TEM 用試料作成および電子顕微鏡 JEM-7 の使用に際して，東京大学海洋研究所資源生物部門の原政子技官にお世話になった。透過電子顕微鏡写真の解釈について種々ご教示いただいた東京医科歯科大学和気健二郎教授および東京大学農学部

Procedure	Reagent	Duration	Temperature
anesthetization	0.1% w/v MS222	1 min.	room temperature
fixation	3 % glutaraldehyde	30 min.	0 - 4°C
	3 % glutaraldehyde	4 - 6 hrs.	
washing	0.1 M phosphate buffer	10 - 30 min.	0 - 4°C
	0.1 M phosphate buffer	until the next step	
fixation	1 % osmium tetroxide	1 hr.	0 - 4°C
washing	distilled water	1 min.	0 - 4°C
staining	2 % uranyl acetate	1 hr.	0 - 4°C
dehydration	50, 90 % ethyl alcohol	5 min., 5 min., 5 min.	
	95, 99, 100 % ethyl alcohol	15 min., 15 min., 15 min.	0 - 4°C
replacement	propylene oxide	3 min., 3 min., 3 min.	room temperature
	propylene oxide and Epon	overnight	room temperature
	Epon	8 hrs.	room temperature
embedding	Epon	36 hrs.	60°C
sectioning	(Sorvall MT2 "Porter Blum" ultramicrotome with a glass knife)		room temperature
staining	saturated solution of uranyl acetate	15 min.	room temperature
washing	distilled water	3 min.	room temperature
staining	0.4 % lead citrate	2 min.	room temperature
washing	distilled water	3 min.	room temperature
examination with TEM	(JEM-7)		

Fig. 1. Procedures to prepare biological specimens for TEM.

羽生功教授に感謝の意を表する。

2. 材料と方法

1978年1月18～21日に東京大学海洋研究所の淡青丸で相模湾において，夜間に表層曳ネットでプランクトンを採集した。やむしの感覚器官は損傷しやすいので，ネットのバケットには 2*l* のポリエステル製ビーカーを使用した。プランクトンからやむしを選別し，種を同定した。*S. nagae* 数個体をグルタールアルデヒド，ついでオスミウム酸で固定し，透過電子顕微鏡（TEM）用の試料とした。TEM 用試料の作成方法を Fig. 1 に示す。固定から脱水までの過程は SEM 用試料の作成方法（永沢・丸茂，1978）とほぼ同じであるが，グルタールアルデヒドの濃度を濃くし，オスミウム酸による後固定の時間を長くした。TEM 用試料の切片の一部はトルイジンブルーで染色し，LM による観察のために用いた。

3. 結　果

繊毛感覚器官（cso）の内部構造

1) LM による内部構造の観察：cso は表皮の上に丘のようにもりあがり，中心部に多数の繊毛が生えている。トルイジンブルーで染色した切片には，cso，鰭（f）とそのつけ根のふくらみが見える（Fig. 2A）。cso を拡大すると感覚細胞の列があり，その上方には繊毛の断面が見える（Fig. 2B）。鰭のつけ根のふくらみの部分を拡大すると（Fig.

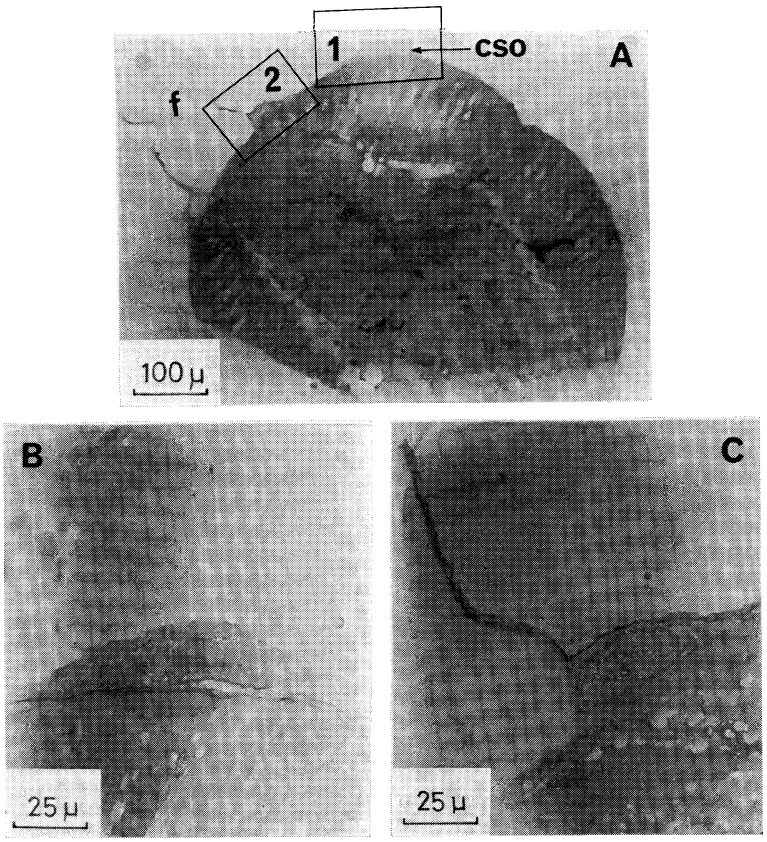

Fig. 2. (A) A micrograph of a transverse section through a ciliary sense organ (cso) and a fin (f), cut with a glass knife and stained with toluidine blue. (B) Enlarged view of a ciliary sense organ numbered "1" in (A). (C) Enlarged view of the base of a fin numbered "2" in (A).

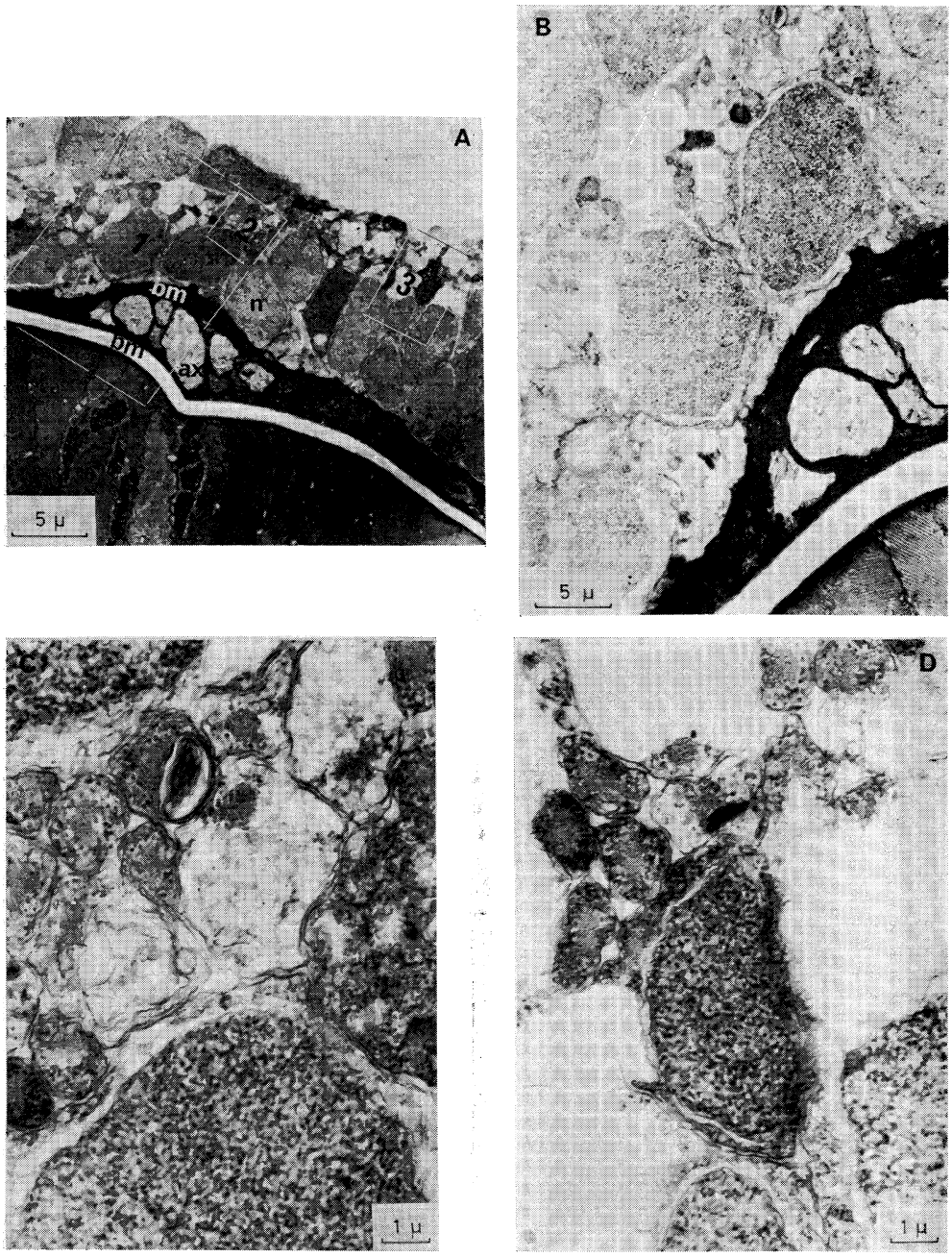

Fig. 3. TEM micrographs showing a part of ciliary sense organ in *Sagitta nagae*. (A) There are large numbers of nuclei (n) of sensory cells above a basement membrane (bm) while axons (ax) are between basement membranes. (B) Enlarged view of a part numbered "1" in (A). (C) Enlarged view of a part numbered "2" in (A). (D) Enlarged view of a part numbered "3" in (A). Cross sections of the base of cilia are found near the nucleus in (C) and (D).

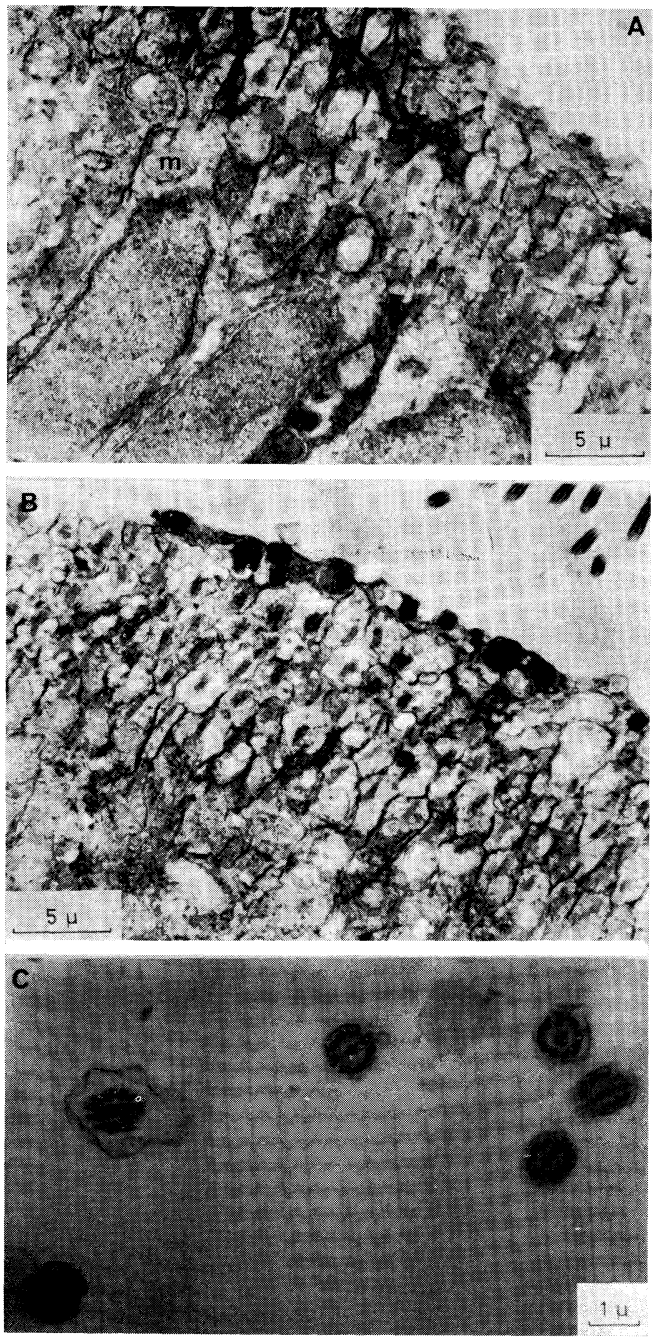

Fig. 4. TEM micrographs of upper parts of a ciliary sense organ in *Sagitta nagae*. (A) A mitochondrion (m) is found near the nucleus. (B) Longitudinal sections of cilia are shown. (C) Transverse sections of cilia are shown.

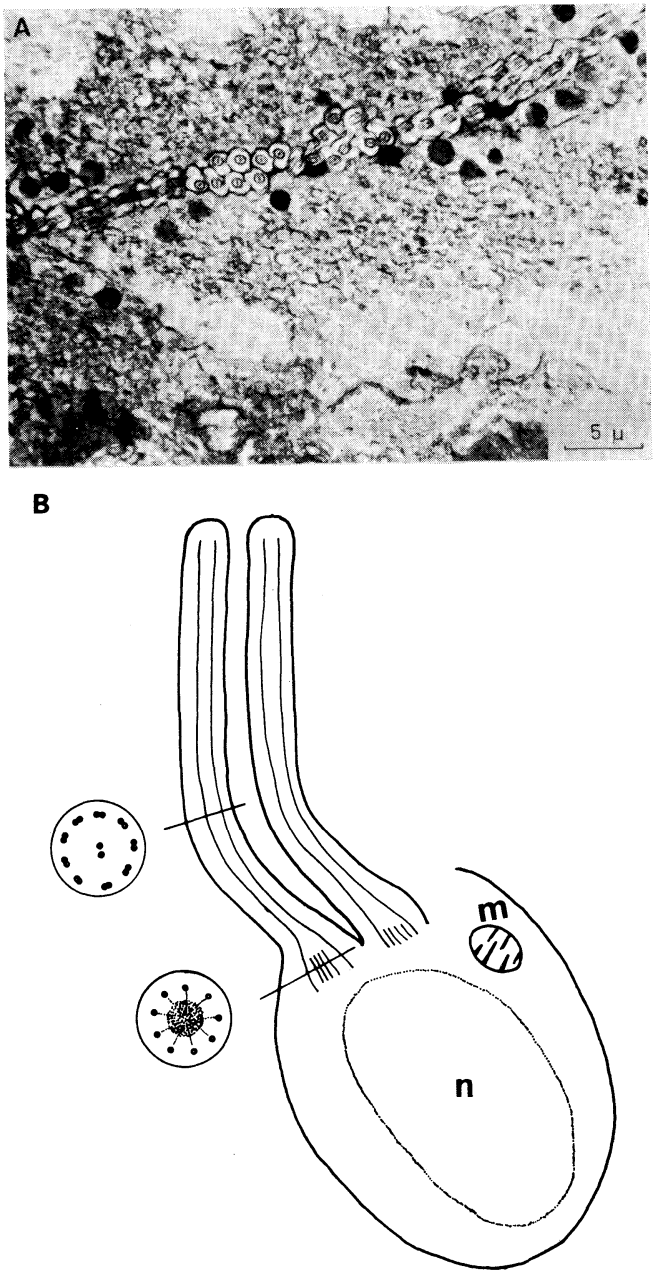

Fig. 5. (A) A TEM micrograph of a section parallel with the surface of the body with a group of cilia cut transversely. This ciliary sense organ is oriented longitudinally on the basis of a number of cilia. (B) A diagram of a sensory cell of *Sagitta nagae* based on TEM micrographs. A sensory cell is composed of a large nucleus (n), a mitochondrion (m) and more than two processes showing the structure of a cilium.

2C)，鰭の薄い膜と体の間にはなにかがつまっており空洞ではない。

2) TEM による内部構造の観察: cso の縦断面の一部を示した (Fig. 3A, B)。白と黒の帯状の部分は基底膜で，その間に神経繊維の束がある。黒い基底膜の外側に感覚細胞の大きな核が見える。核の周辺をさらに拡大すると (Fig. 3C, D)，繊毛のねもとの横断面がいくつか見える。その横断面には中心に細いフィラメントが密集し，周辺部にはいくつかの微小管がある。Fig. 3C, D からひとつの感覚細胞は1本ではなく，2本以上の繊毛からなることがわかった。感覚細胞の核の付近にはミトコンドリアがあり (Fig. 4A)，感覚細胞が外に向かって延びている部分には繊毛の断面が見え (Fig. 4A, B)，繊毛はさらに外の方まで延びて，横断面は2本の中心小管と9組の周辺小管とが並行に配列した微小管の束を主体とする構造，いわゆる9+2の構造を示している (Fig. 4C)。cso の繊毛の列の横断面を示した (Fig. 5A)。感覚細胞が2本以上の繊毛をもつため，繊毛は密集している。繊毛の近くに電子密度の濃い球状体が散在している。これは蛋白質の結晶であると考えられる。*S. cephaloptera* では cso の繊毛は *S. nagae* のようにちみつに配列していない。また，cso の周囲には典型的な上皮細胞があり，その細胞のいくつかは大きな球状の蛋白質の結晶を有している (HORRIDGE and BOULTON, 1967)。

以上の TEM 写真に基づいて，cso の感覚細胞

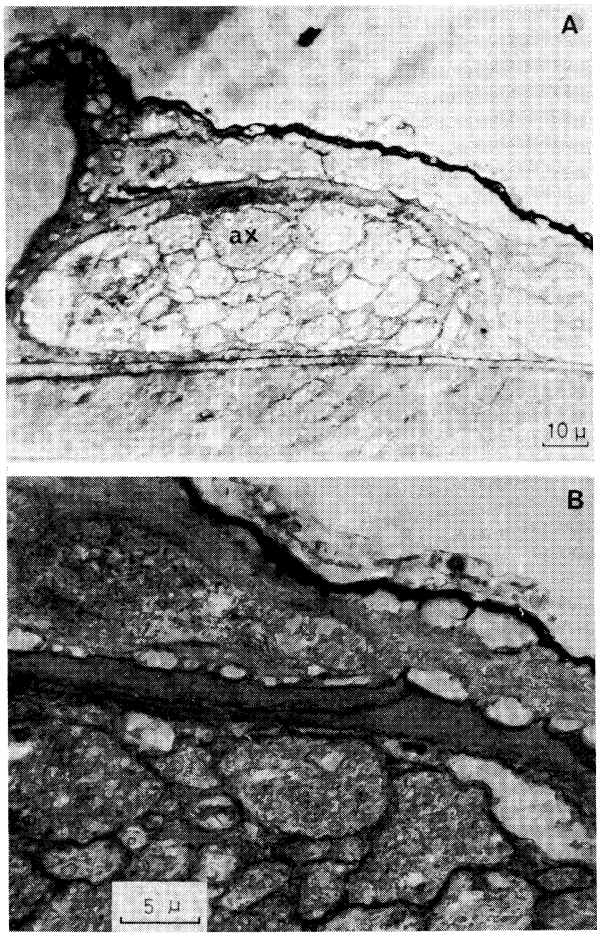

Fig. 6. TEM micrographs of the base of a fin in *Sagitta nagae*. (A) Large numbers of axons are found at the base of a fin. (B) Enlarged view of groups of axons.

の模式図を示した（Fig. 5B）。感覚細胞は大きな核，ミトコンドリア，長い2本以上の突起をもつ。この突起の基部は繊毛のいわゆる 9+2 の構造とは少し異なるが，基部以外の部分は 9+2 の構造をもつので，長い突起を繊毛と呼ぶことができる。感覚器官はある刺激を受容する器官であるので，感覚細胞を受容器細胞と呼ぶことがある。

cso は繊毛が体軸に平行（longitudinally）および垂直（transversely）に配列する2型があり，それぞれを L，T と呼ぶ。L は T より小規模で繊毛も少ないが，両者の外部構造は基本的には同じであった（永沢・丸茂，1978）。さらに L，T の繊毛数は SEM 写真から，それぞれ 50～100，200～300 であると推定された。また，感覚細胞は複数の繊毛をもつことが本研究により明らかになった。したがって，*S. nagae* の感覚細胞の数は繊毛数の半分以下，すなわち，L，T でそれぞれ 25～50以下，100～150 以下である。一方，底生性やむし *S. cephaloptera* では，cso の感覚細胞はその細胞から1本の樹状突起を伸ばし，その先端が繊毛で終る構造で（HORRIDGE and BOULTON, 1967），*S. nagae* とは異なる。*S. cephaloptera* の cos は，およそ 190 の繊毛をもつが，樹状突起の数は不明である。したがって cso を構成する感覚細胞の数は明らかでない。BONE and PULSFORD (1978) によれば，*S. cephaloptera* は浮遊性やむし *S. elegans* と同じく T，L 2種の cso をもっている。前者の T は L より多数存在し，T の規模は L より大きく，T は L のおよそ2倍の感覚細胞からなる。

鰭のつけ根のふくらんだ部分には多数の神経繊維（軸索）の束がある（Fig. 6A, B）。*S. nagae* は他のやむしと異なり，2対の側鰭の上には多数の cso をもち，鰭上と体表の cso は SEM 写真からは構造上の差違はなかった（永沢・丸茂，1978）。*S. nagae* の鰭のつけ根には，このように多数の神経がきており，そこから神経が側鰭上にある多数の cso に達していると考えられる（Fig. 7A）。Fig. 6A に基づいて，Fig. 7A を a 線で切断した面の模式図（Fig. 7B）を，また TEM による今回の組織学的な研究の結果に基づいて，*S. nagae* の cso の模式図（Fig. 7C）を示した。Fig. 7C では神経繊維の束が基底膜を2回つきぬけて神経繊維が感覚細胞に達しており，感覚細胞は以前に示した模式図（永沢・丸茂，1978）と同じく，一次感覚細胞として示されている。それは本研究ではシナップスや神経細胞の存在の確認ができなかったことによる。今後の研究において，シナップスや神経細胞の確認ができれば，この模式図を改訂しなければならない。基底膜と基底膜の間に神経が存在することは本研究で確かめた（Fig. 3A, B）が，第一，第二の基底膜を神経がつきぬける部分

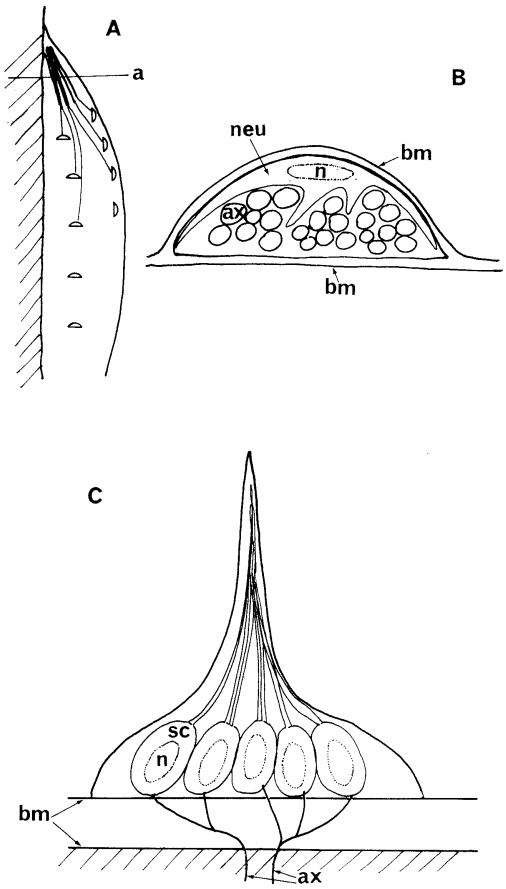

Fig. 7. Schematic drawings of the nerve fibers (axons) and ciliary sense organs on the lateral fin (A), of the base of a fin cut transversely (B) and of a ciliary sense organ (C) in *Sagitta nagae*.
bm, basement membrane; ax, axon; n, nucleus; neu, neurilemma; sc, sensory cell.

の観察はできなかった。このように，*S. nagae* の cso の構造に関する研究は十分とはいえず，感覚細胞が底生性の *S. cephaloptera* のように一次感覚細胞（HORRIDGE and BOULTON, 1967; BONE and PULSFORD, 1978）であるのか，二次感覚細胞であるのか明らかではない。しかし，いずれにせよ *S. nagae* の cso は多数の受容器細胞からなり，各受容器細胞は複数の繊毛を有することはまちがいない。

4. 論　議

cso の機能を解明する直接的な方法は電気生理学的な研究である。しかしこのような研究は試料が小型でかつ脆弱であるため，実験技術上きわめて困難であり，今のところ行なわれていない。したがって，cso の機能はやむしの行動や cso の形態に関する研究に基づいて論議される。cso の機能について著者らの考えを次に述べる。

T は体の前後，L は体の左右の方向からの振動や乱流によって生じる水の動きを感知する。水の振動が柔軟性を有する繊毛に与える変化，たとえば動く方向と屈曲，角度，変位の程度が T あるいは L の受容器細胞を刺激する。このような機械的な刺激は受容器細胞の細胞膜に電位変化を起す。このとき生じる受容器電位は神経細胞内に起動電位をひき起し，これが感覚器官から中枢神経へ神経インパルスを送る。中枢神経は変化が起ると同時にそれを知り，動物はただちに適切に反応する。このようにして，やむしは外界の水の動きの変化を cso で感じ，その変化はすみやかに中枢神経に伝わり，餌や捕食者の存在と位置を知り，摂餌や逃避の行動を起す。やむしは視覚に頼らずに全身にある多数の cso が受ける機械的な刺激により，外界の情報をとらえつつ変化に対して敏速に行動する。

cso は魚の側線器官の末梢にある管器（canal organs）や遊離感丘（epidermal neuromasts）と外部形態が似ている。管器や遊離感丘の構造に関する研究およびそれらの器官を構成する繊毛細胞の電気生理学的な研究は，いろいろな魚を用いて行なわれている（FLOCK, 1967, 1971）。しかし，やむしの cso の構造に関する研究は，底生性の *S. cephaloptera* および浮遊性の *S. nagae* について行なわれたのみである。前者の cso は組織学的研究の対象としてたびたびとりあげられてきた（HORRIDGE and BOULTON, 1967; REISINGER, 1970; BONE and PULSFORD, 1978）が，浮遊性やむしについては *S. nagae* の cso がはじめて研究された。比較的よく研究された *S. cephaloptera* についても，cso が一次感覚細胞からなるという説（HORRIDGE and BOULTON, 1967; BONE and PULSFORD, 1978）と二次感覚細胞からなるという説（REISINGER, 1970）がある。HORRIDGE and BOULTON (1967) が示した cso は REISINGER (1970) の感丘 (neuromasts) に相当するが，TEM 写真の解釈は両者で異なる。REISINGER (1970) は cso を感丘と呼び，その縦，横断面の TEM 写真を示し，さらに *Spadella* と魚 *Lota* の感丘の模式図を比較している。REISINGER (1970) の写真や図を見る限りでは，*Spadella* は魚の感丘ほど複雑ではないが，基本的には魚と同じ構造の器官をもっており，感覚細胞は二次感覚細胞であり，感丘と呼ぶのがふさわしく思われる。

やむしのように小型で脆弱なプランクトンが組織学的研究の対象になる例は多いとはいえない。しかし，解剖学的，組織学的研究を通して，やむしの系統的位置を解明しようとする研究は，試料の採集が容易であり，脆弱でない底生性やむしを用いて行なわれてきた。BONE and PULSFORD (1978) は，やむしの末梢の感覚器官についてその構造を SEM，TEM で調べ，それがどの分類群の感覚器官と相同であるかを明らかにしようとした。その結果，*S. cephaloptera* には cso のほかに繊毛をもつ2種類の感覚受容器があることが分った。その一つは *S. cephaloptera* の頭部腹面にのみ存在し，enclosed ciliary slit receptors と呼ばれ，化学受容器であると考えられた。もう一つは尾鰭，尾部，頭部に存在し，単一の太い繊毛であり，cso の第二の型であろうと推測された。BONE and PULSFORD (1978) は，末梢の感覚器官に関する研究から，やむしの系統的な位置づけを明確にすることはできなかった。また，彼らは

REISINGER (1970) を引用していないため，REISINGER (1970) の結果をどのように評価し，それを自分たちの結論とどのように関連づけるのか不明である。それはともかく，*S. cephaloptera* についても cso の組織学的研究をさらに追試する必要がある。

S. cephaloptera の体表，鰭上の感覚器官の LM による観察では，すべての器官は同一であり，TEM や SEM で観察された (HORRIDGE and BOULTON, 1967; BONE and PULSFORD, 1978) 剛毛は認められなかった (FEIGENBAUM, 1978)。それは，この剛毛が損傷しやすいこと，またその配列や総数は標本により異なり，ある標本では欠損している (BONE and PULSFORD, 1978) ことによる。LM ではどの器官も同じ構造をしていると観察され，ただ1種類の器官の存在を明らかにしただけであった。ところが形態の異なる3種類の器官の存在がSEMにより確認された (BONE and PULSOFRD, 1978)。その意義は大きい。

S. nagae のほかに表層性やむし数種の体表に分布する cso を SEM で観察したところ，いずれもその外部構造は同じであった (永沢，未発表)。しかし，*S. ferox* のある個体に従来の cso の構造とは異なる器官を見出した。これがまれに存在する形態なのか，*S. ferox* のどの個体にも存在するのかわからない。各種のやむしの多数の個体について，頭部から尾部まで，背面および腹面にわたって，体中に分布する器官をくまなく，ていねいに SEM で観察することが必要である。また，TEM による観察もあわせて行なうことにより，それらの器官の機能や生態的役割はより適切に解釈されると思われる。

文　献

BIERI, R. (1966): The function of the "wings" of *Pterosagitta draco* and the so-called tangoreceptors in other species of Chaetognatha. Publ. Seto mar. biol. Lab., **14**, 23-26.

BONE, Q. and A. PULSFORD (1978): The arrangement of ciliated sensory cells in *Spadella* (Chaetognatha). J. mar. biol. Ass. U.K., **58**, 565-570.

FEIGENBAUM, D. L. (1978): Hair-fan patterns in the Chaetognatha. Can. J. Zool., **56**, 536-546.

FLOCK, Å. (1967): Ultrastructure and function in the lateral line organs. p. 163-197, *In* Lateral Line Detectors (ed. P. CAHN). Indiana Univ. Press, Bloomington, Indiana.

FLOCK, Å. (1971): The lateral line organ mechanoreceptors. p. 241-263, *In* Fish Physiology V. Sensory Systems and Electric Organs (eds. W.S. HOAR and D.J. RANDALL). Academic Press, New York and London.

HERTWIG, O. (1880): Über die Entwicklungsgeschichte der Sagitten. Jena Ges. Med. Naturw., **14**, 196-303.

HORRIDGE, G.A. and P.S. BOULTON (1967): Prey detection by Chaetognatha via a vibration sense. Proc. R. Soc. London, B., **168**, 413-419.

JOHN, C.C. (1933): Habits, structure and development of *Spadella cephaloptera*. Q.J. Microsc. Sci., **75**, 625-696.

永沢祥子 (1978): 沿岸浮遊性毛顎類の生態学的研究，とくに *Sagitta nagae* ALVARIÑO について．学位論文，東京大学，392 pp.

永沢祥子，丸茂隆三 (1978): 走査電子顕微鏡によるやむし *Sagitta nagae* ALVARIÑO の繊毛感覚器官の構造．うみ，**16**, 7-17.

REISINGER, E. (1970): Zur Problematik der Evolution der Coelomaten. Zeit. zool. Sys. Evo., **8**, 81-109.

SPERO, H.J., D. HAGAN and A. VASTANO (1979): An SEM examination of *Sagitta tenuis* CONANT (Chaetognatha) utilizing a special sedation and handling procedure. Trans. Amer. Micros. Soc., **98**, 139-141.

La mer 20: 151-160, 1982
Société franco-japonaise d'océanographie, Tokyo

Early Diagenesis of Manganese and Phosphorus in Nearshore Sediments Collected from Suruga Bay, Japan*

Akio NISHIDA**, Yoshihisa KATO*** and Shiro OKABE***

Abstract: Manganese and phosphate in the interstitial waters of reducing marine sediment cores collected from Suruga Bay were analyzed. Manganese and phosphate concentration peaks existed in their vertical distributions, and below the peaks, these concentrations sharply decreased with depth.

From the application of the diagenetic mass transport equation to the distributions of the two elements, it could be estimated that authigenic mineral precipitation rate constants for the two elements were 3.1 yr^{-1} and 2.3 yr^{-1}, respectively. Dissolved manganese produced by the reduction of manganese oxides may be removed from the interstitial waters by the formation of authigenic minerals in a very short time compared with the results of deep sea sediments. Dissolved phosphate liberated during the decomposition of organic phosphorus may be also removed within several months. The upward fluxes of manganese and phosphate across the sediment-water interface were 8.3 $\mu M\ cm^{-2}\ yr^{-1}$ and 0.28 $\mu M\ cm^{-2}\ yr^{-1}$, respectively.

1. Introduction

It is well known that interstitial waters are very sensitive tracers for diagenetic reactions in marine sediments, and they have been actively studied in recent years (BERNER, 1964, 1971, 1974, 1980; NISSENBAUM *et al.*, 1972; PRESLEY *et al.*, 1972; SHOLKOVITZ, 1973; VANDERBOUGHT *et al.*, 1977a, b; MURRAY *et al.*, 1978; EMERSON *et al.*, 1980; KLINKHAMMER, 1980; ODA, 1980). Manganese and phosphate are common elements for the geochemical study of interstitial water (PRESLEY *et al.*, 1967; CALVERT and PRICE, 1972; DUCHART *et al.*, 1973; HOLDREN *et al.*, 1975; BERNER, 1977; MARTENS *et al.*, 1978; TSUNOGAI, 1980; KROM and BERNER, 1981; SUESS, 1981).

LYNN and BONATTI (1965) and BONATTI *et al.* (1971) proposed the postdepositional migration model and indicated that manganese might reprecipitate from the interstitial water of reducing sediment as a carbonate mineral. Through the thermodynamic solubility calculations, LI *et al.* (1969) and KATO (1981) demonstrated that the interstitial waters of deep sea sediments were supersaturated with respect to rhodochrosite ($MnCO_3$). Also authigenic manganese-carbonate phases including calcium and magnesium have been identified in reducing marine sediments (MANHEIM, 1961; CALVERT and PRICE, 1970; SUESS, 1979; PEDERSEN and PRICE, 1982).

Phosphate in interstitial waters of reducing sediments is generally enriched by several orders of magnitude relative to that in normal sea waters. SHOLKOVITZ (1973) stoichiometrically showed that such high concentrations in the anoxic interstitial waters resulted from the decomposition of the planktonic organic matter. Phosphate enrichment, in turn, may be responsible for the phosphatization of fossils of benthonic foraminifera (MANHEIM *et al.*, 1975), and the thermodynamic calculations also suggested that iron- and calcium-phosphate could precipitate from the interstitial waters of reducing marine sediments (BRAY *et al.*, 1973; TROUP *et al.*, 1974; BERNER, 1974; MARTENS *et al.*, 1978; MURRAY *et al.*, 1978; KATO, 1981).

Some of manganese and phosphate released into interstitial water diffuse and advect into overlying sea water with the results of sharp

* Received March 17, 1982
** Kurakuen Junior High School, Kurakuen, Nishinomiya, 662 Japan
*** Faculty of Marine Science and Technology, Tokai University, Orido 1000, Shimizu, Shizuoka, 424 Japan

concentration gradients and sedimentation. The chemical composition of the overlying sea water may be greatly affected by these upward fluxes across the sediment-water interface. SAYLES (1979) indicated that in pelagic sediments, during diagenetic processes, several elements were added or subtracted from sea water at the rates that were of the same order of magnitude as the rates at which they were loaded from rivers into oceans.

The purpose of this paper is to elucidate the early diagenesis of manganese and phosphorus in the reducing nearshore sediments from Suruga Bay based on the knowledges obtained by the application of the diagenetic model (as BERNER, 1971) to their distributions in the interstitial waters and, at the same time, to estimate their upward fluxes across the sediment-water interface.

2. Materials and Methods

Three sediment cores used in this study were collected in Suruga Bay. During the cruise BO-80-12 by R/V Bosei Maru-II in August 1980, a 113 cm core sample was collected at Stn. 4 (35°03.8′N, 138°45.6′E, water depth 530 m). Two core samples, 93 cm and 90 cm length, were obtained at C-3 (34°39.7′N, 138° 23.8′E, water depth 480 m) and C-2-2 (34°46.4′N, 138°26.5′E, water depth 857 m) during the cruise TO-80-21 by R/V Tokai Daigaku Maru-II in November 1980. All of core samples were collected by using a gravity corer with a plastic inner tube (8 cm diameter). The sampling sites are shown in Fig. 1.

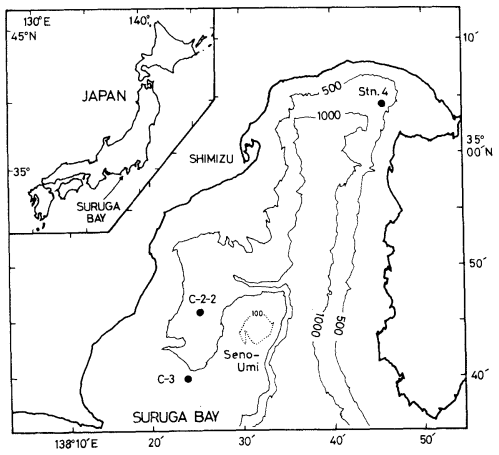

Fig. 1. Sampling sites of nearshore sediments from Suruga Bay, Japan.

Stn. 4 is located off the estuary of Kano River and just at the continental slope topographically. The general color of this sediment core was olivish gray in the upper 0-5 cm layer. C-3 is located in the basin at the southwest of Seno-Umi and the general appearence of its sediment was brownish gray at the upper 0-20 cm layer and olivish gray throughout the rest of about 70 cm. C-2-2 is also located in West Seno-Umi Basin and the general appearence of its sediment was olivish gray throughout the rest of 80 cm. In these three sediments, there was not the odor of hydrogen sulfide. MATSUMOTO and KINOSHITA (1978) reported that the sedimentation rate at the site of C-3 was 0.17 cm yr^{-1} by Pb-210 method.

The core sample of Stn. 4 was sectioned to 5 cm divisions. Each of them was put into thin bags filled with nitrogen gas to avoid air oxidation (ODA *et al.*, 1979) and was stored in a 0-1°C walk-in incubator and then transported to our land laboratory. C-3 and C-2-2 core samples were sectioned in the same ways as the case of Stn. 4. Each of them was also stored in an about 5°C walk-in refrigerator but was not sealed with nitrogen gas because of the short voyage.

Interstitial waters were gently squeezed in a 0-1°C walk-in incubator by using the squeezer of MANHEIM (1968) slightly modified in our laboratory (ODA *et al.*, 1979).

Manganese was directly measured by using an atomic absorption spectrophotometer (Hitachi Model 170-50A), and phosphate was colorimetrically analyzed by molybdenum blue method (GRASSOFF, 1976). The analytical errors for manganese and phosphate measurements were $\pm 2\%$ and $\pm 5\%$, respectively.

3. Results and Discussion

3-1. Manganese

Manganese distributions in the interstitial waters at Stn. 4, C-3 and C-2-2 are summarized in Fig. 2. Manganese concentration at Stn. 4 is approximately constant at 7.9 μM l^{-1}, which is several hundred times higher than dissolved manganese concentration of 0.02 μM l^{-1}, reported

by KIKUYA (private communication), in the deep sea water of Suruga Bay. A concentration peak might be observed at the upper 0–15 cm if manganese in the interstitial waters of such layer had been measured, as mentioned for the following case of C-3.

In the upper 0–5 cm of C-3, manganese concentration shows the maximum of 57 μM l^{-1}, and it decreases to 8.2 μM l^{-1} at the depth of 20 cm. Below this depth, manganese concentration remains approximately constant. Therefore, its distribution pattern indicates that the layer of 0–5 cm may be the reducing zone where manganese oxides are rapidly reduced to Mn(II) accompanying the bacterial decomposition of organic matter. The formation of authigenic manganese carbonate such as rhodochrosite in greater depths of this core may be responsible for the decrease in manganese concentration at the depth of 5–20 cm, if the interstitial water was oversaturated with respect to such a mineral (LI *et al.*, 1969).

Manganese concentration of C-2-2 is much higher than those in the interstitial waters of other two cores. Manganese gradually increases with depth and shows the maximum of 81 μM l^{-1} at the depth of 70–75 cm and the mean concentration is 48.8 μM l^{-1}. The authigenic manganese carbonate may form at greater depths below 80 cm in this core.

3-2. Phosphate

Phosphate distributions in interstitial waters are shown in Fig. 3. Phosphate concentrations at the depth of 0–10 cm of Stn. 4 are from 6.27 μM l^{-1} to 6.93 μM l^{-1}, which are about three times higher than that in the overlying sea water (2.8 μM l^{-1}). Below 30 cm depth, phosphate increases from 2.3 μM l^{-1} to 15 μM l^{-1}. In C-3, phosphate concentrations in the upper 30 cm are nearly equal to that in the overlying

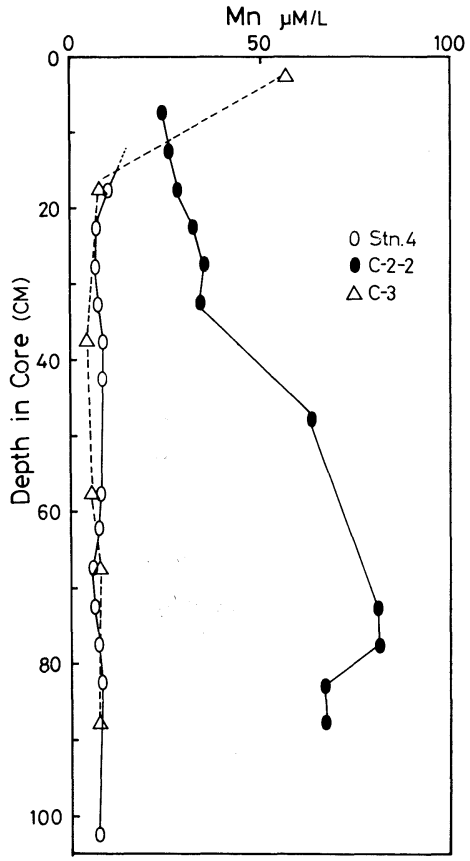

Fig. 2. Manganese in the interstitial waters at Stns. 4, C-3 and C-2-2.

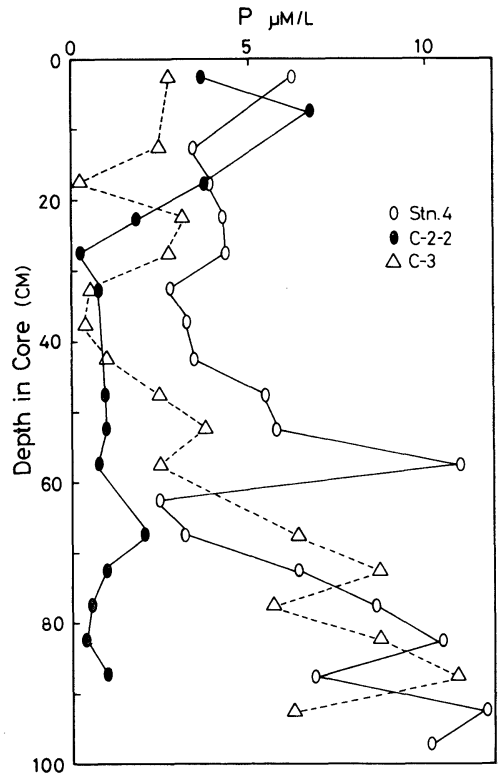

Fig. 3. Phosphate in the interstitial waters at Stns. 4, C-3 and C-2-2.

sea water. Below 40 cm depth, however, phosphate linearly increases from 0.37 μM l^{-1} to 9.89 μM l^{-1} with depth. In these two cores, the decomposition of the planktonic organic phosphorus may be more active in the lower parts of the sediments.

On the other hand, phosphate in C-2-2 increases to the maximum of 6.81 μM l^{-1} from the top to 10 cm depth. Then, it gradually decreases to reach the constant value of 0.98 μM l^{-1} below 23 cm depth. As mentioned earlier, the increase in the upper 0-10 cm may be due to the decomposition of the organic phosphorus, and the decrease at the depth of 10-23 cm may be caused by the predominant precipitation of authigenic phosphorous minerals such as iron- and/or calcium-phosphate.

3-3. Diagenetic Models of Manganese and Phosphate

We discuss the diagenesis of manganese and phosphate in the sediments based on the knowledges obtained by the application of the mass transport models, so-called the diagenetic models. The diagenetic equations have been developed by BERNER (1971, 1980) and LERMAN (1979) in order to interpret the geochemical behaviors of elements in natural sediments. Then, in this paper, we estimate the authigenic mineral precipitation rate constants and the upward fluxes for dissolved manganese and phosphate, applying those diagenetic equations to their distributions in the interstitial waters.

The basic assumptions to apply to the diagenetic equations are follows; sedimentary processes and diagenesis are in steady state, porosity of sediment is constant and chemical reactions (reduction, decomposition, precipitation, etc.) occur via first order kinetics.

Manganese

As described earlier, in the sediment core of C-3, the upper layer of 0-5 cm may be the reducing zone where manganese oxides are reduced to manganous ions, and in the lower the decrease in dissolved manganese may be caused by the predominant precipitation of manganese carbonate with the increase in dissolved carbon dioxide accompanying the bacterial decomposition of the sedimentary organic matter. Therefore, the major processes controlling the dissolved manganese concentration are diffusion, advection, manganese oxide reduction and authigenic mineral precipitation.

The appropriate diagenetic equations are;

$$-\omega\frac{\partial(Mn)_s}{\partial x}-k_{s,\,Mn}(Mn)_s=0, \qquad (1)$$

$$D_s\frac{\partial^2 C}{\partial x^2}-(1+K)\omega\frac{\partial C}{\partial x}+k_{s,\,Mn}(Mn)_s-k_{m,\,Mn}(C-C_{eq})=0, \qquad (2)$$

where C is concentration of dissolved manganese and C_{eq} is that at equilibrium with a given manganese mineral, $(Mn)_s$ is concenration of manganese oxide in sediment, D_s is molecular diffusion coefficient for manganese in interstitial water, K is equilibrium adsorption constant for manganese ion (for details; Berner, 1976), $k_{s,\,Mn}$ and $k_{m,\,Mn}$ are rate constants for manganese oxide reduction and manganese mineral precipitation, respectively, ω is sedimentation rate and x is depth in core. Using these equations, KATO (1981) has already discussed the diagenesis of manganese in hemi-pelagic deep sea sediments.

Assuming that the initial and boundary conditions are;

$$(Mn)_s=(Mn)_{s,\,0} \text{ and } C=C_0 \text{ at } x=0,$$
$$(Mn)_s\to 0 \text{ and } C\to C_{eq} \text{ as } x\to\infty,$$

the solutions of Eqs. (1) and (2) are follows;

$$(Mn)_s=(Mn)_{s,\,0}\exp\left(-\frac{k_{s,\,Mn}}{\omega}x\right), \qquad (3)$$

$$C=C_{eq}-\left\{\frac{k_{s,\,Mn}(Mn)_{s,\,0}\omega^2}{D_s k^2_{s,\,Mn}+\omega^2(1+K)k_{s,\,Mn}-\omega^2 k_{m,\,Mn}}\right\}\times\exp\left(-\frac{k_{s,\,Mn}}{\omega}x\right)+\left\{C_0-C_{eq}+\frac{k_{s,\,Mn}(Mn)_{s,\,0}\omega^2}{D_s k^2_{s,\,Mn}+\omega^2(1+K)k_{s,\,Mn}-\omega^2 k_{m,\,Mn}}\right\}\times\exp\left[\frac{(1+K)\omega}{2D_s}-\frac{1}{2}\sqrt{\left\{\frac{(1+K)\omega}{D_s}\right\}^2+\frac{4k_{m,\,Mn}}{D_s}}\right]. \qquad (4)$$

On the other hand, the empirical expression with respect to the actual data of manganese in the interstitial waters of C-3 can be statistically

obtained, and that is;

$$C=7.0-98.5\exp(-2.14\,x)+93.1\exp(-0.249\,x), \quad (5)$$

where C is in μM l^{-1} and the curve of Eq. (5) is illustrated in Fig. 4 with the original data of dissolved manganese.

Identification of Eq. (5) with Eq. (4) yields;

$$\frac{k_{s,\,Mn}}{\omega}=2.14\ \mathrm{cm}^{-1}, \quad (6)$$

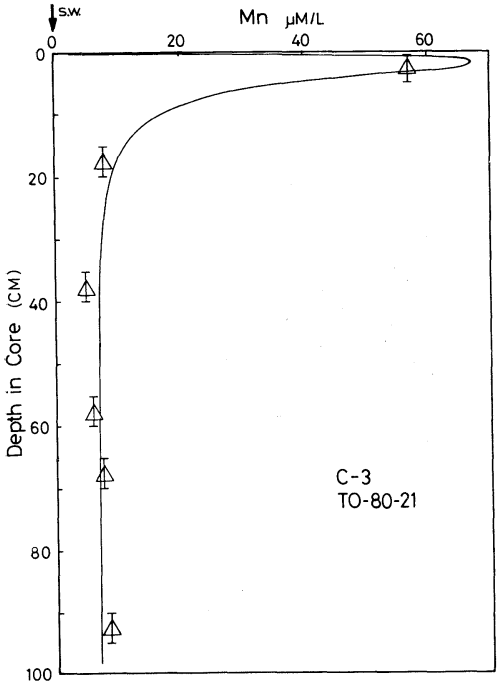

Fig. 4. Manganese in the interstitial water at Stn. C-3. Data are fitted by the expression: $C=7.0-98.5\exp(-2.14\,x)+93.1\exp(-0.249\,x)$, where C is in μM l^{-1}.

$$\frac{(1+K)\omega}{2D_s}-\frac{1}{2}\sqrt{\left\{\frac{(1+K)\omega}{D_s}\right\}^2+\frac{4k_{m,\,Mn}}{D_s}}=-0.249\ \mathrm{cm}^{-1}, \quad (7)$$

$$\frac{k_{s,\,Mn}(Mn)_{s,\,0}\,\omega^2}{D_s k^2{}_{s,\,Mn}+\omega^2(1+K)k_{s,\,Mn}-\omega^2 k_{m,\,Mn}}=93.1\ \mu\mathrm{M\,l}^{-1}. \quad (8)$$

Now, the sedimentation rate, ω, is 0.17 cm yr^{-1} at this site (MATSUMOTO and KINOSHITA, 1978). The diffusion coefficient and the equilibrium adsorption constant for manganese ion are assumed to be equal to that for calcium ion, so that we have $D_s=48.8$ cm^2 yr^{-1} and $K=1.4$ from the experimental data by LI and GREGORY (1974). Using these values, we can obtain from Eqs. (6), (7) and (8);

$k_{s,\,Mn}=0.36$ yr^{-1},
$k_{m,\,Mn}=3.1$ yr^{-1},
$(Mn)_{s,\,0}=56\ \mu$M cm^{-3} by interstitial water
$=11000$ ppm by dry sediment
(porosity $=0.9$).

These results are summarized in Table 1.

The values of $k_{m,\,Mn}$ and $k_{s,\,Mn}$ are about three and four orders of magnitude larger than that for the deep sea sediments reported by KATO (1981), respectively, whereas the $k_{s,\,Mn}$ value is about one-twentieth of that estimated for the shallow water sediments by ELDERFIELD (1976). This suggests that the diagenetic reactions of manganese (reduction of the oxides and precipitation from interstitial water) may rapidly proceed at least in nearshore sediments relative to in deep sea sediments. On the other hand, such high value of $(Mn)_{s,\,0}$ estimated for dry sediment might be found in pelagic sediments

Table 1. Reaction rate constants (yr^{-1}) and surface concentrations (ppm) of manganese and organic phosphorus in the Suruga Bay sediments.

Manganese (C-3)			Phosphorus (C-2-2)			References
k_s	k_m	$(M_n)_{s,\,0}$	k_s	k_m	$\alpha_p G_{p,0}$	
0.4	3.1	11000	0.040	2.3	400	in this study
0.0173						HOLDREN *et al.* (1975)[1]
8.2–9.6	1.2–5.5×10^{-2}					ELDERFIELD (1976)[2]
2.9–3.7×10^{-5}	1.0–3.3×10^{-3}					KATO (1981)[3]
			0.30			BERNER (1974)[4]
			0.006			KROM and BERNER (1981)[4]

1) Chesapeake Bay, 2) Loch Fyne, 3) Japan Sea Basin, 4) Long Island Sound.

(GOLDBERG and ARRHENIUS, 1958). Whereas, total manganese content in the surface sediments near this site was only about 500 ppm (MATSUMOTO and KINOSHITA, 1978). Therefore, this means that the greater part of sedimentary manganese is reducible and is dissolved rapidly in top few centimeters of this core.

Phosphate

Phosphate concentration of C-2-2 increases to give the maximum and sharply decreases with depth. The increase in the upper layer is due to the mineralization of organic phosphorus and the decrease in the lower part may result from the precipitation of authigenic phosphorous minerals. The major processes controlling phosphate concentration are similar to that for manganese, but the term of the reduction is replaced by that of organic matter decomposition.

The appropriate diagenetic equations are;

$$-\frac{\partial G_p}{\partial x}-k_{s,p}G_p=0, \qquad (9)$$

$$D_s\frac{\partial^2 C}{\partial x^2}-(1+K)\omega\frac{\partial C}{\partial x}+\alpha_p k_{s,p}G_p-k_{m,p}(C-C_{eq})=0, \qquad (10)$$

where G_p is concentration of metabolizable organic matter in terms of carbon in sediment, α_p is the atomic ratio of P/C in the organic matter, $k_{s,p}$ is rate constant for organic phosphorus decomposition, and other symbols are represented by phosphate as those in Eq. (2) by manganese.

Under the following conditions;

$G_p=G_{p,0}$ and $C=C_0$ at $x=0$,

$G_p\to 0$ and $C\to C_{eq}$ as $x\to\infty$,

the solutions of Eqs. (9) and (10) are follows;

$$G_p=G_{p,0}\exp\left(-\frac{k_{s,p}}{\omega}x\right), \qquad (11)$$

$$C=C_{eq}-\left\{\frac{\alpha_p k_{s,p}G_{p,0}\omega^2}{D_s k^2_{s,p}+\omega^2(1+K)k_{s,p}-\omega^2 k_{m,p}}\right\}\times\exp\left(-\frac{k_{s,p}}{\omega}x\right)+\left\{C_0-C_{eq}+\frac{\alpha_p k_{s,p}G_{p,0}\omega^2}{D_s k^2_{s,p}+\omega^2(1+K)k_{s,p}-\omega^2 k_{m,p}}\right\}\times\exp\left[\frac{(1+K)\omega}{2D_s}-\frac{1}{2}\sqrt{\left\{\frac{(1+K)\omega}{D_s}\right\}^2+\frac{4k_{m,p}}{D_s}}\right]. \qquad (12)$$

On the other hand, phosphate concentrations of C-2-2 are fitted by the following equation;

$$C=1.0-32.5\exp(-0.238x)+34.3\exp(-0.143x), \qquad (13)$$

where C is in μM l^{-1} and the curve of Eq. (13) is also illustrated in Fig. 5.

Identification of Eq. (13) with Eq. (12) yields;

$$\frac{k_{s,p}}{\omega}=0.238\ \mathrm{cm}^{-1}, \qquad (14)$$

$$\frac{(1+K)\omega}{2D_s}-\frac{1}{2}\sqrt{\left\{\frac{(1+K)\omega}{D_s}\right\}^2+\frac{4k_{m,p}}{D_s}}=-0.143\ \mathrm{cm}^{-1}, \qquad (15)$$

$$\frac{\alpha_p k_{s,p}G_{p,0}\omega^2}{D_s k^2_{s,p}+\omega^2(1+K)k_{s,p}-\omega^2 k_{m,p}}=34.3\ \mu\mathrm{M\,l}^{-1}. \qquad (16)$$

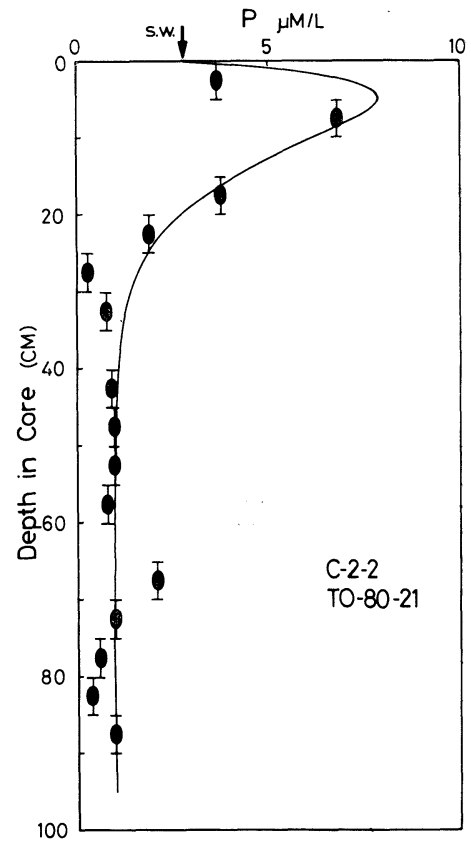

Fig. 5. Phosphate in the interstitial water at Stn. C-2-2. Data are fitted by the expression: $C=1.0-32.5\exp(-0.238x)+34.3\exp(-0.143x)$, where C is in μM l^{-1}.

Now, the sedimentation rate at this site is assumed to be equal to that of C-3 and the other constants for phosphate are selected as follows; $D_s=113\,\mathrm{cm^2\,yr^{-1}}$ and $K=1.8$ (KROM and BERNER, 1980), and $\alpha_p=0.009$ (REDFIELD *et al.*, 1963). Using these values, from Eqs. (14), (15) and (16) we can obtain;

$$k_{s,p}=0.04\,\mathrm{yr^{-1}},$$
$$k_{m,p}=2.3\,\mathrm{yr^{-1}},$$
$$G_{p,0}=390\,\mu\mathrm{M\,cm^{-3}}\ \text{by interstitial water},$$

and these results are also summarized in Table 1.

The $k_{s,p}$ values estimated in coastal anoxic marine sediments, Long Island Sound (BERNER, 1974; KROM and BERNER, 1981), are one order of magnitude larger and about two orders of magnitude smaller than this, respectively. Then, the value of $k_{s,p}$ may be fluctuated by the kind of sediments.

The term, $\alpha_p G_{p,0}$, represents the metabolizable organic phosphorus content in the top of C-2-2. Assuming that porosity and average density of sediment particles are 0.9 and $2.5\,\mathrm{g\,cm^{-3}}$, respectively, $\alpha_p G_{p,0}$ becomes $13\,\mu\mathrm{M\,g^{-1}}$ for dry sediment. Furthermore, if $\alpha_p=0.009$, the metabolizable organic carbon content in the top of the core becomes 1.7% by dry weight.

Unfortunately, we do not have the other information of $k_{m,p}$ in sediments during early diagenesis, except for the values in the Deep Sea Drilling Project sites reported by LERMAN (1979).

Upward Fluxes

Flux of mass through interstitial water can be generally described by the following relationship (BERNER, 1980). At the sediment-water interface, that is;

$$J_0=-\phi_0 D_s\left(\frac{\partial C}{\partial x}\right)_0+\phi_0\omega C_0\,, \qquad (17)$$

where J and ϕ are flux and porosity, respectively, and subscript 0 denotes the sediment-water interface ($x=0$).

Here, ϕ_0 is also assumed to be 0.9 and the other constants are given earlier. The concentration gradient, $\left(\frac{\partial C}{\partial x}\right)_0$, of manganese and phosphate can be obtained from direct differentiations of Eqs. (5) and (13). In Eq. (17), however, the advective term can be almost ignored. Then, the results of the calculations are listed in Table 2.

Table 2. Upward fluxes of dissolved manganese and phosphate across the sediment-water interface in Suruga Bay ($\mu\mathrm{M\,cm^{-2}\,yr^{-1}}$).

Manganese (C-3)	Phosphate (C-2-2)	
8.3	0.28	in this study
7.3	6.6	Narragansett Bay[1]
	1.0	interior shelf[2]
8×10^{-4} [3]	0.13[2]	whole ocean

1) MCCAFFREY *et al.* (1980), 2) MORSE (1979), 3) MANHEIM (1976).

According to Table 2, the upward flux of manganese in C-3 is nearly equal to that in coastal reducing sediment. However, this value is distinctly different from that for the whole ocean. The diffusive flux of manganese, 8×10^{-4} $\mu\mathrm{M\,cm^{-2}\,yr^{-1}}$, estimated for the whole ocean corresponds to 40% of its annual flux entering the ocean from rivers and streams (MANHEIM, 1976). Therefore, it is suggested that manganese concentrations in the overlying sea waters in Suruga Bay may be considerably influenced by its diagenetic upward flux from sediments.

On the other hand, the upward flux of phosphate in C-2-2 is estimated to be $0.28\,\mu\mathrm{M\,cm^{-2}\,yr^{-1}}$. This value falls between $0.13\,\mu\mathrm{M\,cm^{-2}\,yr^{-1}}$ for the whole ocean and $6.6\,\mu\mathrm{M\,cm^{-2}\,yr^{-1}}$ in the coastal sediment. It seemed that the concentration gradients in the upper portion of interstitial water is influenced by the activities of organisms in the sediment.

In these diagenetic model, the effects of burrowing organisms, current stirring and porosity gradients on the diagenetic processes of elements in the sediments are not considered. For example, VANDERBOUGHT *et al.* (1977a) emphasized that the bulk diffusion coefficients of dissolved elements became about 100 times higher than the molecular diffusion coefficients due to wave and current stirring. Therefore, the values of the rate constants and upward fluxes may be subject to certain limitations. So the upward fluxes estimated in this study may be the lower limits.

Acknowledgements

We wish to thank Mr. SATO, Department of Marine Mineral Resources in our Faculty, for his advice on sampling. We also wish to thank the staff members of R/V Bosei Maru-II and Tokai Daigaku Maru-II and, especially, we wish to thank Researchers M. HANADA and H. MORIYA for their kind co-operations.

References

BERNER, R. A. (1964): An idealized model of dissolved sulfate distribution in recent sediments. Geochim. Cosmochim. Acta, **28**, 1479-1503.

BERNER, R. A. (1971): Principles of Chemical Sedimentology. McGraw-Hill, New York. 240 pp.

BERNER, R. A. (1974): Kinetic models for the early diagenesis of nitrogen, sulfur, phosphorus, and silicon in anoxic marine sediments. *In*, The Sea, Vol. 5 (ed. E. D. GOLDBERG). Wiley-Interscience, New York. p. 427-450.

BERNER, R. A. (1976): Inclusion of adsorption in the modeling of early diagenesis. Earth Planet. Sci. Lett., **29**, 333-340.

BERNER, R. A. (1977): Stoichiometric models for nutrient regeneration in anoxic sediments. Limnol. Oceanogr., **22**, 781-786.

BERNER, R. A. (1980): Early Diagenesis—A Theoretical Approach. Princeton Univ. Press, Princeton. 241 pp.

BONATTI, E., D. E. FISHER, O. JOENSUU and H. S. RYDEL (1971): Postdepositional mobility of some transition elements, phosphorus, uranium and thorium in deep sea sediments. Geochim. Cosmochim. Acta, **35**, 189-201.

BRAY, J. T., O. P. BRICKER and B. N. TROUP (1973): Phosphate in interstitial waters of anoxic sediments: Oxidation effects during sampling procedure. Science, **180**, 1362-1364.

CALVERT, S. E. and N. B. PRICE (1970): Composition of manganese nodules and manganese carbonates from Loch Fyne, Scotland. Contrib. Mineral. Petrol., **29**, 215-233.

CALVERT, S. E. and N. B. PRICE (1972): Diffusion and reaction profiles of dissolved manganese in the pore waters of marine sediments. Earth Planet Sci. Lett., **16**, 245-249.

DUCHART, P., S. E. CALVERT and N. B. PRICE (1973): Distribution of trace metals in the pore waters of shallow water marine sediments. Limnol. Oceanogr., **18**, 605-610.

ELDERFIELD, H. (1976): Manganese fluxes to the oceans. Mar. Chem., **4**, 103-132.

EMERSON, S., R. JAHNKE, M. BENDER, P. FROELICH, G. KLINKHAMMER, C. BOWSER and G. SETLOCK (1980): Early diagenesis in sediments from the eastern equatorial Pacific. I. Pore water nutrient and carbonate results. Earth Planet. Sci. Lett., **49**, 57-80.

GOLDBERG, E. D. and G. O. S. ARRHENIUS (1958): Chemistry of Pacific pelagic sediments. Geochim. Cosmochim. Acta, **13**, 153-212.

GRASSOFF, K. (1976): Methods of Sea Water Analysis. Verlag Chemie, New York. 317 pp.

HOLDREN, G. R., Jr., O. P. BRICKER, III and G. MATISOFF (1975): A model for the control of dissolved manganese in the interstitial waters of Chesapeake Bay. *In*, Marine Chemistry in the Coastal Environment (ed. T. M. CHURCH). American Chemical Society, Washington, D. C. p. 364-381.

KATO, Y. (1981): Geochemical study of pore water of marine sediments during early diagenesis. Ph. D. thesis, Tokai Univ. 128 pp.

KLINKHAMMER, G. (1980): Early diagenesis in sediments from the eastern equatorial Pacific. II. Pore water metal results. Earth Planet. Sci. Lett., **49**, 81-101.

KROM, M. D. and R. A. BERNER (1980): The diffusion coefficients of sulfate, ammonium, and phosphate in anoxic marine sediments. Limnol. Oceanogr., **25**, 327-337.

KROM, M. D. and R. A. BERNER (1981): The diagenesis of phosphorus in a nearshore marine sediment. Geochim. Cosmochim. Acta, **45**, 207-216.

LERMAN, A. (1979): Geochemical Processes—Water and Sediment Environments. Wiley-Interscience New York. 481 pp.

LI, Y. H., J. BISCHOFF and G. MATHIEU (1969): The migration of manganese in the Arctic Basin sediment. Earth Planet. Sci. Lett., **7**, 265-270.

LI, Y. H. and S. GREGORY (1974): Diffusion of ions in sea water and in deep-sea sediments. Geochim. Cosmochim. Acta, **38**, 703-714.

LYNN, D. C. and E. BONATTI (1965): Mobility of manganese in diagenesis of deep-sea sediments. Mar. Geol., **3**, 457-474.

MANHEIM, F. T. (1961): A geochemical profile in the Baltic Sea. Geochim. Cosmochim. Acta, **25**, 52-70.

MANHEIM, F. T. (1968): Disposable syringe techniques for obtaining small quantities of pore water from unconsolidated sediments. J. Sediment. Petrol., **38**, 666-668.

MANHEIM, F. T. (1976): Interstitial waters of marine sediments. *In*, Chemical Oceanography, Vol. 6, 2nd ed. (ed. J. P. RILEY and R. CHESTER).

Academic Press, London. p. 115-186.

MANHEIM, F. T., G. T. ROWE and D. JIPA (1975): Marine phosphorite formation off Peru. J. Sediment. Petrol., **45**, 243-251.

MARTENS, C. S., R. A. BERNER and J. K. ROSENFELD (1978): Interstitial water chemistry of anoxic Long Island Sound sediments. 2. Nutrient regeneration and phosphate removal. Limnol. Oceanogr., **23**, 605-617.

MATSUMOTO, E. and Y. KINOSHITA (1978): The bottom sediments in Suruga Bay. *In*, Environmental Research in Japan, 1977. Environment Agency, No. 56-2. 42 pp. (with English abstract)

MCCAFFREY, R. J., A. C. MYERS, E. DAVEY, G. MORRISON, M. BENDER, N. LUEDTKE, D. CULLEN, P. FROELICH and G. KLINKHAMMER (1980): The relation between pore water chemistry and benthic fluxes of nutrients and manganese in Narragansett Bay, Rhode Island. Limnol. Oceanogr., **25**, 31-44.

MORSE, J. P. (1979): Fluxes of phosphate from ocean-floor sediments. *In*, Report on the Marine Phosphatic Sediments Work Shop, Feb., 1979, Honolulu, Hawaii (ed. W.C. BURNETT and R.P. SHELDON). Resource Systems Institute, East-West Center, Hawaii. p. 22.

MURRAY, J. W., V. GRUNDMANIS and W. M. SMETHIE, Jr. (1978): Interstitial water chemistry in the sediments of Saanich Inlet. Geochim. Cosmochim. Acta, **42**, 1011-1026.

NISSENBAUM, A., B. J. PRESLEY and I. R. KAPLAN (1972): Early diagenesis in a reducing fjord, Saanich Inlet, British Columbia—I. Chemical and isotopic changes in major components of interstitial water. Geochim. Cosmochim. Acta, **36**, 1007-1027.

ODA, H. (1980): Study on chemical diagenesis of zinc in interstitial water in pelagic sediments. J. Fac. Mar. Sci. Technol. Tokai Univ., **13**, 29-97. (with English abstract)

ODA, H., Y. KATO and S. OKABE (1980): Transition metals in interstitial water in marine sediments. *In*, The Kuroshio IV: Proc. 4th Symp. Co-operative Study of the Kuroshio and Adjacent Regions (Chairman A.Y. TAKENOUTI), Feb., 1979, Tokyo, Japan. p. 415-431.

PEDERSEN, T. F. and N. B. PRICE (1982): The geochemistry of manganese carbonate in Panama Basin sediments. Geochim. Cosmochim. Acta, **46**, 59-68.

PRESLEY, B. J., R. R. BROOKS and I. R. KAPLAN (1967): Manganese and related elements in the interstitial water of marine sediments. Science, **158**, 906-910.

PRESLEY, B. J., Y. KOLODNY, A. NISSENBAUM and I. R. KAPLAN (1972): Early diagenesis in a reducing fjord, Saanich Inlet, British Columbia—II. Trace elements distribution in interstitial water and sediment. Geochim. Cosmochim. Acta, **36**, 1073-1090.

REDFIELD, A. C., B. H. KETCHUM and F. A. RICHARDS (1963): The influence of organisms on the composition of sea water. *In*, The Sea, Vol. 2 (ed. M. N. HILL). Wiley-Interscience, New York. p. 26-77.

SAYLES, F. L. (1979): The composition and diagenesis of interstitial solutions—I. Fluxes across the seawater-sediment interface in the Atlantic Ocean. Geochim. Cosmochim. Acta, **43**, 527-545.

SHOLKOVITZ, E. (1973): Interstitial water chemistry of the Santa Barbara Basin sediments. Geochim. Cosmochim. Acta, **37**, 2043-2073.

SUESS, E. (1979): Mineral phases formed in anoxic sediments by microbial decomposition of organic matter. Geochim. Cosmochim. Acta, **43**, 339-352.

SUESS, E. (1981): Phosphate regeneration from sediments of the Peru continental margin by dissolution of fish debris. Geochim. Cosmochim. Acta, **45**, 577-588.

TROUP, B. N., O. P. BRICKER and J. T. BRAY (1974): Oxidation effect on the analysis of iron in interstitial water of recent anoxic sediments. Nature, **249**, 237-239.

TSUNOGAI, S. (1980): Early diagenesis in marine sediment and manganese nodule. Bull. Soc. Sea Water Sci. Japan, **33**, 287-299. (in Japanese)

VANDERBORGHT, J. P., R. WOLLAST and G. BILLEN (1977a): Kinetic models of diagenesis in disturbed sediments. Part 1. Mass transfer properties and silica diagenesis. Limnol. Oceanogr., **22**, 787-793.

VANDERBORGHT, J. P., R. WOLLAST and G. BILLEN (1977b): Kinetic models of diagenesis in disturbed sediments. Part 2. Nitrogen diagenesis. Limnol. Oceanogr., **23**, 794-803.

駿河湾の浅海堆積物中におけるマンガンおよびリンの初期続成過程

西田昭夫，加藤義久，岡部史郎

要旨：駿河湾から還元性の堆積物柱状試料を採取し，その間隙水中のマンガンおよびリン酸塩を分析し，それらの元素の初期続成過程を考察した。

マンガンおよびリン酸塩の分布に続成モデルを適用して解析した結果，マンガンが自生鉱物を生成して沈積する時の速度定数は $3.1\ yr^{-1}$，リン酸塩のそれは $2.3\ yr^{-1}$ であった。したがって，還元されて間隙水中に遊離したマンガンは，深海堆積物の場合と比較して，速やかに間隙水中から除かれ，有機物の分解によって生成したリン酸塩も数カ月で間隙水中から除かれると推察される。また，マンガンおよびリン酸塩の間隙水から海水中へのフラックスは，それぞれ $8.3\ \mu M\ cm^{-2}\ yr^{-1}$ および $0.28\ \mu M\ cm^{-2}\ yr^{-1}$ であった。

La mer 20: 161-168, 1982
Société franco-japonaise d'océanographie, Tokyo

The Ocean Characteristics and Their Change in the Seto Inland Sea*

Tetsuo YANAGI**

Abstract: The ocean characteristics and their change in the Seto Inland Sea were investigated with use of transparency, water temperature and salinity data at six straits in the Seto Inland Sea which were obtained every month from 1964 to 1977. The main water temperature anomaly from the averaged seasonal variation has the same phase in the whole area and has the period of around 5 years. It has its origin in the open sea, particularly in the variation of water temperature of the whole North Pacific. Salinity anomaly has also the same phase in the whole area and has the period of around 3 years. It has its origin in the variation of precipitation in the said area.

1. Introduction

The Seto Inland Sea is a long channel whose length is about 500 km and whose depth is about 30 m (Fig. 1). It has four mouths, Kanmon Str., Hayasui Str., Tomogashima Str. and Naruto Str., whose cross-sectional areas are 0.009 km^2, 1.13 km^2, 0.35 km^2 and 0.025 km^2, respectively. The main influences from open ocean are brought through Hayasui Str. and Tomogashima Str. Tidal currents, residual flows and other flow system have been already reviewed (YANAGI and HIGUCHI, 1979, 1981; YANAGI, 1981). The local ocean characteristics have been shown by the each Prefecture Fisheries Observa-

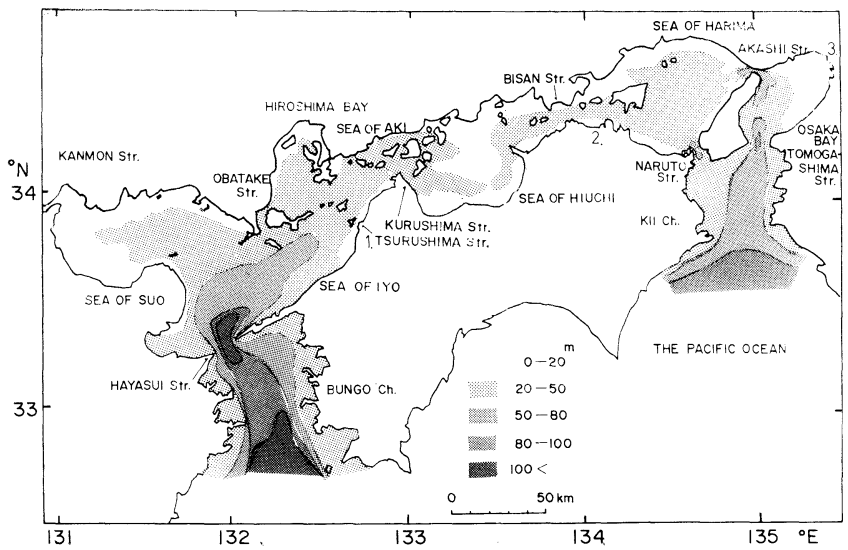

Fig. 1. The Seto Inland Sea. Oceanographic data were obtained at the six straits; Hayasui, Tsurushima, Kurushima, Bisan, Akashi and Tomogashima. Meteorological data were obtained at Matsuyama (1), Takamatsu (2) and Osaka (3).

* Received April 4, 1982
** Department of Ocean Engineering, Faculty of Engineering, Ehime University, Matsuyama, 790 Japan

tory but the whole ocean characteristics and their changes in the Seto Inland Sea have not been shown yet. Moreover the relations between such current system and the characteristics of water temperature and salinity variations have not been made clear. In this paper it is aimed to try to make clear the ocean characteristics and their change in the Seto Inland Sea with use of transparency, water temperature, salinity data and meteorological data.

2. Data used for analysis

Each Prefecture Fisheries Observatory around the Seto Inland Sea carried out observations of water temperature, salinity and transparency at many fixed stations every month from 1964. All data have been compiled by the Fisheries Agency every year. Such data were utilized in this analysis. An example of such data is shown in Fig. 2. As this observation station is situated in Kurushima Str., water temperature and salinity are uniform from the surface to the bottom and they change smoothly all through the year. The data in the straits are suitable for research of the long-term variability of whole area ocean condition, because the straits play

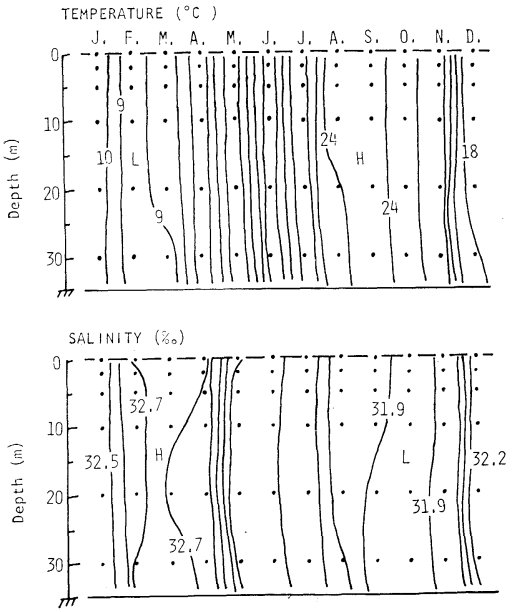

Fig. 2. Vertical distributions of water temperature and salinity at Kurushima Straits from January to December 1977.

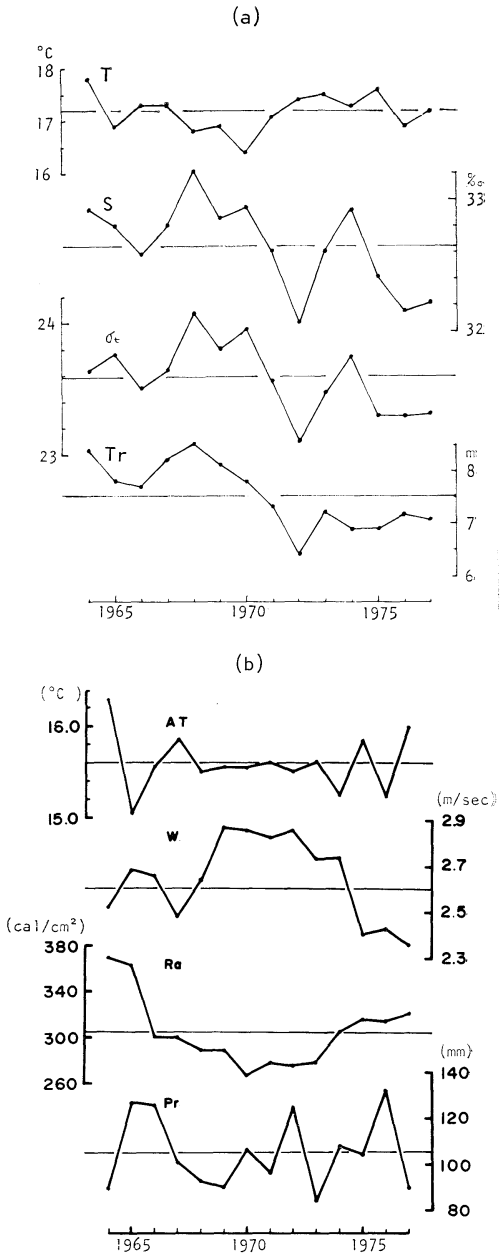

Fig. 3. (a) Year-to-year variations of water temperature (T), salinity (S), water density (σ_t) and transparency (Tr) averaged over the six straits. (b) Year-to-year variations of air temperature (AT), wind velocity (W), total radiation (Ra) and precipitation (Pr) averaged over the three stations.

as a sort of low-pass filter. Here transparency, water temperature and salinity at 10 m depth of the six straits, Hayasui, Tsurushima, Kurushima, Bisan, Akashi and Tomogashima every month from 1964 to 1977 were used.

Since observation days are not predetermined and their distribution is random, a midmonth data are linearly interpolated using pre- and aftermonth data. The meteorological data, monthly mean wind velocity, monthly mean net radiation and monthly accumulated precipitation were collected at the three meteorological observatory, Matsuyama, Takamatsu and Osaka, to investigate the relationships between ocean condition and meteorological one.

3. Year-to-year variability

Variabilities of yearly averaged oceanographic data over six stations and meteorological ones over three stations are investigated (Fig. 3). Water temperature falls down around every 5 or 6 years. This period coincides with the year-to-year valiability of north-Pacific ocean circulation (KORT, 1970). Salinity falls down around every 3 or 4 years. This variability well coincides with that of precipitation, that is, salinity falls down in the year of much precipitation. The variation of water density has more similarity to that of salinity than to that of water temperature. Transparency continues to fall down from 1968 to 1972 but it stagnates from 1973 to 1977. This is due to that the sewage supplement from land rapidly decreased in 1973 as the special law "Protection of Marine Environment in the Seto Inland Sea" was to be effective this year.

4. Seasonal variation

The data were averaged every month in 14 years in order to investigate the averaged

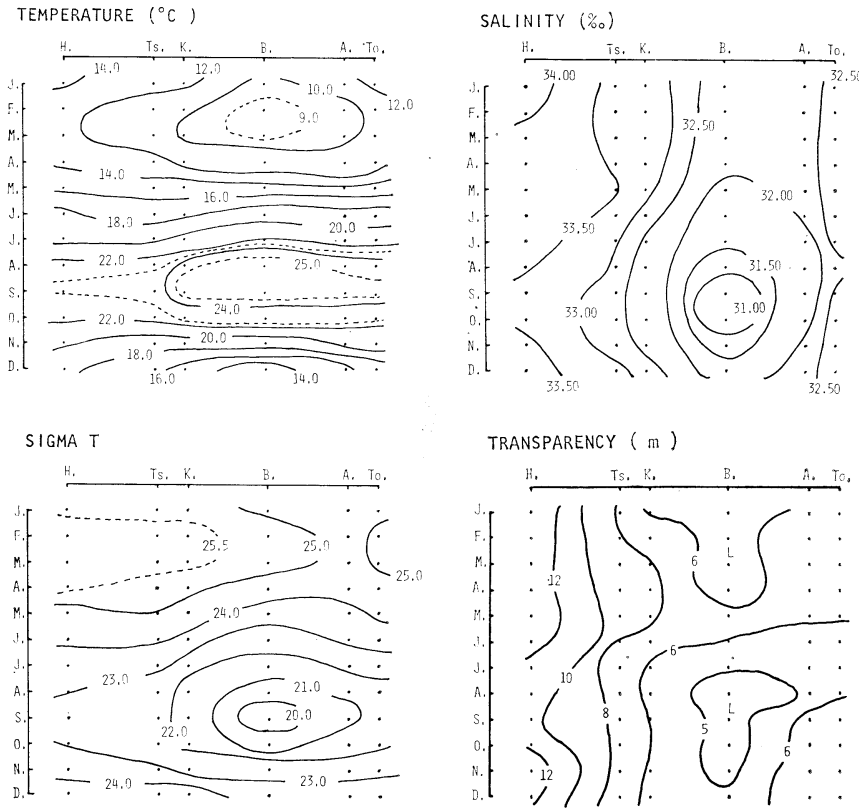

Fig. 4. Averaged seasonal variations of water temperature, salinity, water density σ_t and transparency over 14 years.

seasonal variation (Fig. 4). Water temperature has the whole amplitude of about 16°C at Bisan Str. while it has that of about 10°C at Hayasui Str. The maximum water temperature occurs in September and the minimum one in February. On the other hand, salinity has the whole amplitude of about 1.5‰ at Bisan Str. while it has that of 0.8‰ at Hayasui Str. The maximum salinity occurs in February and the minimum one in September. The variation pattern of water density is placed between that of water temperature and that of salinity. Transparency at Bisan Str. has minimum value in September.

The similar seasonal variation of the meteorological data is shown in Fig. 5. The data is

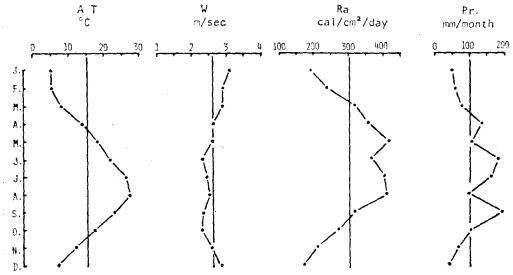

Fig. 5. Averaged seasonal variations of air temperature (AT), wind velocity (W), total radiation (Ra) and precipitation (Pr) over 14 years, averaged over the three stations.

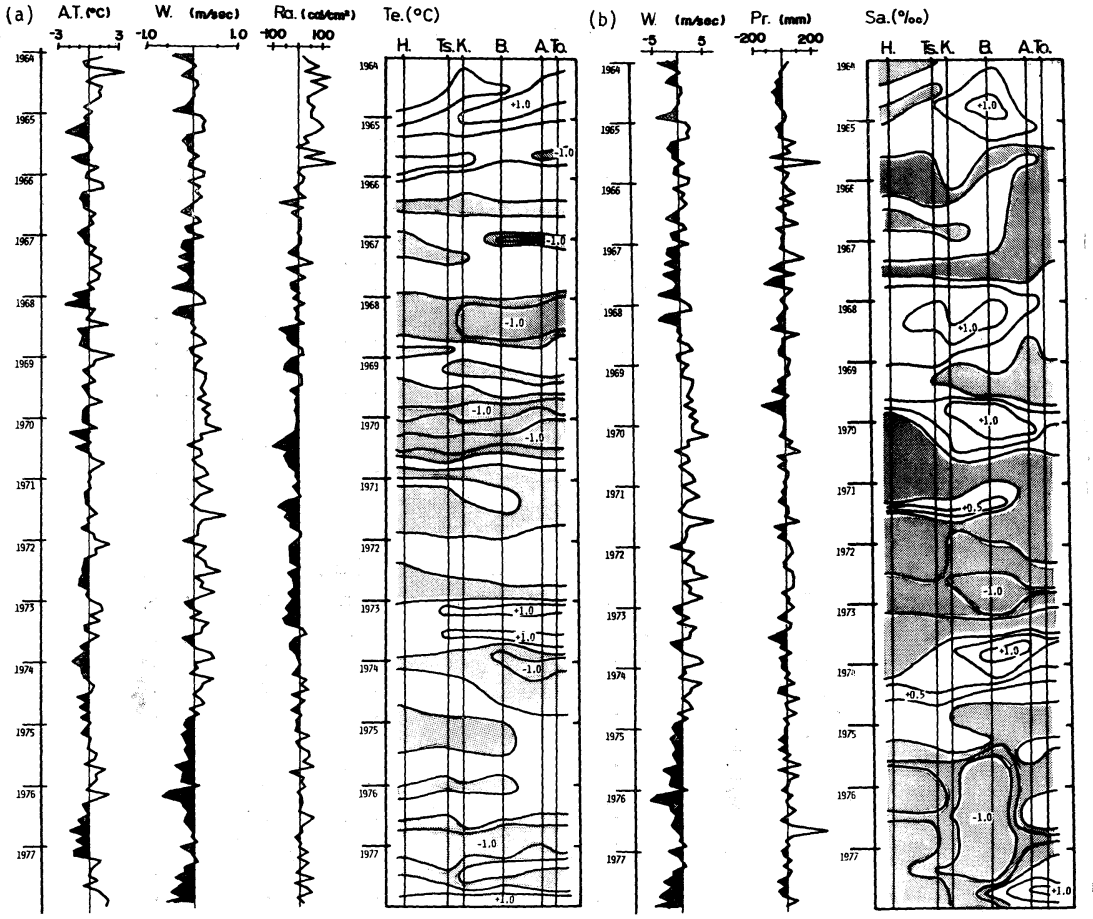

Fig. 6. (a) Anomaly of air temperature (AT), wind velocity (W), radiation (Ra) and water temperature (Te) from averaged seasonal variations. (b) Anomaly of wind velocity (W), precipitation (Pr) and salinity (Sa). Shadow region shows the negative anomaly.

averaged over three stations. The vertical line in the figure shows the yearly averaged value. Air temperature has its minimum value in February and has its maximum value in August. Wind blows rather stronger in winter. Net radiation on a horizontal surface has local minimum value in June due to much cloud in rainy season. Precipitation has large values in April, June, July and September.

5. Anomaly from the averaged seasonal variation

The deviations from the averaged seasonal variation obtained in Section 4 are calculated each month at each station. Similar procedure on meteorological data is also carried out (Fig. 6). The deviation of water temperature has its maximum value at Tomogashima Str. This fact shows that the water temperature anomaly is mainly brought through Kii Channel from the Pacific Ocean. The same anomaly from the Pacific Ocean is thought to be brought through Bungo Channel. However, water temperature anomaly at Bungo Channel is not so large as that at Kii Channel, because the heat capacity of the former is larger than that of the latter. The radiation anomaly rather shows the similar pattern to the water temperature one, that is, the water temperature anomaly and the radiation

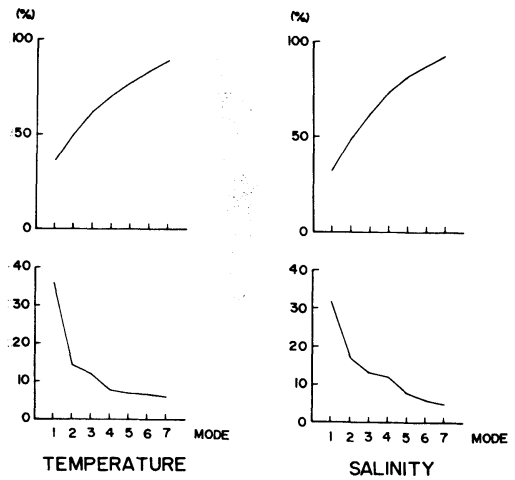

Fig. 7. Accumulated contribution ratio (upper) and each contribution ratio (lower) of each spatial mode of water temperature and salinity variation.

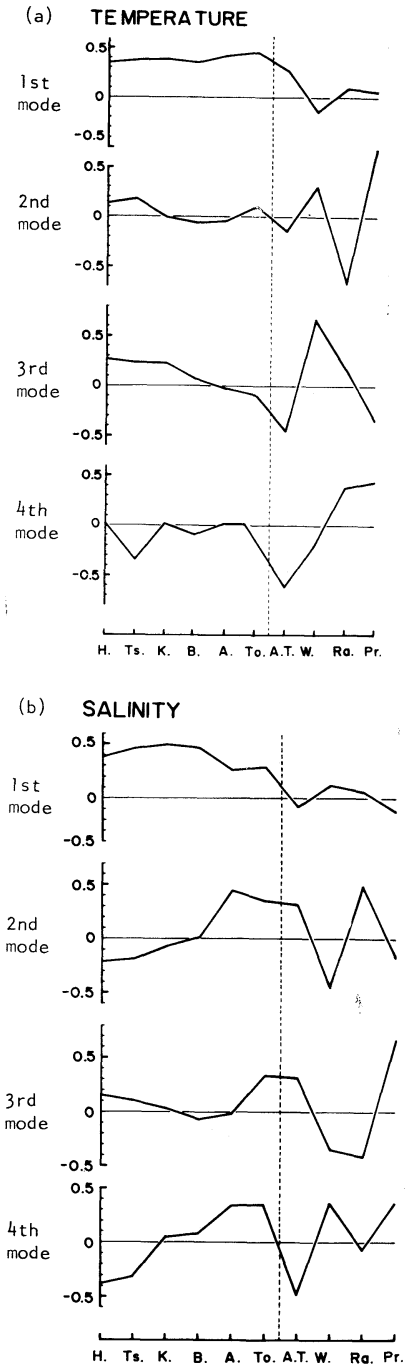

Fig. 8. Spatial distribution of eigen vector of the largest four modes of water temperature and salinity.

one have the negative sense from 1968 to 1973. The radiation anomaly has the anti-phase to the wind velocity one but it has not the distinct relationship to the air temperature one. On the other hand, the salinity anomaly has its maximum value at Bisan Str. The precipitation anomaly shows the similar pattern to the salinity one, that is, the negative anomalies of precipitation in 1964-1965, 1968-1969 and 1973-1974 coincide with the positive anomalies of salinity. This fact shows that the salinity anomaly is mainly due to the precipitation. We may consider that water temperature anomaly has its origin in the open sea and the salinity anomaly has its origin in the inland sea.

6. Principal component analysis

The principal component analysis is carried out in order to investigate the characteristic variabilities of water temperature and salinity and their relations to the meteorological conditions. The cross-correlation coefficient matrix

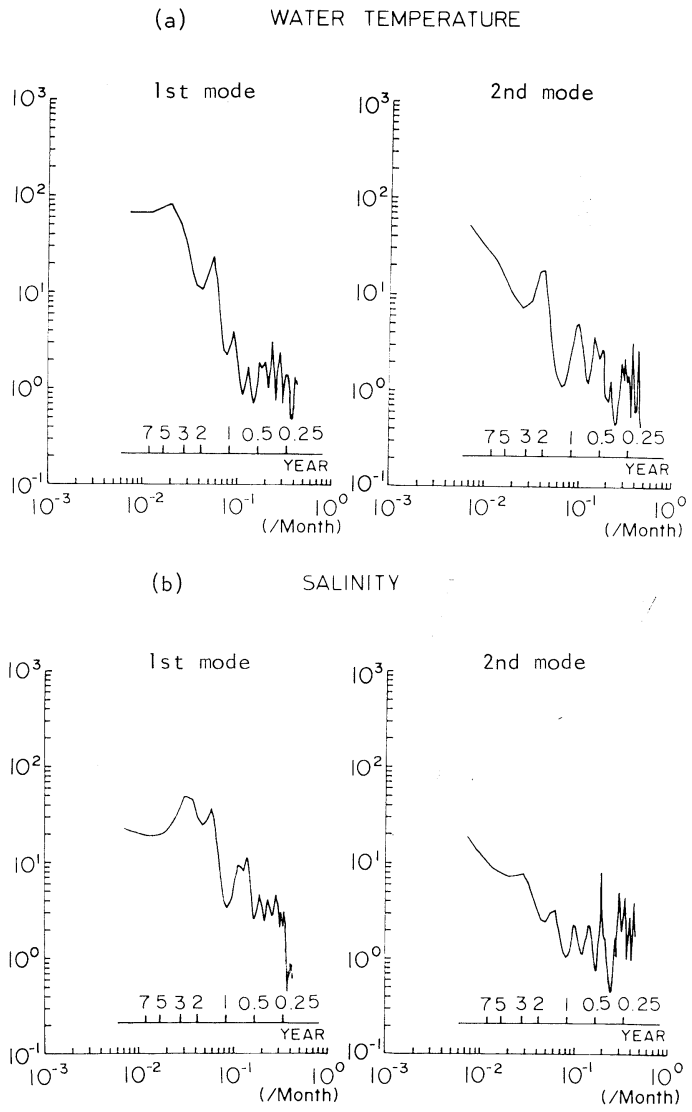

Fig. 9. Power spectra of temporal modes of water temperature and salinity.

$\boldsymbol{R}$ is calculated with use of oceanographic and meteorological data.

$$\boldsymbol{R}=\begin{pmatrix}\gamma_{11} & \cdot & \gamma_{1n}\\ \cdot & \cdot & \cdot\\ \gamma_{n1} & & \gamma_{nn}\end{pmatrix} \qquad (1)$$

$$\gamma_{ij}=\frac{\sigma_{ij}}{\sqrt{\sigma_{ii}\,\sigma_{jj}}} \qquad \sigma_{ij}=\frac{1}{N_t-1}\sum_{t=1}^{N_t} x_{it}\,x_{jt} \qquad (2)$$

Here γ_{ij} denotes the normalized cross-correlation coefficient, σ_{ij} cross-correlation coefficient, i,j observational stations or meteorological factor, t time (month), Nt number of observation 168, that is 12 months times 14 years, x_{it}, x_{jt} the anomaly from the averaged seasonal variation obtained in Section 5. Eigen values and eigen vectors are obtained by Yacobi Method to satisfy the following eigen equation.

$$|\boldsymbol{R}-\lambda\boldsymbol{I}|=0 \qquad (3)$$

Here λ is the eigen value and $\boldsymbol{I}$ eigen vector matrix. We call the spatial mode as each eigen vector. We can obtain ten spatial modes because $\boldsymbol{R}$ is calculated with use of six water temperature or salinity data and four meteorological data. The contribution ratio of each mode to the total variation is estimated by the following formula:

$$C_n=\frac{\lambda_n}{\sum_{n=1}^{10}\lambda_n}\times 100\,.$$

Each contribution ratio C_n and accumulated C_n from 1st to 7th mode in order of larger eigen value are shown in Fig. 7. C_n of 1st mode of water temperature and salinity exceeds 30% and accumulated C_n to 4th mode exceeds 70% in water temperature and 74% in salinity, respectively. Eigen vectors of 1st, 2nd, 3rd and 4th spatial mode are shown in Fig. 8. First mode of water temperature has the positive correlation in the whole area of the Inland Sea and has the negative correlation to the wind velocity. Second mode has the positive correlation in the both ends of the Seto Inland Sea and has the negative correlation in the central part. Third and 4th modes are as shown in Fig. 8(a). First mode of salinity has the positive correlation in the whole area of the Seto Inland Sea and has the negative correlation to air temperature and precipitation. Second mode shows the anti-phase cross-correlation between the eastern part and the weastern part of the Seto Inland Sea.

The temporal variability of each spatial mode is calculated by the following formula;

$$a_{nt}=\sum_{i=1}^{10} x_{it}\,e_{ni}\,.$$

Here we call the temporal mode as a_{nt}. e_{ni} shows the eigen vector of n-th mode at i-th station. After all the deviation from the averaged seasonal variation x_{it} is expressed by the linear combination of each mode;

$$x_{it}=\sum_{n=1}^{10} a_{nt}\,e_{ni}\,.$$

Here both a_{nt} and e_{ni} are linear independent. We estimate the predominant period of temporal variation of each spatial mode by calculation of power spectrum a_{nt} with use of the maximum entropy method. The result is shown in Fig. 9. First mode of water temperature has the spectrum peak at the period of 4.6 years and 2nd mode has that at 2.0 years. On the other hand, 1st mode of salinity has the spectrum peak at the period of 2.8 years and 2nd mode has that at 5.5 months. Third and 4th modes have their spectrum peaks at higher frequencies and do not have any special dominant peak.

7. Discussion

Wide range variabilities of sea condition of the Seto Inland Sea, from their period of 5 or 6 years to several months are studied in detail. The variability of water temperature has the main period of 4.6 years and has the same phase in the whole inland sea. As it has its origin in the open sea, it may be possible to monitor the variability of open sea condition by the continuous observation of water temperature in the coastal area. On the other hand, salinity variability has the main period of 2.8 years and this period coincides with that of precipitation. Salinity variability has its origin in meteorological condition, especially in precipitation of the said area. The time duration of negative salinity anomaly induced by precipitation depends in the water exchange ability in the sea. The residence time of water in the Seto Inland Sea is about

1 year after TAKEOKA (1981). This fact shows that the impact of decreasing salinity every around 3 years lasts about 1 year.

Year-to-year variation pattern of water density well coincides with that of salinity as shown in Fig. 3(a). The averaged seasonal variation pattern of water density is placed between that of water temperature and that of salinity as shown in Fig. 4. These facts show that the basic seasonal variation of water density depends on those of water temperature and salinity but the variation of density anomaly from the seasonal variation mainly depends on that of salinity. As the maximum salinity anomaly reaches about 1‰ and the maximum water temperature anomaly reaches about 1°C as shown in Fig. 6(a) and (b), σ_t changes are expected about 0.8 and 0.2 by these maximum anomalies, respectively. After all we may consider that the variation of density current in the Seto Inland Sea due to density anomaly has more dependency to salinity anomaly than to water temperature anomaly.

Acknowledgements

The author expresses his sincere thanks to Prof. H. HIGUCHI of Ehime University for his encouragement. He also thanks Mr. H. TAKEOKA of Ehime University for his helpful discussions and Mr. Y. MIYAZAKI of Ehime University, who now belongs to Mitsui Residence Construction Co. Ltd., for his assistance in data analysis. The data processing was carried out on a FACOM 230-28 of Ehime University and on a FACOM M-200 of the computor center of Kyushu University. This study is a part of the special project research "The ocean characteristics and their changes" by the Ministry of Education, Science and Culture.

References

FISHERIES AGENCY (1964-1977): Marine Observation Table.

KORT, V. G. (1970): Large-scale sea-air interaction. Okeanol., **10**, 222-240.

METEOROLOGICAL AGENCY (1964-1977): Monthly Weather Data Report.

TAKEOKA, H. (1981): On the concepts of the water exchange and the transfer of matter in the sea. Mem. Ehime Univ., **9**, 287-298. (in Japanese)

YANAGI, T. (1981): A review of the physical processes governing transport and distribution of pollutants in the coastal sea. Mem. Ehime Univ., **9**, 269-281.

YANAGI, T. and H. HIGUCHI (1979): Residual flows in the Seto Inland Sea. Bull. Coast. Oceanogr., **16**, 123-127. (in Japanese)

YANAGI, T. and H. HIGUCHI (1981): Tide and tidal current in the Seto Inland Sea. Proc. 28th Conf. Coast. Engineer., JSCE, p. 555-558. (in Japanese)

瀬戸内海の海況・変動特性

柳　　哲　雄

要旨: 1964年～1977年，毎月1回瀬戸内海の6つの海峡部で得られた透明度，10 m 層の水温・塩分データを用いて，瀬戸内海の海況特性とその変動特性を明らかにした。平均的な季節変動からの水温偏差は全域で同位相，約5年周期の変動が卓越していて，この変動の原因は北部太平洋全域の水温変動に在る。同じく平均的な季節変動からの塩分偏差は全域で同位相，約3年周期の変動が卓越していて，この変動は降雨量の経年変動に起因している。

La mer 20: 169-180, 1982
Société franco-japonaise d'océanographie, Tokyo

Continental Shelf Waves off the Eastern Coast of Korea*

Jae Hak LEE** and Jong Yul CHUNG**

Abstract: Spectral analysis has been made to investigate the effect of the atmospheric pressure on 12-hourly mean sea level at three stations off the eastern coast of Korea.

Our estimated barometric factor indicates that the response of sea level to atmospheric pressure fluctuations is non-barometric in most of the frequency range 0-0.5 cycles per day. In addition, the weighted barometric factor shows seasonal variation. The computed phase shift and the time lag between adjusted sea levels at different stations suggest a trend of a wave propagation at 0.24-0.26 cpd from the north to the south, which is found in summer season only. The predicted phase speed from the nondivergent shelf wave theory, which is based on our bottom profile, i.e., exponential depth profile, well agrees with our observed values. Therefore, through this investigation, it was found that this phenomenon might be interpreted as a continental shelf wave.

1. Introduction

In theory, the sea level reacts as an inverse barometer to the atmospheric pressure change. However it does not always respond barometrically in the coastal region. Continental shelf waves, namely topographic Rossby waves trapped over the continental margin, are one of the essential ingradients of understanding the coastal region phenomena. The continental shelf waves have frequencies less than the local inertial frequency and wavelength much greater than the shelf width. The waves progress parallel to the coast in one direction only, like the classical Kelvin waves. In the northern hemisphere, they travel with their right shoulder against the coast.

SHOJI (1961) observed similar waves with a period of several days, moving along the Japanese shelf. Since HAMON (1962, 1963) first detected continental shelf waves along the Australian coast, the evidence for the existence of continental shelf waves has been accumulated through a series of analyses made from the tide gage records and meteorological records; i.e., the Australian coast (HAMON, 1966, 1967; MYSAK, 1967), the Oregon coast (MOOERS and SMITH, 1968), the North Carolina coast (MYSAK and HAMON, 1969), the Japanese coast (ISOZAKI, 1969), and the Bay of Biscay (LIE, 1979). These waves also have been found in current meter records, of the west coast of Scotland (CARTWRIGHT, 1969), Lake Ontario (CSANADY, 1976), the Florida Strait (SCHOTT and DÜING, 1976; BROOKS and MOOERS, 1977), and the Ghana coast (HOUGHTON, 1979). CUTCHIN and SMITH (1973) also have detected the shelf waves in their spectral analysis of tidal and meteorological records along with the current meter records.

ROBINSON (1964) proposed that the non-equilibrium response observed by HAMON (1962, 1963) was caused by the propagation of barotropic waves, termed continental shelf waves, along the coast. MYSAK (1967) developed a more comprehensive model of shelf waves by including the effect of a continental slope region, deep stratification, and longshore current. ADAMS and BUCHWALD (1969) have shown that the wind stress is the principal driving force, and that the correlation between sea level and pressure change is due to the correlation existing between the changes in wind stress and in pressure. A more general treatment of the problem on the generation mechanism by the wind stress was given by GILL and SCHUMANN

* Received April 17. 1982
Presented at the First JECSS Workshop, June 1981 (cf. La mer, **20**: 37-40, 1982).

** Department of Oceanography, Seoul National University, Seoul 151, Korea

(1974).

The purpose of this study is to investigate the effect of the atmospheric pressure on the sea level along the eastern coast of Korea. The standard techniques of time series analysis have been employed to determine (1) energy peaks at periods of several days, (2) responses of the sea level to the atmospheric pressure fluctuations, and (3) existence of any time lags between the sea levels at pairs of adjacent stations. And also a theoretical analysis has been employed to explain our observed results.

2. Data and its reduction procedure

The locations of tidal stations in this analysis are shown in Fig. 1. Tidal data were obtained by the Hydrographic Office of Korea. For all stations, the hourly data covered the period from April 1, 1978 to April 30, 1979. The tide gage records were read to 1 cm.

The locations of weather stations selected for the present study are also shown in Fig. 1. The data were obtained by the Central Meteorological Office of Korea, covering a period from April 1, 1978 to April 30, 1979 for all the stations. The data consisted of four observations per day at 0600, 1200, 1800 and 2400 UT (Universal Time) and were read to 0.1 mb.

1) Data Reduction Procedure

Sea Levels: The tidal data were fully checked by an error detection technique which uses a low pass numerical filter. The error detection formula is the form;

$$X'_i = 0.75(X_{i-1}+X_{i+1}) - 0.30(X_{i-2}+X_{i+2}) + 0.05(X_{i-3}+X_{i+3}),$$

where X_i and X'_i are the ith original and estimated values, respectively. When the difference $X_i - X'_i$ exceeds 12 cm (predetermined standard deviation), they are replaced by the estimated values.

Tidal effects were eliminated from hourly tide data by using two kinds of numerical filters. The first one is a Cosine-Lanczos filter, as used by MOOERS and SMITH (1968). The filter has the following form;

$$Y_i = (X_i + \sum_{m=1}^{60} f(m)\,(X_{i-m}+X_{i+m}))/G,$$

where $f(m) = (1+\cos \pi m/60)\,(\sin 0.7\pi m/12)/(0.7\pi m/6)$, $G = 1+2\sum_{m=1}^{60} f(m)$, and X_i is the hourly tidal data. This filter acts as a low pass filter with a half-power at 40 hrs (i.e., 0.6 cpd).

The second one is an ideal low pass filter as used by CHUNG (1979). The filter function is given by

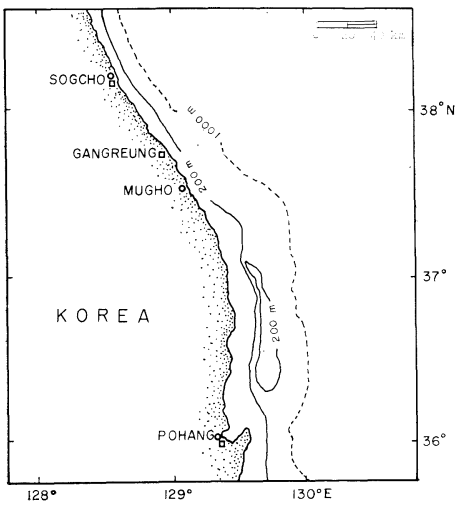

Fig. 1. Location of tidal stations (○) and weather stations (□).

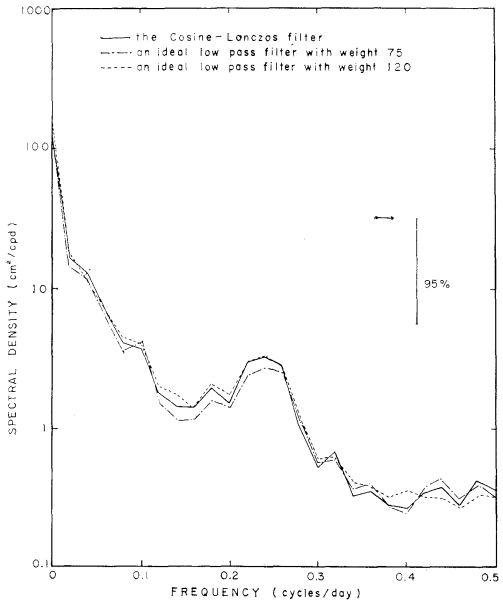

Fig. 2. Spectral density of the adjusted mean sea level at Sogcho in summer.

$$H^{(M)}(\omega)=C_0+2\sum_{m=1}^{M} C_m \cos(m(\omega \Delta t)),$$

where $\omega=2\pi f$ and C_m are smoothed weights. For the comparison with the Cosine-Lanczos filter, the smoothed weights for various M are chosen, giving the results in Fig. 2 along with the results of the Cosine-Lanczos filter.

After filtering, mean sea levels were obtained for every 12 hour centered on 0600 and 1800 UT.

Atmospheric Pressure: The atmospheric pressure data were also fully checked by the error detection formula as used in sea level data. Values deviating from the predetermined amounts (i.e., standard deviation), 1.6 mb, were rejected and they were replaced by the estimated values. For the purpose of estimating 12-hourly mean value, raw data were filtered by a symmetric filter, as used by HAMON (1976); .232 (central weight), .186, .126, .060, and .012. These filter values were chosen to form a low pass filter having approximately a half power point at 54 hrs (i.e., 0.43 cpd) (HAMON, 1976). The mean values were also obtained for every 12 hour centred on 0600 and 1800 UT.

2) Adjusted Sea Level and Final Data Set

According to the hydrostatic hypothesis, the mean sea level responds as an inverse barometer to the atmospheric pressure change. That is, an increase of 1 mb in atmospheric pressure amounts to a decrease in the sea level by 1.01 cm. The adjusted mean sea levels were obtained by adding the atmospheric pressure minus 1015 mb (the approximate average atmospheric pressure) to the corresponding mean sea levels.

Finally, the data sets of sea level and atmospheric pressure were stored in the 180 days record arrays (April 15, 1978 to October 10, 1978 and October 11, 1978 to April 8, 1979 as the summer and winter seasons respectively).

3. Spectral analysis and result

1) Methods of Spectral Estimation

a) The Blackman and Turkey method

This method first involves the calculation of the auto-covariance function, which is then smoothed and Fourier transformed to yield the spectrum. In this study, the spectra comprised 360 data points from 180 days records for each season with a maximum lag of 50 data points. The sampling interval is a half day, so the Nyquist frequency is 1.0 cpd. According to HAMON and HANNAN (1963) and JENKINS and WATTS (1968), the degree of freedom and the bandwidth are given by 8N/3M and 1.333/M (N, data points; M, maximum lags), respectively. Hence the degree of freedom is 19 and the bandwidth is 0.26 cpd in this analysis.

b) FFT method

FFT (Fast Fourier Transformation) technique allows direct calculation of Fourier coefficients of time series data without intermediate estimation of the auto-covariance function. The calculation of the spectra from the raw tidal data has been made by NEWFFT program written by GROSCH and CHUNG (1980). In analyzing 8640 data points taken from 360 days records, we set the number of segment (M) to be 8. Then the number of data points in each segment (N) becomes 1024 and the resolution frequency yields 0.27×10^{-6} Hz with the error bound ($(3/8\,M)^{1/2}$) of 21.7 %. When we analyse 4320 data points from the 180 days records, the number of segment is 8, the number of data in each segment is 512, the resolution frequency is 0.54×10^{-6} Hz, and the error bound is 21.8 %.

2) Autospectrum

Figure 3 through Fig. 8 show the spectral density of the observed sea level, the adjusted sea level, and the atmospheric pressure at the stations observed both for the summer and the winter, respectively. As a measure of statistical significance, the 95 % confidence limits and the corresponding bandwidth are indicated in the figures.

In all the summer spectra (Fig. 3 through Fig. 5), peaks are present in the frequency band we examined. The peaks are significant at 0.24-0.26 cpd for Sogcho and Mugho, at 0.24 cpd for Pohang. These peaks are all found in the observed sea level, the adjusted sea level, and the atmospheric pressure. The spectral frequency band possessing significant peaks of Sogcho and Mugho records implies that the energy density of the adjusted sea level is larger than that of the observed sea level and the atmospheric pressure. The spectral density of zero frequency is found to be extremely high.

It might occur from the fact that the annual term, amplitude about 20 cm, was not removed. So, they might be explained more clearly by analyses of monthly or annual sea level changes. In the winter spectra (Fig. 6 through Fig. 8), small peaks are present. However these peaks are not significant, because they are within the confidence limits. The adjusted sea level spectra show considerable energy peaks, indicating that the isostatic adjustment (1.01 cm/mb) was not

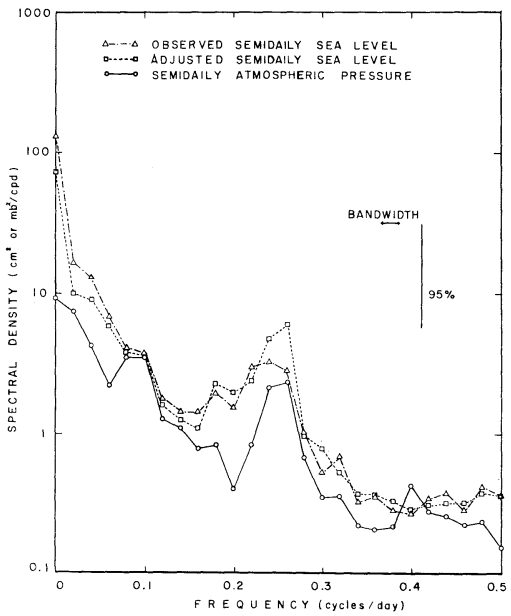

Fig. 3. Spectral density at Sogcho in the summer season.

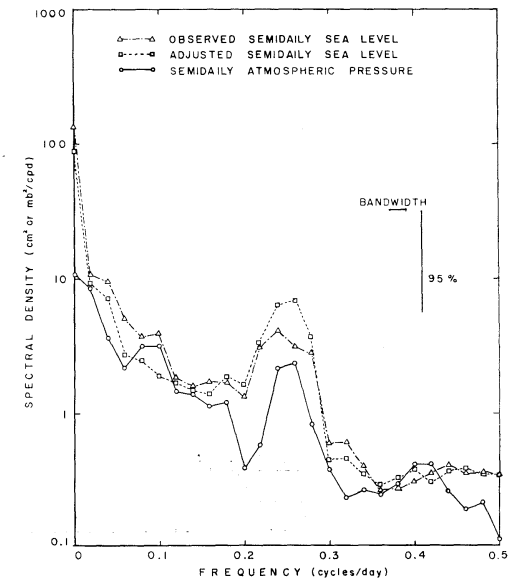

Fig. 4. Spectral density at Mugho, Gangreung in the summer season.

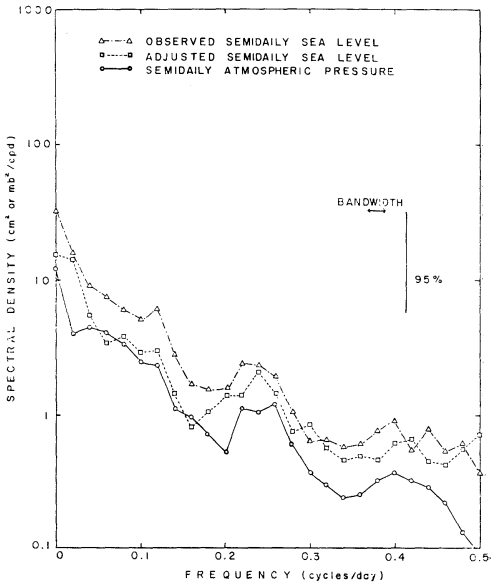

Fig. 5. Spectral density at Pohang in the summer season.

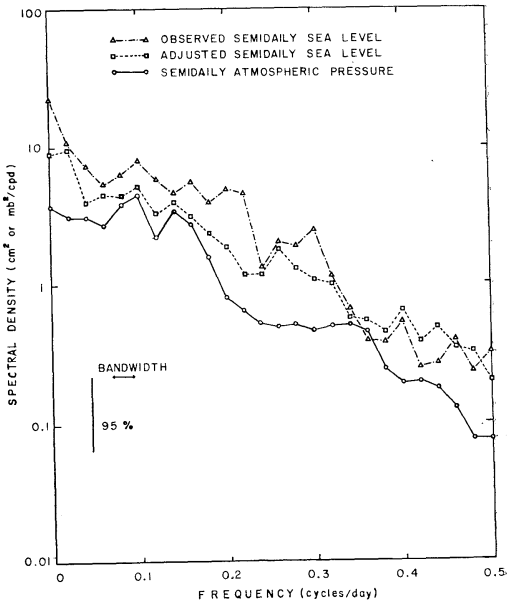

Fig. 6. Spectral density at Sogcho in the winter season.

effective.

Figures 9 and 10 show the spectral density of the raw tidal data processed by FFT. Peaks are found near 0.26 cpd in the summer records except for the part showing tidal periodicities. However, there is no peak at low frequencies for the winter record (Fig. 10). These results are consistent with those shown in Fig. 3 through Fig. 8, which were computed by the Blackman and Turkey method.

3) Barometric Factor

The barometric factor can be determined as a function of frequency. The barometric factor $b(f)$, (i.e., the co-spectrum between the observed sea level and the atmospheric pressure to the autospectrum of the atmospheric pressure),

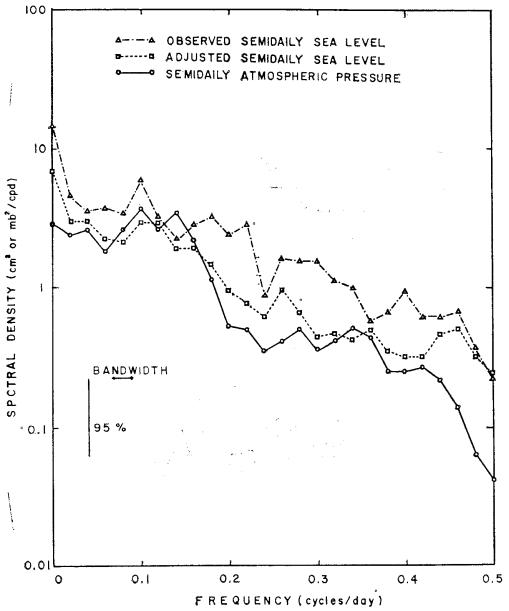

Fig. 7. Spectral density at Mugho, Gangreung in the winter season.

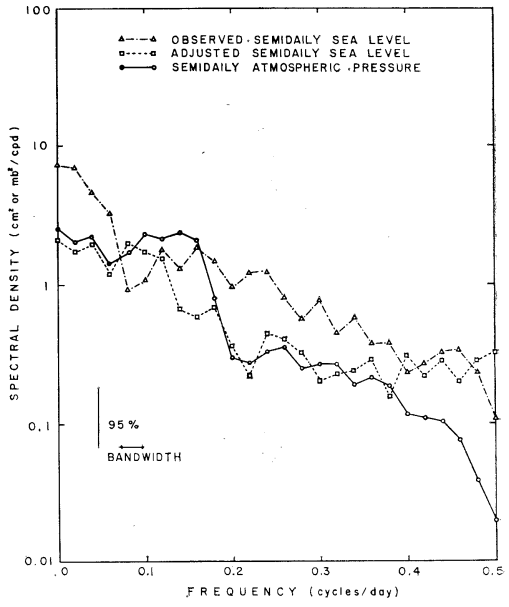

Fig. 8. Spectral density at Pohang in the winter season.

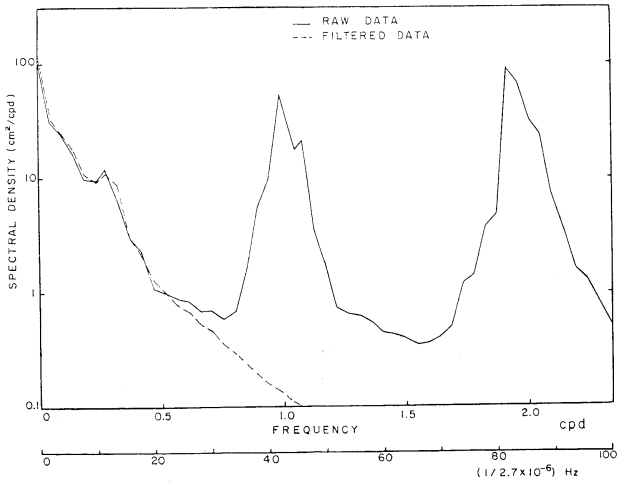

Fig. 9. Spectra of the raw tide data and the filtered data at Sogcho in summer. Filtering function is an ideal low pass filter with weight 120.

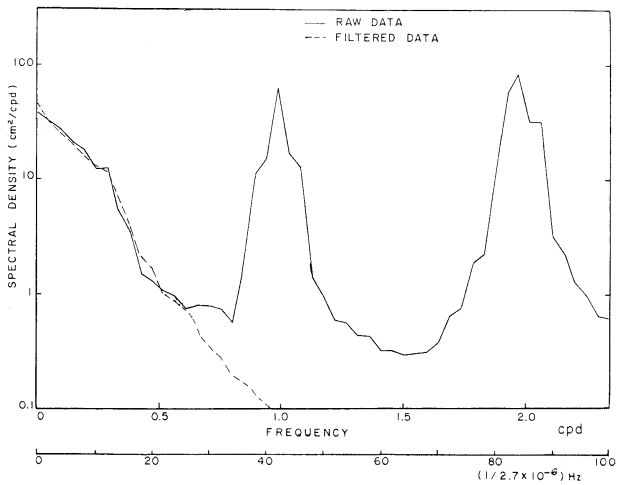

Fig. 10. Spectra of the raw tide data and the filtered data at Sogcho in winter. Filtering function is an ideal low pass filter with weight 120.

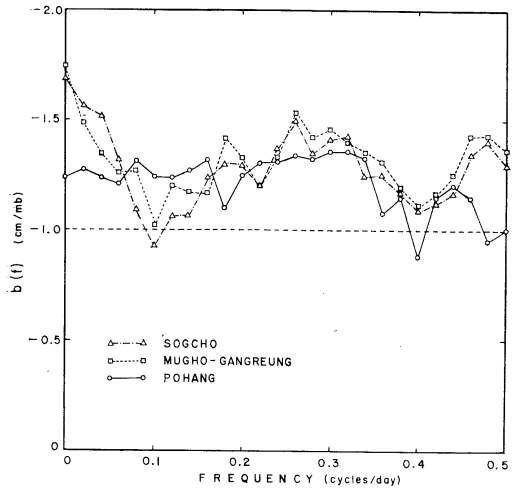

Fig. 11. Barometric factor versus frequency for Sogcho, Mugho-Gangreung, and Pohang in the summer season.

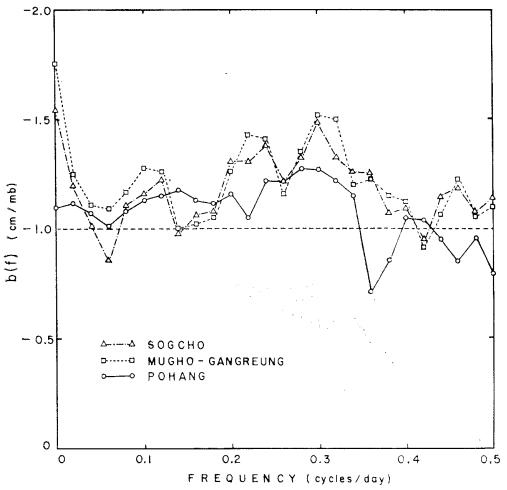

Fig. 12. Barometric factor versus frequency for Sogcho, Mugho-Gangreung, and Pohang in the winter season.

was computed. The computed barometric factors for all the stations both for the summer and the winter records are shown in Figs. 11 and 12. Generally, the barometric factor is greater than 1.01 cm/mb, and also it varies with the frequency f. The higher values of the barometric factor appear in the range of 0.22–0.32 cpd for all the stations for the summer records. In the case of winter records, they appear at two subranges, 0.22–0.24 cpd and 0.30–0.32 cpd, for Sogcho and Mugho, in 0.28–0.30 cpd for Pohang.

The weighted barometric factor was obtained by taking a weighted average of $b(f)$ over frequency. Table 1 shows the weighted barometric factor. Our computed barometric factors indicate that the isostatic hypothesis does not hold for all frequencies and that an abnormal phenomenon exists.

4) Cross Correlation

The cross correlations between the adjusted sea level at different stations for each season are shown in Figs. 13 and 14. In case of the

Table 1. The weighted barometer factor.

Stations	Summer (cm/mb)	Winter (cm/mb)
Sogcho	1.28±0.18	1.20±0.16
Mugho-Gangreung	1.27±0.18	1.23±0.17
Pohang	1.20±0.12	1.11±0.12

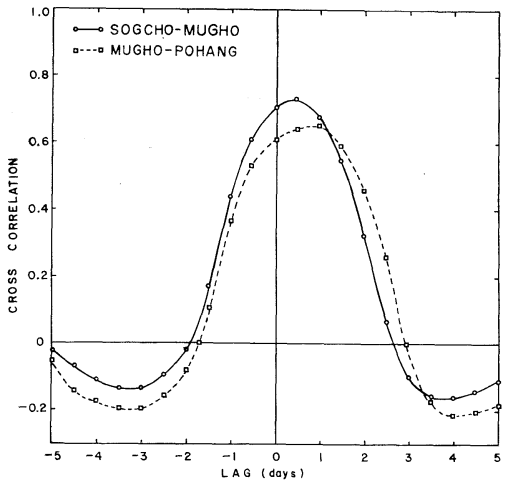

Fig. 13. Lagged cross correlation between the adjusted sea levels in the summer season.

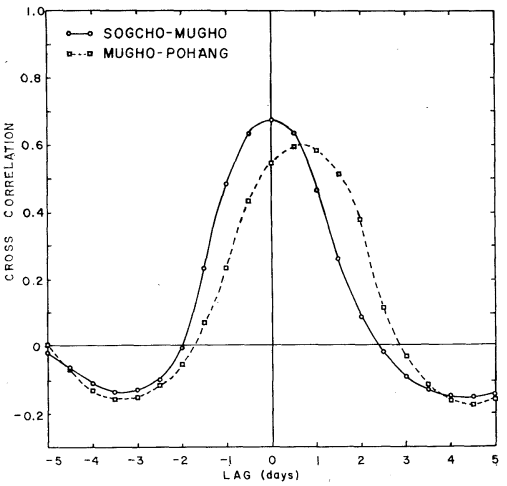

Fig. 14. Lagged cross correlation between the adjusted sea levels in the winter season.

summer, the maximum correlation between Sogcho and Mugho appears at time lag of half day, and one day for Mugho and Pohang, while in the winter it is located near zero time lag. The time lag at the maximum correlation represents a weighted mean of the phases at

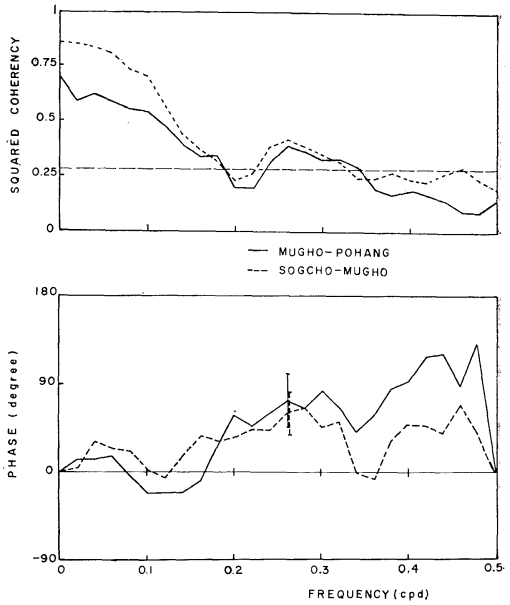

Fig. 15. Squared coherency and phase spectra in the summer season.

different frequencies. According to our cross correlation analysis, it implies that a certain phenomenon such as a southward travelling signal existed. The direction of propagation in this phenomenon is consistent with that of the continental shelf waves.

5) Cross-spectrum

The squared coherency and the phase spectrum obtained from the cross spectra of the sea levels give the correlation and the time displacement of one record with respect to the other as a function of frequency, using the adjusted sea level data. Computations were made for Sogcho versus Mugho and for Mugho versus Pohang, for the summer season. Figure 15 shows the squared coherency and the phase spectrum. As a test of statistical significance, the 95% confidence levels for the squared coherency and for the phase spectrum are indicated in the figure.

The squared coherency for the Sogcho versus Mugho is greater than the 95% confidence level at 0–0.18 cpd and 0.24–0.32 cpd. For the Mugho versus Pohang, the squared coherency is significant at the 95% confidence level at frequencies 0–0.18 cpd and 0.24–0.34 cpd. Except 0–0.18 cpd, the maximum of the squared coherency occurs at 0.26 cpd for the both station pairs. The phase

differences of the frequency at the squared coherency maximum between the station pairs, the Sogcho versus Mugho and the Mugho versus Pohang, are 60° and 70° respectively. The phase differences are interpreted as the lag time, because the observed phase shift seems to be caused by the propagation of the signal from north to south, which is in the same direction as that of the continental shelf waves at northern hemisphere. This result is also consistent with the interpretation of the cross correlation analysis.

The observed phase velocity at any given frequency f can be obtained from the phase shift by the following expression;

$$c=L/\tau(f)=2\pi fL/\theta(f),$$

where $\tau(f)$ is the time lag, $\theta(f)$ is the phase shift and L is the distance between two stations. Our computed phase speed between Sogcho and Mugho, where L is 90 km, is 140 km/day and for Mugho and Pohang, where L is 190 km, is 250 km/day at frequency of 0.26 cpd.

4. Theoretical considerations

Some of theories on continental shelf waves were analyzed in order to find out a theory, which could properly explain our findings than others along with the boundary conditions of our bottom topography.

1) Robinson and Mysak's Shelf Wave Theory

According to ROBINSON (1964), the sea level would be the result of the isostatic response plus the elevations due to travelling waves initiated by the pressure variations or wind stress correlated with pressure. The sea level would be then regarded as containing the sum of the isostatic responses to the atmospheric pressure and the elevation due to the continental shelf waves. So, the continental shelf waves could either increase or decrease according to the apparent barometric factor.

In general, the continental shelf waves in mid-latitude have long wavelengths ($\lambda \gg l$, λ: wavelength, l: shelf width), low frequencies ($w \ll f$, w: wave frequency, f: inertial frequency), and small amplitude (a few centimeters).

Robinson's model implies that it could have infinite number of modes, i.e., the first mode has an antinode at the coast, decaying exponentially seawards from the shelf edge, while higher modes have nodes and antinodes in shelf region. And also the shelf waves travel in one direction only and they are nondispersive. ROBINSON (1964) has proposed that the phase speed, $C=\omega/\kappa$, is

$$C=-4fl/\gamma^2_{0j},$$

where f is the Coriolis parameter, l is the shelf width and γ_{0j} ($j=1, 2, \ldots$) is defined as the roots of the zeroth order Bessel function of the first kind. For the fundamental mode, $C=-fl/1.44$.

To apply the Robinson's model on this analysis, the 200 m contour line was taken to be the edge of the continental shelf (Fig. 1). The averaged shelf width between Sogcho and Mugho is about 10 km, and that between Mugho and Pohang is about 25 km. The distance from Sogcho to Mugho is 90 km, and the distance between Mugho and Pohang is 190 km. The Coriolis parameters were taken from the mean latitude between the two pairs of stations. The Robinson's model predicts that the continental shelf waves have a phase speed of 50 km/day between Sogcho and Mugho, and 130 km/day between Mugho and Pohang. These predicted values are much lower than our observed phase speeds.

MYSAK (1967) presented a more comprehensive model which include effects of a linear slope at the edge of the shelf, a mean current and a deep sea stratification. It was found that the predicted phase speeds of the Mysak's model are about twice as that of the Robinson's model.

It should be noted that the both models are based on the assumption, i.e. the bottom profile has a linear slope at the shelf, and it drops off towards a flat deep sea region. But our bottom topography looks more like an exponential depth profile.

2) Exponential Depth Profile Model

The fluid is assumed to be inviscid, incompressible and homogeneous. A right-handed Cartesian coordinate system (x, y, z) is introduced, with the positive z-axis vertically upwards. Let $\zeta(x, y, z)$ and $h(x, y)$ denote the elevation of the free surface above the equilibrium level and the depth respectively. Then, a set of the linearized equations of motion in the case of uniformly rotating shallow water is given by

$$\frac{\partial u}{\partial t}-fv=-g\frac{\partial \zeta}{\partial x} \qquad (1)$$

$$\frac{\partial v}{\partial t}+fu=-g\frac{\partial \zeta}{\partial y} \qquad (2)$$

with the equation of continuity,

$$\frac{\partial (hu)}{\partial x}+\frac{\partial (hv)}{\partial y}+\frac{\partial \zeta}{\partial t}=0, \qquad (3)$$

where u and v are components of the velocity in the x, y directions, g is the acceleration of gravity and f is the Coriolis parameter.

To perform the scale analyses of the topography and the motion, two assumptions are introduced: 1) f-plane approximation in which the slope of the bottom topography is sufficiently large so as to dominate the β-effect, i.e. $|\nabla h| > h/R_e \tan\theta$. For our study region, the depth $h \simeq 0(2\times10^2-10^3\,\mathrm{m})$, $R_e \tan\theta \simeq 0(6\times10^6\,\mathrm{m})$ (R_e: radius of Earth, θ; latitude), and $l \simeq 0(10^4\,\mathrm{m})$ (l: shelf width). Hence, $|\nabla h| \simeq 0(10^{-2})$, $h/R_e \tan\theta \simeq 0(10^{-4})$. These values satisfy the condition of f-plane approximation. 2) Rigid-lid approximation, in which $\varepsilon \ll 1$. The parameter $\varepsilon = f^2 l^2/gh$ is square of the ratio of the geometric length scale (l) to the Rossby deformation radius $R=(gh)^{1/2}/f$. If $\varepsilon=(l/R)^2 \ll 1$, from the point of view of the vorticity balance, the free surface appears to be a rigid (PEDLOSKY, 1979). For the studied region, ε is smaller than 2×10^{-3}, which certainly satisfies $\varepsilon \ll 1$. The assumption

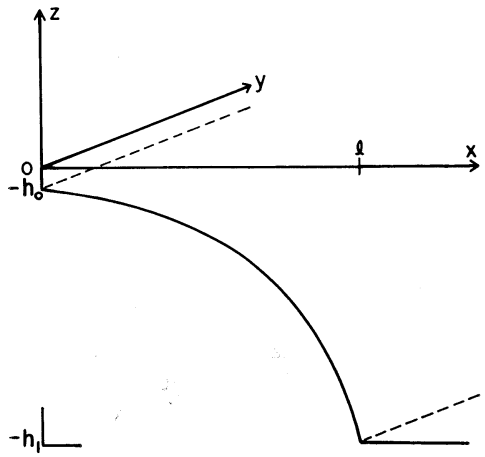

Fig. 16. Shelf profile model.

$\varepsilon=0$ implies the motion is horizontally non-divergent. Consequently, in this case the vertical displacement can be neglected in the equation of continuity, so that the equation becomes

$$\frac{\partial (hu)}{\partial x}+\frac{\partial (hv)}{\partial y}=0. \qquad (4)$$

This allows us to use a mass-transport stream function ϕ

$$hv=\frac{\partial \phi}{\partial x},\quad hu=-\frac{\partial \phi}{\partial y}. \qquad (5)$$

Subtracting equation (1) from equation (2) after partially differentiating them with respect to x, y respectively and then, using equations (4) and (5), one finds the vorticity equation

$$\frac{\partial}{\partial t}\left[\frac{\partial}{\partial y}\left(\frac{1}{h}\frac{\partial \phi}{\partial y}\right)+\frac{\partial}{\partial x}\left(\frac{1}{h}\frac{\partial \phi}{\partial x}\right)\right] +f\left[\frac{\partial}{\partial y}\left(\frac{1}{h}\frac{\partial \phi}{\partial x}\right)-\frac{\partial}{\partial x}\left(\frac{1}{h}\frac{\partial \phi}{\partial y}\right)\right]=0. \qquad (6)$$

Let assume that the depth profile has the form of

$$h(x)=\begin{cases} h_0 e^{-bx}, & 0\le x<l \\ h_1, & l<x \end{cases} \qquad (7)$$

where $h_1=h_0 e^{-lb}$ so that h is continuous at $x=l$. Appropriate values for the shelf near Mugho are found to be $h_0=10$ m, $h_1 \sim 1000$ m, $l \sim 6\times10^4$m and $bl \sim 4.6$, respectively. Figure 16 shows the resulting model of the shelf profile.

For the waves travelling parallel to the coast, we assume that

$$\phi(x,y,t)=\Phi(x)\, e^{i(ky-\omega t)}. \qquad (8)$$

In the shelf region, equation (6) becomes, after some manipulation,

$$\frac{d^2\Phi}{dx^2}-b\frac{d\Phi}{dx}-\left(\frac{fbk}{\omega}+k^2\right)\Phi=0 \qquad (9)$$

and in the deep ocean ($b=0$),

$$\frac{d^2\Phi}{dx^2}-k^2\Phi=0. \qquad (10)$$

For trapped waves, the boundary condition is given by $hu=0$ for all y at the coast, hence

$\Phi(0)=0$. In the deep ocean, the amplitude of the trapped waves decays, hence $\Phi\to 0$ as $x\to\infty$. The solutions of equations (9) and (10) are

$$\Phi_s = Ae^{\frac{b}{2}x}\sin mx\,, \tag{11}$$

$$\Phi_0 = Be^{-|k|x}\,, \tag{12}$$

where A and B are arbitrary constants and m is determined from

$$m^2+k^2+\left(\frac{b}{2}\right)^2+\frac{fbk}{\omega}=0\,. \tag{13}$$

At $x=l$, the elevation of sea level ζ and the normal transport hu are continuous, so

$$\Phi_s(l)=\Phi_0(l)$$
$$\left.\frac{d\Phi_s}{dx}\right|_{x=l}=\left.\frac{d\Phi_0}{dx}\right|_{x=l}\,. \tag{14}$$

From the equations (11), (12) and (14), we obtain

$$\tan m=-\frac{m}{\frac{b}{2}+|k|}\,. \tag{15}$$

Equations (13) and (15) give the theoretical properties of the shelf waves. Equation (13) can be rewritten in the form of

$$\left(\frac{\omega}{k}\right)_i=-\frac{bf}{m_i^2+k^2+(b/2)^2}\,, \tag{16}$$

where subscript i denotes the mode number of the waves and m_i is the ith solution of equation (15). In the northern hemisphere, $f>0$, so $(\omega/k)_i$ is negative and waves propagate with the phase velocity in the negative y-direction only. But the group velocity has opposite sign for the wave number k. In the case of very long waves, $(k\to 0)$,

$$\left(\frac{\omega}{k}\right)_i=-\frac{bf}{m_i^2(0)+(b/2)^2}\,. \tag{17}$$

This indicates that ω_i is approximately linear in k. Consequently, the phase and group velocities are equal and nearly constant.

For near Mugho, bl and $m_1(0)$ are found to be $bl=4.6$, and $m_1(0)=2.3$, being computed by the method of BUCHWALD and ADAMS (1968) using our local value of $f=8.88\times10^{-5}$ rad/sec. Hence the southward velocity of long shelf waves is computed as 230 cm/sec or 200 km/day, which agree with our observed values, 140 km/day–250 km/day.

5. Discussion of results

The spectral analysis of sea level and atmospheric pressure shows that the adjusted sea levels have energy peaks in the frequency band 0–0.5 cpd. This result indicates that the isostatic hypothesis does not account for sea level variations. Another significant peak which appeared near 0.26 cpd in summer records for all stations, indicates the existence of a phenomenon with period of 0.26 cpd. The barometric factor in the region having significant spectral peaks shows an apparent increase in the response of sea level to atmospheric pressure. It is difficult to explain higher peaks occurred at zero frequency. However, they might be associated with monthly or annual sea level changes.

The cross correlations between the adjusted sea level at different stations, the squared coherency, and phase spectra for our summer records indicate that a southward travelling signal exists, which is consistent with the propagation direction of the continental shelf waves. According to LE BLOND and MYSAK (1978) and PEDLOSKY (1979), there is an exact dynamical equivalence between the variation of the Coriolis parameter with latitude, and variations of topography in the presence of constant f. Topographic Rossby waves occur when topographic β-effect is greater than planetary β-effect. In the continental shelf region of the eastern coast of Korea, the slope of bottom topography, $0(10^{-3}$–$10^{-2})$, is greater than that of equivalent topographic β-effect, $0(10^{-4})$. Therefore, the topographic β-effect dominates the planetary β-effect at the region we examined and the topographic Rossby waves, namely continental shelf waves in this case, can occur at the continental margin. The travelling signal has properties that $f\gg\omega$ and $\lambda\gg l$ ($\omega=0(10^{-6})$, $f=0(10^{-4})$, $l=0(10^{6})$, and $\lambda=0(10^{7}$–$10^{8})$), which satisfy the characteristics of continental shelf waves. Hence, the travelling signal may be interpreted as continental shelf waves.

Continental shelf waves are essentially caused by changes in potential vorticity when fluid

elements are displaced up or down the slope by some driving force. ADAMS and BUCHWALD (1969), and GILL and SCHUMANN (1974) insist that as one of the characteristics of the shelf waves the vortex stretches over the shelf due to an oscillating vorticies. In the present study, we found a similar phenomenon in the relationship between the spectra of sea level and those of atmospheric pressure, suggesting that the travelling disturbance might have been generated by the atmospheric pressure fluctuations. However, it could be possible that the wind stress also acts on shelf waves as a driving force, in view of the fact that pressure fluctuations tend to be highly correlated to the changes in the wind stress. At any rate the driving mechanism of the shelf waves is worthy of further investigations.

Our observed phase speed appears to be in better agreement with the theory of nondivergent shelf waves. Based on our findings, it may be concluded that stratifications, longshore currents (branches of the Tsushima current), and topographic irregularities all seem to be responsible for the generation of the continental shelf waves, at least in the regions we investigated.

6. Conclusions

1. The result of the autospectral analysis shows that the adjusted sea levels have energy peaks near 0.26 cpd for all stations during the summer. This result indicates that the isostatic hypothesis does not account for sea level variations. Any statistically significant periodicities don't exist for the adjusted sea level data in winter.

2. The barometric factor indicates that the response of sea level to atmospheric pressure fluctuations is non-barometric. The weighted barometric factor shows seasonal variation.

3. The cross correlations between the adjusted sea level at different stations, the squared coherency, and phase spectra for summer records indicate existence of a southward travelling signal.

4. The predicted phase speeds of the nondivergent shelf wave theory, based on exponential depth profile model, well agree with the observed values. The phenomenon of wavelike motion, which we found through this investigation, might be interpreted as a continental shelf wave.

5. The driving mechanism of the shelf waves is worthy of further investigations. And also the detailed investigations on the effects of stratifications, current, and topography will be left future.

References

ADAMS, J. K. and V. T. BUCHWALD (1969): The generation of continental shelf waves. J. Fluid Mech., **35**, 815-826.

BROOKS, D. A. and C. N. K. MOOERS (1977): Wind-forced continental shelf waves in the Florida Current. J. Geophys. Res., **82**, 2569-2576.

BUCHWALD, V. T. and J. K. ADAMS (1968): The generation of continental shelf waves. Proc. Roy. Soc., A, **305**, 235-250.

CARTWRIGHT, D. E. (1969): Extraordinary tidal currents near St. Kilda. Nature, **223**, 928-932.

CHUNG, J. Y. (1979): Turbulence spectra in a well-mixed estuary. Ph. D. dist. 233 pp.

CSANADY, G. T. (1976): Topographic waves in Lake Ontario. J. Phys. Oceanogr., **6**, 93-103.

CUTCHIN, D. L. and R. L. SMITH (1973): Continental shelf waves: Low frequency variations in sea level and currents over the Oregon continental shelf. J. Phys. Oceanogr., **3**, 73-82.

GILL, A. E. and E. H. SCHUMANN (1974): The generation of long shelf waves by the wind. J. Phys. Oceanogr., **4**, 83-90.

GROSCH, C. E. and J. Y. CHUNG (1981): NEWFFT—Two dimensional package program for Old Dominion University computer center.

HAMON, B. V. (1962): The spectrums of mean sea level at Sydney, Coff's Harbour, and Lord Howe Island. J. Geophys. Res., **67**, 5147-5155. (correction, 1963, J. Geophys. Res., **68**, 4635)

HAMON, B. V. (1966): Continental shelf waves and the effects of atmospheric pressure and wind stress on sea level. J. Geophys. Res., **71**, 2883-2893.

HAMON, B. V. (1976): Generation of shelf waves on the east Australian coast by wind stress. Mém. Soc. R. Sci. Liège. 6e sér., **10**, 359-367.

HAMON, B. V. and E. J. HANNAN (1963): Estimating relations between time series. J. Geophys. Res., **68**, 6033-6041.

HOUGHTON, R. W. (1979): Characteristics of the fortnightly shelf wave along the Ghana coast. J. Geophys. Res., **84**, 6355-6361.

ISOZAKI, I. (1969): An investigation on the variations of sea level due to meteorological dis-

turbances on the coast of Japanese island (III). J. Oceanogr. Soc. Japan, **25**, 91-102.

JENKINS, G. M. and D. G. WATTS (1968): Spectral Analysis and its Applications. Holden-day, San Francisco. 525 pp.

LE BLOND, P. H. and L. A. MYSAK (1978): Waves in the Ocean. Elsevier, Amsterdam. 602 pp.

LIE, H. J. (1979): Effects of atmospheric pressure and wind stress on daily mean sea level in the Bay of Biscay. Analysis of continental shelf waves. J. Oceanogr. Soc. Korea, **14**, 45-53.

MOOERS, C. N. K. and R. L. SMITH (1968): Continental shelf waves off Oregon. J. Geophys. Res., **73**, 549-557.

MYSAK, L. A. (1967): On the theory of continental shelf waves. J. Mar. Res., **25**, 205-227.

MYSAK, L. A. and B. V. HAMON (1969): Low-frequency sea level behavior and continental shelf waves off North Carolina. J. Geophys. Res., **74**, 1397-1405.

PEDLOSKY, J. (1979): Geophysical Fluid Dynamics. Springer-Verlag. New York. 624 pp.

ROBINSON, A. R. (1964): Continental shelf waves and the response of sea level to weather systems. J. Geophys. Res., **69**, 367-368.

SCHOTT, F. and W. DÜING (1976): Continental shelf waves in the Florida Straits. J. Phys. Oceanogr., **6**, 451-460.

SHOJI, D. (1961): On the variations of the daily mean sea levels along the Japanese Island. J. Oceanogr. Soc. Japan, **17**, 142-152.

韓国東方海域の大陸棚波

Jae Hak LEE, Jong Yul CHUNG

要旨: 大気圧が水位の12時間平均に与える影響を，韓国東方の3点でスペクトル解析を行って調べた。0～0.5 cpd という周波数帯では水位は気圧変動に追随しない，計算された位相差および異なる観測点間の水位変化のずれから，夏にだけ 0.24～0.26 cpd の北から南に向かう波動があることがわかる。この海域の深さの分布（指数関数）を使い，非発散陸棚波理論によって位相速度を計算すると，計算結果は観測結果によくあう。したがって，ここで扱った水位変動は陸棚波であると結論されよう。

La mer 20: 181-189, 1982
Société franco-japonaise d'océanographie, Tokyo

Dynamic Response of a Savonius-like Rotor to Unsteady Flows*

Hideki NAGASHIMA** and Moriyoshi OKAZAKI**

Abstract: Response of a rotor type current meter to a stepwise or a sinusoidal change of current speed is studied by a simple two rotor-vane model. The characteristics of the rotor are described by two nondimensional parameters; one is the ratio γ of the normal drag coefficients of both sides of a rotor vane, and the other is the nondimensional moment of inertia. The model is applied to a unidirectional flow, whose magnitude fluctuates sinusoidally, and the positive errors in current measurements are estimated and are well in agreement with those in laboratory experiments by KARWEIT (1974). The response of the rotor to a pure oscillatory flow is also examined by the model and the results are favourably compared with those of laboratory experiment for the Savonius-like rotor. The results shows that the "apparent" current is erroneously recorded by the rotor type current meter. The magnitude of the "apparent" current is 80~90 % of the maximum velocity of the oscillatory current.

1. Introduction

The rotor type current meter is frequently used as a current sensing device in ocean research. For steady flows, the averaged rotational frequency of the rotor is almost linearly related to the speed of the surrounding fluid. However, the real flows are at least unsteady and fluctuated, especially much in the surface layer due to wind waves, turbulence and so on. It is well known that such unsteadiness of the flow produces errors in current observation. SAUNDERS (1976) reports that the Aanderaa current meter with a savonius-like rotor gives mean currents two or three times as strong as those by VACM (vector averaged current meter) in the JASIN '72 experiment. A systematic current meter intercomparison experiment (CMICE 76) is conducted by BEARDSLEY *et al.* (1977) and shows that the Aanderaa current meter overestimates current speeds. The cause of the overestimation is considered to be due to the equal sensitivity of the rotor for any current directions, the fluctuation of mooring systems and so on, in connection with sampling intervals.

The estimation of the error for the Savonius rotor is already reported by KARWEIT (1974) based on the laboratory experiment for sinusoidally fluctuating unidirectional flows. It is found that the error E is apparently positive and any unsteadiness in the flow produces a systematic bias in readings.

Dynamical considerations for meteorological anemometers, such as cup anemometers and rotation vane anemometers are investigated by many workers (MACCREADY, 1966; RAMACHANDRAN, 1969; KONDO *et al.*, 1971; KANANOV and YAGLOM 1976). They solve similar dynamical equations and evaluate the so-called U-error for rotation anemometers. These works are for the case in which fluctuations are much smaller than mean wind speeds. In the ocean, however, fluctuations are rather large and sometimes an oscillatory current with a zero mean velocity is found such as orbital motions due to wind waves. Therefore, it is necessary to investigate a response of a rotor under such conditions.

The equation of rotor rotation is written by

$$I\frac{d\omega}{dt}=N, \qquad (1)$$

where ω, I and N are an angular frequency of the rotor, its moment of inertia and the torque. N is mainly due to the hydrodynamical torque which depends on the positions of rotation vanes

* Received December 25, 1981
** Institute of Physical and Chemical Research, Hirosawa, Wakoh-shi, Saitama-ken, 351 Japan

in relation to the direction of the current. It is very difficult to evaluate the torque exactly because of the complexity of the flow around the rotor.

In this paper a simple 2-vane model is proposed and the response of the rotor is investigated by solving the equation of the rotor rotation. This model is applied to a unidirectional flow, the magnitude of which fluctuates sinusoidally. The results are favourably compared with the Karweit's experimental data. Numerical calculations are extended for the case of a sinusoidal fluctuation with a zero mean velocity and compared with the results of laboratory experiments.

2. Equation of rotor rotation

A rotor type current meter has several rotation vanes. As shown in Fig. 1, the hydrodynamical torque N_i acting on the i-th rotation vane at the angle θ may be written by

$$N_i=\frac{1}{2}\rho s C_D(\alpha)U_e^2(\theta)r_e + \rho s d r_e C_M(\alpha)\frac{dU_e}{dt}, \qquad (2)$$

where ρ is the water density, $C_D(\alpha)$ the normal drag coefficient for a rotation vane at angle α, α the angle between the tangential direction of rotation and the direction of a relative velocity $\vec{U}_e$ of the vane, s the area of the vane, d the thickness, and r_e the effective distance between the axis of rotation and the vane (FUJINAWA, 1977). The second term in (2) is the torque due to the virtual mass, where $C_M(\alpha)$ is the added mass coefficient. $U_e(\theta)\,(=|U_e|)$ is connected with the current velocity U and the angular frequency ω of the counterclockwise rotation by the following relation:

$$U_e=(U^2+r_e^2\omega^2-2Ur_e\omega\cos\theta)^{1/2}, \qquad (3)$$

and

$$\alpha=\theta+\phi, \qquad (4)$$

$$\phi=\sin^{-1}\left(\frac{r_e\omega}{U_e}\sin\theta\right). \qquad (5)$$

The evaluation of the torque N_i is difficult because of unknown parameters, $C_D(\alpha)$, $C_M(\alpha)$ and r_e. Even if these values are given, it is very complicated to sum up the torque N_i for all vanes and to solve the equation (1). Then,

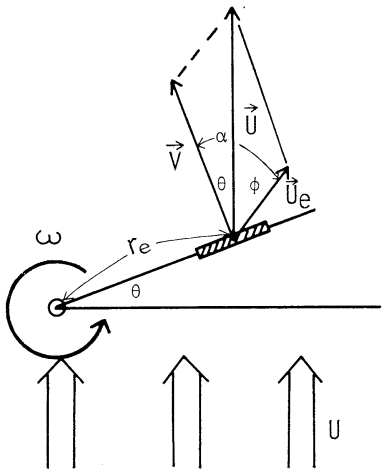

Fig. 1. Schematic view of rotation of a vane. Water flows upward with its speed of U, a vane rotates counterclockwise in this plane with the angle θ. Hydrodynamical torque is supposed to act on the point, whose distance from the axis of rotation is denoted by r_e. $\vec{V}$ and $\vec{U}_e$ denote tangential velocity of the point and the fluid velocity relative to it, respectively, and α the angle between these two vectors, ϕ the angle between current direction and the direction of the vector $\vec{U}_e$.

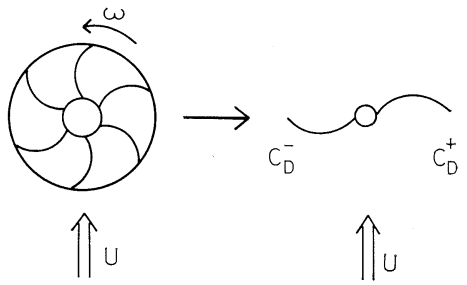

Fig. 2. Schematic view of the two rotor-vane model. Hydrodynamical torques acting on a rotor shown in left-hand side are simplified to be torques acting on virtual two vanes, one of which has a position with its concave side against flow direction, and the other with its convex side. Normal drag coefficient of each side is denoted by C_D^+ and C_D^-, respectively.

we simplify the torque ΣN_i by considering two virtual rotation vanes as shown in Fig. 2 instead of taking real all vanes into consideration. One has the position of $\theta=0$ with the drag coefficient C_D^+, the other $\theta=\pi$ with the coefficient C_D^-, where C_D^+ is greater than C_D^-. As the second term of (2) is negligibly small (detailed order estimation is given in § 4), the torque N in (1) acting on the two vanes is given by

$$N\begin{cases}=\dfrac{1}{2}\rho s r_e[C_D^+(U_e^+)^2-C_D^-(U_e^-)^2], & (U_e^+\geq 0)\\ =-\dfrac{1}{2}\rho s r_e C_D^-[(U_e^+)^2+(U_e^-)^2], & (U_e^+<0),\end{cases} \quad (6)$$

where $U_e^+=U-r_e\omega$, $U_e^-=U+r_e\omega$. This is a simple expression of the torque which rotates a rotor. The basic characteristics of the torque, however, seem to be well modeled. Now, let us consider that the current U changes sinusoidally with its amplitude $u_{\max}$ around the averaged velocity U_0, hence, U is given by

$$U=U_0+u_{\max}\sin\beta t\,, \quad (7)$$

where β denotes the angular frequency of the sinusoidal fluctuation of the current.

With the following characteristic scales

$$\omega_0=\frac{U_0}{r_e},\ \omega_1=\frac{u_{\max}}{r_e}\ \text{and}\ \beta,$$

the nondimensional form of (1) is derived:

$$A\frac{dY}{dt}=p(1+f\sin t'-Y)^2-\gamma(1+f\sin t'-Y)^2, \quad (8)$$

where

$$Y=\omega/\omega_0,\ \gamma=C_D^-/C_D^+,$$
$$f=\omega_1/\omega_0(=u_{\max}/U_0),\ t'=\beta t\,,$$
$$A=2I\beta/\rho s r_e^3 C_D^+\omega_0,$$
$$p\begin{cases}=1;\ (1+f\sin t'-Y\geq 0)\\ =-\gamma:\ (1+f\sin t'-Y<0)\end{cases}$$

and the prime in t' is hereafter neglected for simplicity.

3. Results

Constant flow: In the case of a constant flow U_0, the equation (8) becomes

$$p(1-Y)^2=\gamma(1+Y)^2. \quad (9)$$

Since the value of p in this case is 1, the solution of the equation (9) is given by

$$Y=\frac{1-\sqrt{\gamma}}{1+\sqrt{\gamma}}\equiv g(\gamma)\,. \quad (10)$$

The solution (10) can be expressed by

$$r_e\omega_s=U_0 g(\gamma)\,, \quad (11)$$

where ω_s denotes the angular frequency of the rotor in the steady state.

Response to abrupt changes of flow: Next we calculate the equation (8) for the stepwise change of current speed as follows:

(a) $U=0$, $t\leqq 0$ and $U=U_0$, $t>0$ (acceleration), (12)

and

(b) $U=U_0$, $t\leqq 0$ and $U=0$, $t>0$ (deceleration). (13)

In these two cases the equation (8) becomes

$$A\frac{dY}{dt}=p(1-Y)^2-\gamma(1+Y)^2, \quad (14)$$

where β in A is replaced by ω_0. In the case (a), since $U_e^+(=U-r_e\omega)$ in (6) has a positive value for $t>0$, the torque N is given by $1/2\cdot\rho s r_e[C_D^+(U_e^+)^2-C_D^-(U_e^-)^2]$. Thus, we can put $p=1$ in (14) and the solution for $t>0$ becomes

$$Y=\frac{g(\gamma)(1-\exp(4\sqrt{\gamma}/A\cdot t))}{g^2(\gamma)-\exp(4\sqrt{\gamma}/A\cdot t)}\,, \quad (15)$$

where $Y=0$ (at $t=0$) is used as an initial condition. The non-dimensional time constant τ_A can be expressed by

$$\tau_A=\frac{A}{4\sqrt{\gamma}}\,; \quad (16)$$

On the other hand, in the case (b), since U_e^+ in (6) has a negative value for $t>0$, the torque N is given by $-1/2\cdot\rho s r_e C_D^-[(U_e^+)^2+(U_e^-)^2]$. Moreover, as the constant flow is absent for positive t, the relation $(U_e^-)^2=(U_e^+)^2=(r_e\omega)^2$ is derived. Thus, the right-hand side of the equation (14) is reduced to $-2\gamma Y^2$. The solu-

tion for $t>0$ becomes

$$\frac{1}{Y}=\frac{1}{g(\gamma)}+\frac{2\gamma}{A}t, \qquad (17)$$

where the relation (10) is used at $t=0$. The solution (17) is rewritten by

$$Y=g(\gamma)\,(1+t/\tau_D)^{-1}, \qquad (18)$$

where $\tau_D=A/2\gamma g(\gamma)$. Inspecting (15), we see that Y shows exponential growth, but from (18) Y does not decay exponentially. Furthermore, the ratio, denoted by τ_{AD}, of the above two time constants is given by

$$\tau_{AD}\equiv\tau_D/\tau_A=2\gamma^{-1/2}\cdot g(\gamma)^{-1}$$
$$=2(1+\sqrt{\gamma})(\sqrt{\gamma}-\gamma)^{-1}. \qquad (19)$$

Note that τ_{AD} is a function of γ only and does not depend on any other parameters. GAUL *et al.* (1963) investigated dynamical properties of the Savonius rotor, e.g., response of the rotor to abrupt change of a flow speed between zero and non-zero costants. Their results shown in Fig. 3 indicate that the rotor decays towards zero much more slowly than it accelerates and the decay rate is a function of step change magnitude. In the present model, the dimensional time constant τ_D^* is given by

$$\tau_D^*=\tau_D/\omega_0=\frac{A}{2\gamma g(\gamma)\omega_0}$$
$$=\frac{I}{\gamma g(\gamma)\rho s r_e^2 C_D^+ U_0}\equiv\frac{L}{U_0}. \qquad (20)$$

As L is almost independent on fluid speed U_0, τ_D^* is inversely proportional to U_0. The difference of the decay rates in the all cases is much conspicuous just after the abrupt change of a flow speed occurs. This might be caused by the wake induced in the wave tank as they described. So, it is difficult to estimate the value of τ_D^*, though the dimensional time constant τ_A^* is easily estimated. If we estimate τ_D^* from the decay curve for large t, τ_{AD} is calculated to be 15.2 approximately. The corresponding value

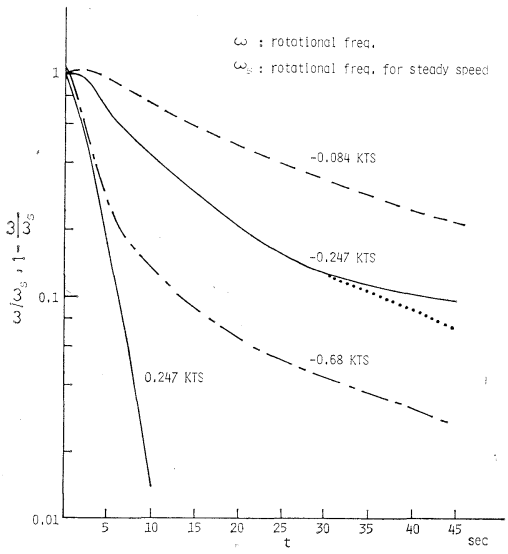

Fig. 3. Rotor response to abrupt change between zero and steady speed. This figure is quoted from GAUL *et al.* (1963) and is rewritten in a semi-logarithmic space. A positive sign denotes change from zero to steady speed; negative vice versa. Abscissa represents the time after the step change of towed speed. Ordinate represents ω/ω_s for negative change, and $1-\omega/\omega_s$ for a positive change. The time constant τ_D^* is estimated from the dotted line.

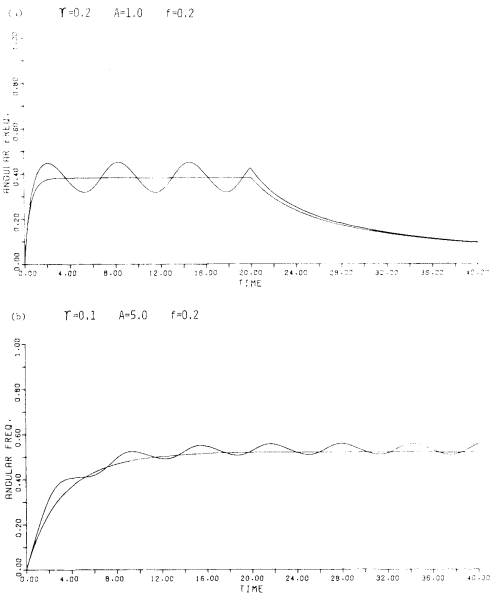

Fig. 4. Time history of normalized rotational frequency for a unidirectional flow, the magnitude of which fluctuates sinusoidally ($f=0.2$). For comparison, a case of nonfluctuation ($f=0$) is also shown. (a) for the case of $\gamma=0.2$ and $A=1.0$. (b) for the case of $\gamma=0.1$ and $A=5.0$.

of γ is derived from (19) to be 0.038 approximately.

Response to an oscillatory flow

Case a ($U_0 > u_{max}$): As it is difficult to obtain a general solution of the equation (8) analytically, (8) is reduced to a difference equation. Forward difference scheme is adopted and (8) is integrated numerically with the nondimensional time interval of 0.01. This means that the equation is integrated about 600 steps within an oscillation of current. Typical two examples are shown in Fig. 4. One is the case in which the values of γ and A are 0.2 and 1.0, respectively. The time history of the normalized rotational frequency Y for $f=0.2$ is compared with that for the constant flow ($f=0$). No significant difference is found between the value for $f=0$ and the averaged value $\overline{Y}$ for the oscillatory current. Each value is 0.382 approximately and is in good agreement with that of the analytical solution (10) for a steady flow. When the flows are stopped at $t=20$, Y decreases gradually. The time constants of deceleration are larger than those of acceleration as the equation (20) indicates. The other example illustrated in Fig. 4b is the case in which the values of γ and A are 0.1 and 5.0, respectively. The averaged rotational frequency for the oscillatory flow is clearly larger than that for the constant flow. This evidence suggests that unsteadiness of the flow sometimes produces positive errors in current observation.

The normalized error E is defined by

$$E \equiv \frac{\bar{Y} - Y_0}{Y_0}, \qquad (21)$$

where Y_0 is the solution for constant flow, and $\bar{Y}$ is for the flow oscillating around the same constant flow and is estimated from the average of the last ten of 100 oscillations. As is readily seen from the equation (8), E is a function of γ, A and f. Three curves in Fig. 5 show the estimated error E as a function of f for three different values of γ with $A=5.0$. The results indicate that the smaller the value of γ is and the larger the amplitude of oscillation is, the larger the error E is. The dependence of E on A for a constant value of γ ($=0.04$) is shown in Fig. 6. This figure indicates that E increases with A and becomes almost constant for large A. From (16), the dimensional time constant τ_A^* is given by

$$\tau_A^* = \frac{\tau_A}{\beta} = \frac{T}{2\pi}\tau_A = \frac{T}{2\pi} \cdot \frac{A}{4\sqrt{\gamma}}. \qquad (22)$$

Hence, the ratio τ_A^*/T is $A/8\pi\sqrt{\gamma}$. When $\gamma=0.04$, the relation $\tau_A^*/T=1$ corresponds approximately to $A=5.0$. Thus, it could be concluded that if a period of oscillation is shorter than or equal to the response time of the rotor, E does not depend on A (or τ_A^*/T), on the other hand, if it becomes much longer, E decreases and tends to be zero.

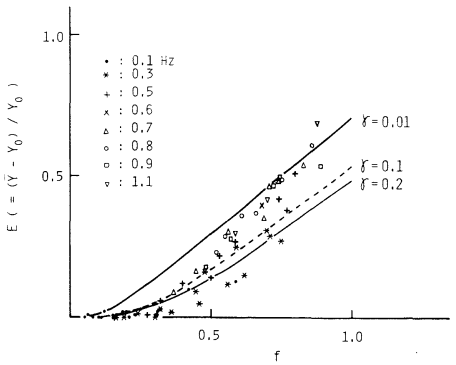

Fig. 5. Normalized error E in measurement of unidirectional current. Abscissa represents the magnitude of fluctuation of current relative to the constant flow. Three lines indicate for various values of γ. Here, the value of A is fixed to be 5.0. Symbols indicate experimental values quoted from KARWEIT (1974).

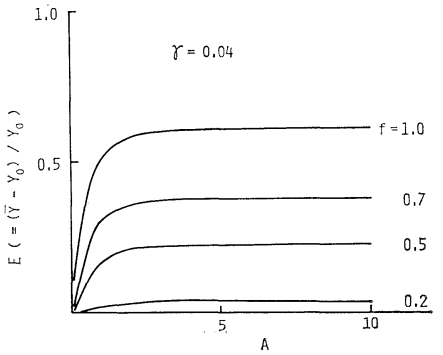

Fig. 6. Dependence of the normalized error E upon the parameter A. Here, γ is taken to be 0.04.

KARWEIT (1974) studied response of the Savonius rotor experimentally. His experimental values are plotted also in Fig. 5 and show that the error E increases with f. The numerical curves are in agreement with his experimental data qualitatively and the value $\gamma=0.04$ derived already from the Gaul's data is also recognized.

Case b ($U_0=0$): For the case of pure oscillatory flow, U_0 in (7) is neglected and a non-dimensional form of the rotation equation similar to (8) is obtained by using the characteristic scales ω_1 ($=u_{\max}/r_e$) and β as follows:

$$A'\frac{dY'}{dt}=p(|\sin t|-Y')^2-\gamma(|\sin t|+Y')^2, \quad (23)$$

where $A'=2I\beta/\rho s r_e^3 C_D^+\omega_1$ and $Y'=\omega/\omega_1$. A numerical solution of (23) for $\gamma=0.04$ and $A=5.0$ is shown in Fig. 7. Although the averaged current speed is zero, the rotational frequency becomes to have a positive mean value Y_w ($=\omega_w/\omega_1$). Thus, the current meter will erroneously record a mean current denoted by U_w (or $r_e\omega_w$). With the aid of the relation (11), the ratio of U_w to $u_{\max}$ is given by

$$\frac{U_w}{u_{\max}}=\frac{1}{r_e\omega_1}\left(\frac{r_e\omega}{g(\gamma)}\right)=\frac{Y_w}{g(\gamma)}. \quad (24)$$

In this case, since $g(\gamma)=0.667$ and $Y_w=0.557$, the ratio $U_w/u_{\max}$ is 0.835 approximately. Dependence of $U_w/u_{\max}$ upon γ and A' is illustrated in Fig. 8. The value of $U_w/u_{\max}$ decreases when γ increases, and has almost constant values for large γ. On the other hand, the value increases with A', and for the value of A' larger than 5.0, the value $U_w/u_{\max}$ does not increase significantly. When A' decreases, the value decreases and tends to be $2/\pi$, which reveals the value of the ratio $\bar{u}/u_{\max}$, where $\bar{u}=\frac{1}{T}\int_0^T\left|u_{\max}\sin\frac{2\pi}{T}t\right|dt$.

Laboratory experiments similar to Karweit's are also conducted in our laboratory for the Aanderaa's rotor under zero mean currents. The results are summarized as follows: (i) in any case, $U_w/\bar{u}$ is greater than 1, (ii) as shown in Fig. 9, the ratio $U_w/u_{\max}$ is 0.9 ± 0.04 for $\xi_0\gtrsim10$ cm, and is almost independent upon the frequency of oscillations, where ξ_0 is the orbital diameter of the oscillatory flow, (iii) for $\xi_0\lesssim5$ cm,

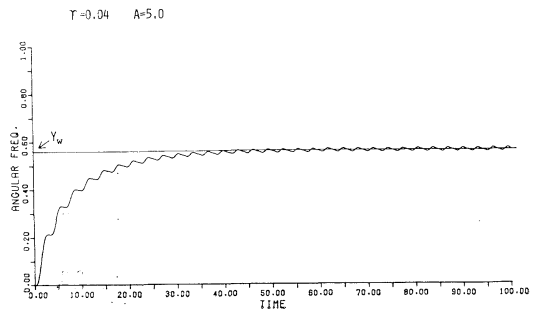

Fig. 7. Time history of normalized rotational frequency for a pure oscillatory flow. Although the averaged current speed is zero, the rotational frequency shows a positive mean value Y_w.

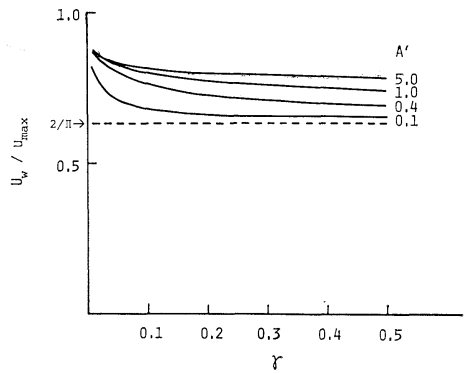

Fig. 8. Dependence of the "apparent" current U_w upon the parameter γ and A'. $2/\pi$ in ordinate represents the ratio $\bar{u}/u_{\max}$, where $\bar{u}=\frac{1}{T}\int_0^T\left|u_{\max}\sin\frac{2\pi}{T}\right|dt$.

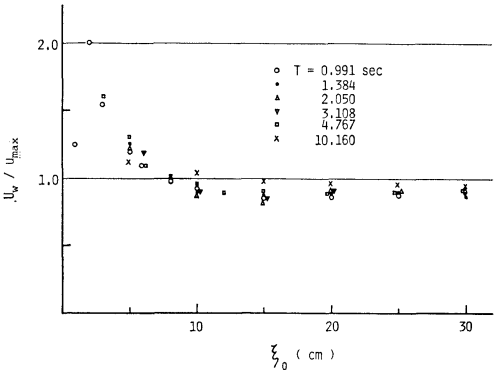

Fig. 9. Experimental results of the "apparent" current U_w for pure oscillatory flow. Abscissa represents orbital diameter ξ_0.

$U_w/u_{\max}$ is rather large and sometimes greater than 1. The results (i) and (ii) are in agreement with those of numerical computations. The meaning of the result (iii), however, is not clearly understood yet. Further investigation under such conditions is desired in connection with the structure of induced secondary flow and/or an oscillatory turbulent flow around the rotor.

4. Discussion

The order estimation of the torque N: A hydrodynamical torque acting of a rotor vane is already expressed by (2). The ratio R of the second term in right side of (2) to the first term is given by

$$R \equiv \frac{\rho s r_e C_M(\alpha) \cdot dU_e/dt}{1/2\,\rho C_D(\alpha) U_e^2 s r_e} = 2 \cdot \frac{C_M(\alpha)}{C_D(\alpha)} \cdot \frac{d}{U_e^2} \cdot \frac{dU_e}{dt}. \quad (25)$$

Let T denote the period of oscillatory flow, the order of dU_e/dt is $2\pi U_e/T$. Since the order of C_M/C_D might be unity, $R \sim O\left(\frac{d}{U_e^2} \cdot \frac{dU_e}{dt}\right) \sim O\left(\frac{d}{TU_e}\right) \sim O\left(\frac{d}{\xi_0}\right)$. When the thickness of the rotor vane d is negligibly smaller than the orbital diameter ξ_0, the second term in (2) can be neglected.

The torque acting on rotational disks: It is well-known that a rotor has two (Aanderaa rotor) or three (Savonius rotor) rotational disks. A negative torque N_d caused by relative motion of fluid acts on disks. FUJINAWA (1978) gives such a torque as follows:

$$-N_d = 1/2\,\rho\omega^2 R_0^5 C_R + 1/2\,\eta\rho R_0^5 C_R \frac{d\omega}{dt}, \quad (26)$$

where R_0 denotes a radius of a disk, C_R a constant related to Reynolds number and η a nondimensional constant of order O (0.1). The negative torque N_d has two terms, one of which is a frictional term and is proportional to ω^2, and the other originates from virtual mass and has an effect to increase apparently the moment of inertia of a rotor from I to I' $(=I+1/2\eta\rho R_0^5 C_R)$.

Frictional effect: Based on the above discussion, a nondimensional form of a rotation equation including the torque acting on disks is derived as follows:

$$A\frac{dY}{dt} = p(1+f\sin t - Y)^2 - \gamma(1+f\sin t + Y)^2 - \alpha' Y^2, \quad (27)$$

where $\alpha' = R_0^5 C_R/s r_e^3 C_D^+$ and the moment of inertia I in A is modified to I'. The analytical solution similar to (10) is given by

$$Y = \frac{1+\gamma-\sqrt{4\gamma-\alpha'\gamma+\alpha'}}{1-\gamma-\alpha'} \equiv g'(\gamma, \alpha'), \quad (28)$$

and the ratio, denoted by τ'_{AD}, of two time constants is

$$\tau'_{AD} = \frac{2(1-\gamma-\alpha')\sqrt{4\gamma+(1-\gamma)\alpha'}}{(2\gamma+\alpha')(1+\gamma-\sqrt{4\gamma+(1-\gamma)\alpha'})}. \quad (29)$$

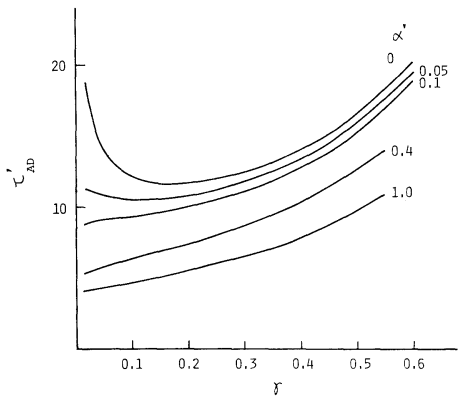

Fig. 10. Frictional effect on rotor response. Ordinate represents the ratio of a time constant of negative change of the flow speed to positive one.

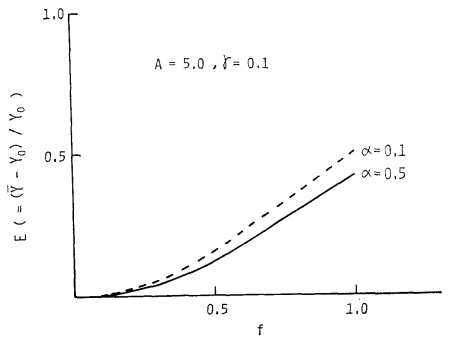

Fig. 11. Frictional effect on the error E.

For small values of γ, say $\gamma \ll 1$ and $\gamma \ll \alpha'$,

$$g'(\gamma, \alpha') = \frac{1}{1+\sqrt{\alpha'}}\left(1+\frac{\alpha'\sqrt{\alpha'}+3\alpha'-4}{2(1-\alpha')\sqrt{\alpha'}}\gamma\right) \tag{30}$$

and

$$\tau'_{AD} = 2(1+\alpha'^{-1/2}) + O(\gamma). \tag{31}$$

The relation (31) shows that τ'_{AD} decreases with α'. This tendency is found also for larger γ as shown in Fig. 10. Numerical solution for unidirectional oscillatory flow shows that the frictional effect reduces the error E slightly as shown in Fig. 11.

5. Concluding remarks

Dynamic response of a rotor to unsteady flows is studied. A simple two rotor-vane model is proposed, in which the rotation of a rotor is described by only two parameters. One is the ratio γ of the normal drag coefficients of both sides of a rotor-vane, and the other A is the nondimensional moment of inertia of a rotor.

By the present model, response times of the rotation to negative and positive stepwise changes of a flow are estimated. The ratio of these two time constants is found to be a function of γ only. Therefore, γ can be evaluated from the experimental values of response times for stepwise changes of a flow; for example, γ is estimated to be 0.038 for the Savonius rotor based on the experimental data by GAUL *et al.* (1963).

The model is applied to a unidirectional flow, the magnitude of which fluctuates sinusoidally, and positive errors in current measurements are estimated. The dependence of the error upon the two prameters, γ and A, is as follows: the smaller the value of γ is, the larger the error is. For a fixed value of γ, the error increases with A and becomes a constant value for fairly large value of A. If the values of γ and A are taken to be 0.04 and 5.0, respectively, the estimated errors are fairly in agreement with those of a laboratory experiment by KARWEIT (1974).

The present model is also applied to the case of a pure oscillatory flow. The estimated "apparent" current speeds are 0.8~0.9 times as large as the maximum speeds of the oscillatory flows. These values are favourably compared with those of the experimental results for the Aanderaa's rotor.

Frictional effect is taken into consideration and it is concluded that those errors are reduced slightly.

In this paper, the error in current measurements is estimated only in connection with the response of a rotor. In the actual field, however, other errors in current measurements must be caused by the motion of a direction sensing vane, fluctuation of a mooring system and so on, in conjunction with the sampling interval. Even if our interest is focused on a response of a rotor, several problems have not been solved yet; how does the rotor respond to non-monotonic or two dimensional fluctuations such as wind waves and so on? It is desired to solve above problems and estimate errors more precisely for refinement of a large number of recent current data obtained by the rotor type current meter near the sea surface. The simple model presented here might give a clue to such problems.

Acknowledgements

The authors wish to express their hearty thanks to Dr. S. UNOKI, Institute of Physical and Chemical Research, for his encouragement during the present study. The authors also express sincere thanks to Dr. Y. FUJINAWA, the National Research Center for Disaster Prevention, and Dr. M. FUKASAWA, Ocean Research Institute, University of Tokyo, for their fruitful discussion throughout the study. Thanks are extended to Ms. Y. IMADA for her typing the manuscript and drafting figures.

References

BEARDSLEY, R. C., W. BOICOURT, L. C. HUFF and SCOTT (1977): A current meter intercomparison experiment conducted off Long Island in February-March, 1976. Technical Rep. Woods Hole Oceanogr. Inst., **62**, 102 pp.

FUJINAWA, Y. (1977): Dynamic property of current meter. Preservation of Marine Environment § 14.3. *In* S. HORIBE (ed.): Report of the Special Project Research, Ministry of Education, Science and Culture, p. 215-233. (in Japanese).

GAUL, R. D., J. M. SNODGRASS and D. J. CRETZLER (1963): Some dynamical properties of the savonius

rotor current meter. *In* Marine Sciences Instrumentation, 2. Instrument Soc. America, Plenum Press, p. 115-125.

KAGANOV, E. I. and A. M. YAGLOM (1976): Errors in wind-speed measurements by rotation anemometers. Boundary-Layer Meteorol., **10**, 15-34.

KARWEIT, M. (1974): Response of savonius rotor to unsteady flow. J. Mar. Res., **32**, 359-364.

KONDO, J., G. NAITO and Y. FUJINAWA (1971): Response of cup anemometer in turbulence. J. Meteorol. Soc. Japan, **49**, 63-74.

MACCREADY, P. B. (1966): Response characteristics and meteorological utilization of propeller and vane wind sensors. J. Appl. Meteorol., **3**, 182-193.

SAUNDERS, P. M. (1975): Near-surface current measurements. Deep-Sea Res., **23**, 249-257.

非定常な流れに対するサボーニアス型ローターの応答特性

長島秀樹，岡崎守良

要旨: ローター型流速計の応答特性を簡単な 2-vane model を用いて調べた。このモデルではローターの特性は仮想的な1枚の vane の両面の，流れに対する抵抗係数の比と，無次元化されたローターの慣性モーメントで記述される。このモデルを一定の向きの流れで，その強さが時間と共に正弦的に変動する場合に適用し，平均流を測定する際に生じる誤差を見積った。その結果は KARWEIT (1974) の実験結果をよく説明した。

次にこのモデルを，単に時間と共に正弦的に振動する流れに適用し，その場合に現われる見かけの流速を見積った。その結果は，サボーニアス型ローターに対する室内実験結果とよく一致した。これによると，振動する流れの最大流速の 80～90 % が，見かけの平均流速として測定されることになる。

La mer 20: 190-192, 1982
Société franco-japonaise d'océanographie, Tokyo

日仏海洋学会賞受賞記念講演

海洋における生体元素，特に珪素の循環機構に関する研究*

鎌　谷　明　善**

Recherches sur les mécanismes de circulation des bioéléments, particulièrement du silicium, dans la mer*

Akiyoshi KAMATANI**

この度は，計らずも学会賞を戴き，身にあまる光栄に深く感謝いたします。それとともに責任の重さを痛感しております。この研究は完成されたものではなく，むしろその緒をつかみ問題を提起したにすぎません。今後の皆様方の一層のご支援とご鞭撻のほどをお願いいたします。

生物シリカへのプレリュード　まず，珪素の化学的性質についてみますと，次のような位置づけにあるといえましょう。珪素は地殻の 27.7％を占め，酸素に次いで多い元素であります。そして，周期表の第4族，所謂炭素族に属しています。自然界で炭素は，C−C, C=C, C≡C 結合，あるいは他の元素との結合を通じて，複雑な高分子化合物をつくっていますが，珪素の Si−Si は C−C よりも不安定で，このような結合様式の天然化合物の存在は現在のところ確認されていません。天然に存在する珪素化合物の総ては酸素を介した Si−O 構造を基本としています。炭素の酸素化合物 CO_2 は常温において気体でありますが，SiO_2 は固体であります。このような化学的性質の相違はまた，自然界における両元素の位置関係にも如実に現われています。即ち，炭素は生物界の中心的な役割を果しているのに対し，珪素は鉱物の構造構成の根幹をなしているということであります。

しかし，生物にとって珪素がまったく無用の存在であるわけではありません。生育していく上で，この元素を多量に必要とする生物も少なくありません。その代表に海洋の基礎生産の担い手としての珪藻を挙げることができます。陸上においてもイネ科の植物を始め多くの植物に利用されています。これらの植物によって消費される量は年間数100億トンに及ぶものと見積られます。なかでも，珪藻は植物界でのユニークな存在といえます。それは，他の植物に比べて多量の珪素を必要とすることに加えて，神秘的なまでに美しい幾何学的構図の珪酸殻を造り出すということであります。高等動物にとって珪素は生物学的に不活性であり，また生理的にも無用の元素と考えられていましたが，この10年来の生物に対する微量元素の役割に関する研究の中で，珪素が生体内のあらゆる組織や器官に微量ながらも含まれており，しかも正常な機能を営むに不可欠な存在であることが明らかにされてきました。このように，珪素は生命化学と深い係りを持つ元素とみなされるようになってきました。そして，珪藻が珪素代謝の研究のモデル生物の代表に取り上げられようとしています。生命過程のメカニズムや生体内の機能と構造についての新しい多くの知見が，珪藻を用いた研究を

---

* 1982年5月28日，日仏会館(東京)にて講演
Résumé de la conférence faite le 28 Mai 1982 aprés la remise du Prix de la Société franco-japonaise d'océanographie

** 東京水産大学 Université des pêches de Tokyo

通してえられる可能性の強いものと期待されましょう。

海洋におけるおおよその珪素収支は次のようであります。河川から運び込まれる量は年間 $43\times10^{13}SiO_2g$ であるのに対し，生物に消費される量は $25\times10^{15}g$ とされています。即ち，生物シリカの溶解速度と溶解割合の如何によっては，海水中のシリカ濃度は時代とともに減少し，ひいては珪藻の増殖の制限因子となるまでに低下していく可能性も生じるということであります。このように，生物による消費とその後の挙動が，海洋における珪素の循環機構を研究していく上で重要な位置づけにあることがわかります。また，堆積物中の珪藻遺骸の分布や量を知ることは，古海洋における生物生産の分布様式や環境の変遷過程を解き明かす緒を与えてくれる点からも興味がもたれるところであります。

生物シリカの性質　今日までに知られている生物シリカの総ては非晶質シリカでありまして，鉱物学や岩石学の研究対象から無視され，その狭間に存在してきた薄幸な化合物であります。非晶質シリカの海水への溶解度は 70 mg SiO_2/l 程度でありますが，海洋のシリカ濃度はたかだか 10 mg SiO_2/l でありまして，未飽和状態にあるといえます。それにも拘らず，海底に多くの海綿の骨針や珪藻殻が沈積し，長い間残っていることは興味ある問題といえます。そこで赤外線吸収スペクトルによる生物シリカの構造解析を試みましたところ，珪藻殻は合成シリカに類似した表面にシラノール基の多い吸収パターンを示しましたが，海綿の骨針はシラノール基に乏しいオパールに属する性質に近いということが判りました。なお，注目すべきことに，地質年代を経た珪藻殻はシリカゲルとオパールの中間に位置しているということでありました。これは，地質年代を経て結晶化する初期に表面のシラノール基が徐々に消失していくことを示唆しているということであります。生物シリカが続成作用を受けて結晶化する速度は，温度や共存物質の性質によって支配されますが，海底堆積物で結晶化するに要する時間は数百万～数千万年のオーダーとされています。

堆積物中に残る生物シリカは特殊な種に限られるようであります。これは生物がつくり出すシリカの溶解及び変質の受け方に違いがあるためと考えられます。そこで，このような変化の受け方の違いが種間にあるかどうかを見分ける方策の一つとして，珪藻殻を熱処理に付し，反応を促進させた場合に生じる現象から調べてみました。その結果，次のような事柄が判明しました。(1) 1000°C 以下の処理では結晶化しないが，シラノール基は消失する。消失度合は処理温度により異なる。(2) 500°C 以下の温度で処理した試料は室内に放置すると，大気中から水分を吸収し，再びシラノール基は回復する。しかし，700°C 以上の温度で処理すると回復は緩慢となり且つ回復割合も小さくなる。このことは，表面に生じた結合が簡単に加水分解されない性質に変化していくこと，並びに局部的にシンターリングをおこすことを示唆している。(3) このような方法では種間における変質割合とその速度の違いを定量的に把えることは技術的に困難であったが，続成作用を受け，変質していく過程を傍証する有効な手段であった。

生物シリカの溶解　地質年代を経た珪藻殻のシラノール基は，現生のものよりも少なくなっていたこと，また，熱処理により消失することから，シラノール基の多少が溶け方と深い関係にあることが推測されます。そこで，異なった温度で処理した珪藻殻の溶け方を 2% Na_2SO_4 溶液 (100°C 60分) について調べましたところ，著しい違いのあることがわかりました。*Rhizosolenia hebetata* は 200°C 前後の処理ですでに難溶化が始まり，処理温度を高めるにつれ難溶化は漸進していました。次いで難溶化されやすいのは *Skeletonema costatum* と *Cyclotella nana* でありました。*Chaetoceros* sp. は 500°C に至って始めて難溶化の兆が現われました。シリカゲルは 700°C を境に急激に難溶化しますが，この温度は丁度シラノール基の消失と回復の可逆性が失なわれる温度であった点で，特に注目される現象といえます。一方，珪藻土 (*Stephanodiscus niagerae, Cyclotella comuta*) は 2～4% の溶解にとどまり，海綿の骨針は 1% 程度でありました。しかし，これらいず

れの生物シリカも2% Na_2CO_3 溶液には完全に溶ける性質でありました。

生物シリカの溶解をどのような尺度で測定するかは，甚だ厄介な問題であります。それは，この溶解機構が不均一反応系に属するうえに，次のような諸々の要素を考慮しなければならないからであります。即ち，(1) 殻の厚さ，大きさ，有効表面積，(2) 有機被膜の化学組成，(3) 表面を保護しようとするような物質（有機，無機）の吸着，(4) 溶液の条件（pH, 温度, イオン強度等）であります。これらの要素を考慮に入れ，溶解速度を取り扱う方法を検討しましたところ，疑一次反応式で取り扱うのが簡便であることがわかりました。この方法で各種の珪藻からのシリカの溶解について調べましたところ，有機物を除去することにより溶解速度定数は 4〜5 倍大きくなりました。また，溶解初期の速度定数(K_1/時) と温度(T°C) との間には $\ln K_1=\alpha+0.0833T$ の関係が見出されました。α は種に特異的な因子でありまして，-7.35〜-10.38 の範囲に納まるようでありました。この式は温度が 10°C 上昇することにより速度定数が約 2.3 倍大きくなることを示しています。一般に速度定数は大型珪藻よりも小型のものが大きくなる傾向が見られました。これらの結果は，水温の高い海域よりも低い海域で生物シリカは溶解しにくく，海底に沈積しやすいこと，並びに小型よりも大型珪藻の方がよりこの傾向の強まることを意味しておりまして，実際の海洋にみられる分布状況を説明するに十分な妥当性のあることを示しています。

他の生体元素との関係　培養をおこないました珪藻を暗所に保存し分解させますと，燐や窒素の無機化に先行してシリカの溶出が観られましたが，動物プランクトンや原生動物を共存させますと，窒素や燐の分解は著しく促進されますために，見掛け上はシリカの溶解が遅れるようになります。従いまして，再生時の窒素と燐の比は終始ほぼ一定しているのに対し，珪素と燐の比は分解の進行に伴ない増大していました。これは海洋の表層で珪素と燐の比が小さく深層にゆくにつれ増大する現象をよく説明しています。

ベーリング海を一例に有機炭素と生物シリカの挙動について調べてみましたところ，生産された有機炭素の 98% は堆積物中に埋蔵される以前に分解されるのに対し，生物シリカは約 50% が溶解するにすぎない結果が得られました。今日迄の通説では生物シリカの 90% 近くはすみやかに溶け出し，1% 程度が堆積物中に残るとされていますので，ベーリング海は特異的な海域かも知れません。堆積物中での有機炭素の分解速度定数を計算してみましたところ，$0.43\text{〜}1.0\times10^{-4}$/年でした。一方，生物シリカの溶解度定数は $1.2\text{〜}1.8\times10^{-4}$/年で，実験から予測されるよりも2桁小さい値でした。この原因は，溶け出したシリカの拡散速度が小さいこと，珪酸殻の表面への有機物や無機物の吸着による有効表面積の低下，続成作用による難溶化などによるものと考えられます。しかし，海洋における珪素の循環を詳細に解析するに必要な基礎的研究が少なく，今後に期待されるところが大きいといえましょう。

学　会　記　事

1. 昭和57年5月17日，東京水産大学において評議員会が開かれた。
   1) 会務報告および編集報告が行われた。
   2) 学会賞受賞候補者として鎌谷明善氏が推薦され，受賞者として決定された経過が報告された。
   3) 昭和56年度の収支決算および昭和57年度の予算案が審議された。
   4) 会則第10条について審議し，「常任幹事 5名」を「常任幹事　若干名」と改正することが決定された。
   5) 役員および編集委員の選出が行われた。
   6) 昭和57年度学会賞受賞候補者推薦委員の選出について協議し，下記の通り決定された。
   阿部友三郎，有賀祐勝，石野　誠，井上　実，岡見　登，鎌谷明善，斎藤泰一，佐藤任弘，根本敬久，松生　洽，丸茂隆三，村野正昭，森田良美
   7) 会則第4条に基づく分科会について審議し，研究部会を設置して活動を活発にすることが決定され，研究部会の世話人を関文威氏に依頼することが承認された。
2. 昭和57年5月28日，日仏会館会議室において第23回総会が開かれた。
   1) 昭和56年度の会務報告および会計報告が行われた。なお，別表の収支決算が承認された。
   2) 編集委員長(代理)から，学会誌 La mer 第19巻の編集経過報告が行われた。第19巻は総ページ数 209 ページで，その内訳は原著論文23篇（和文13，英文9，仏文 1)，寄稿1篇，資料1篇，記念講演1篇，その他学会記事などである。
   3) 学会賞受賞者として鎌谷明善氏が決定に至る経過が報告された。
   4) 昭和57年度予算案について審議の結果，別表の通り承認された。

昭和56年度収支決算

収　入

事　項	決算額(円)
前年度繰越金	27,173
正会員会費	1,557,200
賛助会員会費	835,000
学会誌売上金	196,111
広　告　料	410,000
著者負担印刷費	81,000
雑　収　入	3,258
計	3,109,742

支　出

事　項	決算額(円)
学会誌等印刷費	1,980,600
送料・通信費	265,455
編　集　費	60,000
事　務　費	601,920
交　通　費	150,100
会　議　費	14,550
次年度繰越金	37,117
計	3,109,742

昭和57年度収支予算

収　入

事　項	予算額(円)
前年度繰越金	37,117
正会員会費	1,755,000
賛助会員会費	830,000
学会誌売上金	180,000
広　告　料	480,000
著者負担印刷費	90,000
雑　収　入	3,500
計	3,375,617

支　出

事　項	予算額(円)
学会誌等印刷費	2,100,000
送料・通信費	270,000
編　集　費	60,000
事　務　費	700,000
交　通　費	150,000
会　議　費	20,000
予　備　費	75,617
計	3,375,617

5) 昭和57，58年度の評議員が選出された。また，常任幹事，幹事，監事が承認された。（いずれも本誌196 ページの役員名簿を参照）

6) 編集委員長および編集委員が承認された。（本誌表紙裏の編集委員会名簿を参照）

7) 分科会として研究部会の設置について報告があった。

3. 総会終了後，引続き学会賞授与が行われた。

昭和57年度学会賞受賞者：鎌谷明善氏（東京水産大学）。

受賞課題：海洋における生体元素，特に珪素の循環機構に関する研究（別項「推薦理由書」参照）。

会長から鎌谷氏に賞状，メダルおよび賞金が授与され，続いて受賞記念講演が行われた。

4. 受賞記念講演終了後，懇親会が開かれ，盛会であった。

5. 昭和57年5月28日，日仏会館会議室において昭和57年度学術研究発表会が次の通り行われた。

午前の部

1. 安定海水泡沫の飛散機構—飛散臨界風速について…阿部友三郎，高橋一民（東理大・理）
2. Moiré の方法による水波の解析（その3）
……阿部友三郎，高山晴光(東理大・理)
森谷誠生（気象協会）
3. 構造物周辺で生ずる波浪循環流に関する実験的研究（1）…… 糸洌長敬，五明美智男（東水大）
4. 深海底堆積物の工学的測定(せん断力について)
…… 小林平八郎（東海大・海洋）
5. 赤潮のシステム・モデル
…… 辻田時美（三洋水路，東海大・海洋）
6. OHLE 理論が関与する海洋の物質代謝
…… 関　文威（筑波大・生科系）
7. 中栄養水塊における細菌の栄養摂取に関する研究 ……姜　憲，関　文威（筑波大・生科系）

午後の部

8. 春季霞ケ浦における植物プランクトンの動態Ⅳ．植物プランクトンブルームの発生制限因子
…… 麻崎昭仁（筑波大・環境科学），
関　文威（筑波大・生科系）
9. 春季霞ケ浦における植物プランクトンの動態Ⅴ．植物プランクトンの増殖機構
…… 土田　明（筑波大・環境科学），
関　文威（筑波大・生科系）

特別講演

Primary Production of the Lagoon of an Atoll in French Polynesia……Professor Alain Sournia (Muséum National d'Histoire Naturelle, Paris)

学会賞受賞記念講演

海洋における生体元素，特に珪素の循環機構に関する研究 ……鎌谷明善（東水大）

6. 昭和57年7月10日，東京水産大学において編集委員会が開かれ，La mer 第20巻第3号の編集を行った。

7. 新入会員

氏　名	所　属	紹介者
本座　栄一	通産省工業技術院地質調査所	関　文威
温　保華	山東海洋学院	佐々木忠義
隆島　史夫	東京水産大学	佐々木忠義
宮崎　龍雄	筑波大学生物科学系	関　文威
Alain Sournia	Ichtyologie Générale et Appliquée, Muséum National d'Histoire Naturelle	有賀　祐勝
前田　昌調	東京大学海洋研究所	根本　敬久
稲葉　栄生	東海大学海洋学部	渕　秀隆
岡市　友利	香川大学農学部	佐々木忠義
望月　賢二	東京大学総合研究資料館水産動物部門	阿部　宗明
高橋　正征	筑波大学生物科学系	有賀　祐勝
江面　浩	筑波大学生物科学系	関　文威

8. 退会者 （正会員）前地道義 （賛助会員）㈱東邦電探

9. 会員の住所・所属の変更

氏　名	新住所または所属
山本　秀行	〒230 横浜市鶴見区生麦1-6-11 新日本空調　生麦寮
山路　勇	〒640 和歌山市九家の丁 7-1
福田　雅明	三洋水路測量㈱
深沢　文雄	東亜大学
南　四郎	〒751 下関市向洋町1-18-9

10. 交換および寄贈図書

1) 農業土木試験場報告　第22号
2) 農業土木試験場場報　No. 33, 34
3) 日本航海学会論文集　第66号
4) 航　海　第71，72号
5) Bulletin of the Ocean Research Institute,

University of Tokyo　No. 14
6) 海産研ニュース　No. 3
7) 研究実用化報告　Vol. 31　Nos. 5, 6, 7
8) 東北区水産研究所研究報告　第44号
9) 神戸海洋気象台彙報　No. 200
10) 国立科学博物館研究報告　Vol. 18 No. 1
11) Preliminary Report of the Hakuhō Maru Cruise KH-75-3, KH-77-3
12) 海洋資料センター所蔵資料目録　JODCニュース増刊号　第12
13) JODCニュース
14) RNODC Newsletter for WESTPAC　No. 1
15) WESTPAC Data Management Guide
16) 海洋産業研究資料　Vol. 13 Nos. 4, 5, 6
17) 水産工学研究所技報　第3号
18) なつしま　No. 58
19) 鯨研通信　第344, 345号
20) 早稲田大学理工学部紀要　第45号
21) 理化学研究所科学講演会記録　第4回
22) 東海大学海洋学部業績集　第11集
23) 東海大学紀要　海洋学部　第15号
24) 海洋時報　第25号
25) 海洋地質図　17, 18, 19
26) 神奈川県立博物館研究報告自然科学　13号
27) ガザミの増殖研究
28) 広島県水産試験場事業報告　55年度
29) 広島県水産試験場研究報告　No. 12
30) Bulletin of the National Science Museum　Vol. 18 No. 2
31) Bulletin de l'institut de géologie du bassin d'aquitaine N° 30
32) Science et pêche　N° 316-321
33) 科学通報　Vol. 27 Nos. 4, 5
34) Revue des travaux de l'institut des pêches maritimes Tome 44, Fasc. 4

日仏海洋学会賞受賞候補者推薦理由書

氏　名: 鎌　谷　明　善（東京水産大学）

題　名: 海洋における生体元素，特に珪素の循環機構に関する研究

推薦理由: 珪素は海洋において，栄養元素の一つであり，また水塊のトレーサーとしても重視される元素である。そのために，珪素の分布と変動に関する研究は古くから行われてきた。しかし，海洋における珪素の循環にかかわる生物，なかんずく珪素を特異的に要求する珪藻類の役割については，まだ多くの問題が残されている。それは主として珪藻殻の形成に関する生化学的機構，および珪藻殻の溶解の難易性の解明にある。鎌谷明善博士はこれらの点に着目し，浮遊性珪藻類の培養を行なって珪素の取込みと溶解についての実験を試みる一方，生物体珪酸の溶解性の差異を物理化学的手法を用いて研究し，幾多の重要な知見を発表してきた。

鎌谷博士は，まず生物体珪酸の構造解析に赤外線吸収スペクトルを応用し，溶解の難易性がシラノール基(Si-OH)の多少と密接な関係にあることを明らかにした。併せて，現棲の珪藻殻が地質年代を経て難溶化するに至る間に，X線回折では非晶質で顕著な変質のみられない段階において，既にシラノール基の消失が起きているという新しい知見を得た。これらの業績は，国際的見地からみても先駆的なものであり，海洋の化学・生物学分野はもとより，古生物学，地質学，鉱物学など広い分野の研究者から注目され，多くの論文に引用されている。さらに同博士は，珪藻殻の溶解現象の理論的な取り扱いについて検討を加え，溶解速度が珪藻種間で一定の序列を示すこと，並びに溶解速度定数が温度に強く依存することを明らかにし，これらを数量的に表わす方法を確立した。これらの研究成果は今後海洋における珪藻殻の分布と挙動を解析してゆく上での極めて重要な基礎的資料を提供したものといえる。

鎌谷博士はまた，従来の生物珪酸の分析法に検討を加え，生物体珪酸と非生物体珪酸が複雑な割合で混在する懸濁物や堆積物を対象として，簡便迅速な方法を確立した。これは海洋での珪素の循環における生物体珪酸の役割を正しく評価してゆく上で大きな意義をもつものである。

鎌谷博士は，珪素のみならず，炭素，窒素，燐など他の生体元素の海洋における循環機構の解析も併せて行なってきた。そして，珪素が他の生体元素と大きく異なった挙動を示すことを実証し，海洋における分布の特異性の解明を試みつつある。

鎌谷博士のこれまでの優れた研究業績は，海洋科学の進展に貢献する所が顕著であり，世界的にも高く評価されている。本委員会は同氏を日仏海洋学会賞の受賞者にふさわしいものと判断し，ここに推薦する次第である。

学会賞受賞候補者推薦委員会
委員長　井　上　　実

主 要 論 文

1969: Regeneration of inorganic nutrients from diatom decomposition. J. Oceanogr. Soc. Japan, **25**, 63-74.

1971: Physical and chemical characteristics of biogenous silica. Mar. Biol., **8**, 89-95.

1974: Studies on the dissolution of diatomaceous silica as a function of heating. J. Oceanogr. Soc. Japan, **30**, 157-162.

1975: Fluctuation of dissolved organic carbon in seawater in Sagami Bay, during 1971-1972. J. Oceanogr. Soc. Japan, **37**, 43-47. (with N. OGURA, N. NAKAMOTO, M. FUNAKOSHI and S. IWATA)

1978: 生物体シリカの溶解機構に関する研究．日本プランクトン学会報，**25**，1-6．（中沢信之と共著）

1979: 海産珪藻による亜鉛の吸収について．日本水産学会誌，**45**，715-719．（高橋幹夫・森田良美と共著）

1979: 東京湾における懸濁物及び堆積物中の燐，珪素，炭素と窒素について．日本水産学会誌，**45**，1109-1114.

1979: Rate of dissolution of diatom silica walls in seawater. Mar. Biol., **55**, 29-35. (with J.P. RILEY)

1980: 植物プランクトンの分解にともなう燐と珪素の再生．日本水産学会誌，**46**，537-542．（上野康弘と共著）

1980: Determination of biogenic silica in marine sediment. La mer, **18**, 63-68.

1980: Dissolution of opaline silica of diatom tests in seawater. J. Oceanogr. Soc. Japan, **36**, 201-208. (with J.P. RILEY and G. SKIRROW)

1981: Distribution of nutrients in Sagami Bay during 1971-1973. Bull. Japan. Soc. Sci. Fish., **43**, 1493-1498. (with N. OGURA, N. NAKAMOTO, M. FUNAKOSHI and S. IWATA)

1982: Dissolution rates of silica from diatoms decomposing at various temperatures. Mar. Biol., **68**, 91-96.

1982: The kinetics of decomposition of biogenic silica and organic matter in the sediment of the Bering Sea. Geochim. Cosmochim. Acta (submitted).

日仏海洋学会役員

村野正昭，元田　茂，森川吉郎，森田良美，
森安茂雄，安井　正，柳川三郎，山口征矢，
山路　勇，山中鷹之助，山中一郎，山中　一，
吉田多摩夫，渡辺精一　（五十音順）
マルセル・ジュグラリス，ジャン・アンクティル，ロジェ・ペリカ

賛　助　会　員

旭化成工業株式会社	東京都千代田区有楽町 1-1-2　三井ビル
株式会社内田老鶴圃新社　内田悟	東京都千代田区九段北 1-2-1　蜂谷ビル
株式会社　オーシャン・エージ社	東京都千代田区神田美土代町 11-2　第1東英ビル
株式会社　オセアノート	東京都世田谷区北沢 1-19-4-202
小樽舶用電機株式会社	小樽市色内町 3-4-3
社団法人　海洋産業研究会	東京都港区新橋 3-1-10　丸藤ビル
協同低温工業株式会社	東京都千代田区神田佐久間町 1-21　山伝ビル
小松川化工機株式会社	東京都千代田区岩本町 1-10-5　TMMビル5F
小山　康三	東京都文京区本駒込 6-15-10　英和印刷社
三信船舶電具株式会社	東京都千代田区神田 1-16-8
三洋水路測量株式会社	東京都中央区日本橋堀留町 1-3-17
シュナイダー財団極東駐在事務所	東京都港区南青山 2-2-8　DFビル
昭和電装株式会社	高松市寺井町 1079
新日本気象海洋株式会社	東京都世田谷区玉川 3-14-5
株式会社鶴見精機	横浜市鶴見区鶴見中央 2-2-20
株式会社東京久栄	東京都中央区日本橋 3-1-15　久栄ビル
東京製綱繊維ロープ株式会社	東京都中央区日本橋室町 2-6　江戸ビル
中川防蝕工業株式会社	東京都千代田区神田鍛冶町 2-2-2　東京建物ビル
日本アクアラング株式会社	神奈川県厚木市温水 2229-4
日本テトラポッド株式会社	東京都港区新橋 2-1-13　新橋富士ビル9階
社団法人　日本能率協会	東京都港区芝公園 3-1-22　協立ビル
深田サルベージ株式会社	東京都千代田区神田錦町 1-9-1　天理教ビル8階
藤田峯雄	茨城県北相馬郡藤代町大字毛有 850　株式会社 中村鉄工所
古野電気株式会社	東京都中央区八重洲 4-5　藤和ビル
丸文株式会社	東京都中央区日本橋大伝馬町 2-1-1
三井海洋開発株式会社	東京都千代田区一ツ橋 2-3-1　小学館ビル
宮本悟	東京都中央区かちどき 3-3-5　かちどきビル　㈱本地郷
株式会社ユニオン・エンジニアリング　佐野博持	神戸市中央区海岸通 3-1-1　KCCビル4F
吉野計器製作所	東京都豊島区駒込 7-13-14
株式会社読売広告社	東京都中央区銀座 1-8-14
株式会社離合社	東京都千代田区神田鍛冶町 1-10-4
株式会社　渡部計器製作所	東京都文京区向丘 1-7-17

お　知　ら　せ

本学会が協賛団体の一員となっている講演会が下記の通り開かれますのでお知らせします。

理化学研究所科学講演会

日　時　　昭和57年10月15日（金）　13時開場，13時20分開会

場　所　　経団連会館経団連ホール（14階）（東京都千代田区大手町 1-9-4）

後　援　　科　学　技　術　庁

協　賛　　関　連　学・協　会

講　演　題　目

1. 「日本の自動車車体の鋼板とプレスとそれらの評価法」
　　理化学研究所　主任研究員　吉　田　清　太
2. 「明日の資源を探し求めて宇宙と深海底へ」
　　理化学研究所　主任研究員　島　　誠
3. 「好アルカリ性微生物の世界」　理化学研究所　主任研究員　掘　越　弘　毅

聴講無料

連絡先　　理化学研究所　開発調査室
Tel. 0484-62-1111　内線 2301・2302

珊瑚美術館

「クイーン・コーラル」　↑
深海潜水艇“はくよう”により採集された，世界で一番美しい珊瑚。
高さ 1m　幅 1.2m　重さ 12kg
採集場所　徳之島近海
採集年月日　昭和54年7月4日

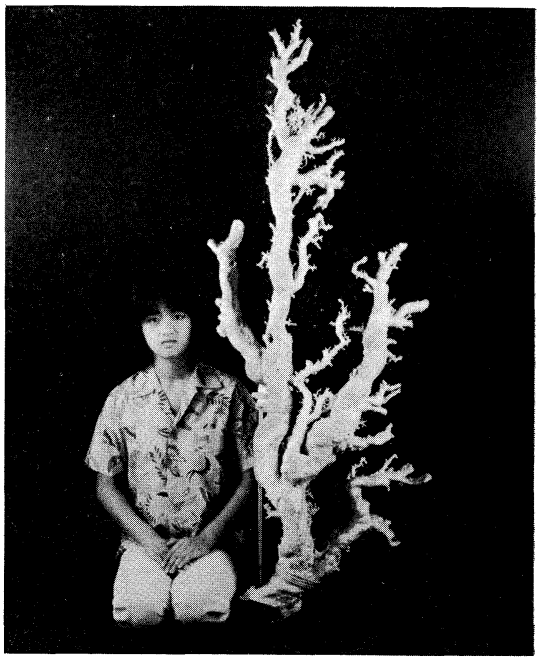

世界最大の珊瑚　→
高さ1.6m，重さ35kgの歴史上最大といわれる“ジャンボサンゴ”
採集場所　沖縄近海
採集年月日　昭和49年5月

花とさんごと美術館

沖縄さんご園

本　　社／〒903 那覇市首里金城町 3-5　☎ (0988) 86-3535 (代)
さんご園事業所／〒901-03 糸満市字摩文仁 1102　☎ (09899) 7-3535 (代)
ホテル店事業所／〒903 那覇市首里山川町 1-132-1　☎ (0988) 84-3535 (代)

ユニオン・エンジニアリングが
パーフェクトな観測をお約束する

海象・気象計測器

優れた精度・取扱い容易・世界的な実績・豊富な部品在庫・迅速確実なメンテナンス

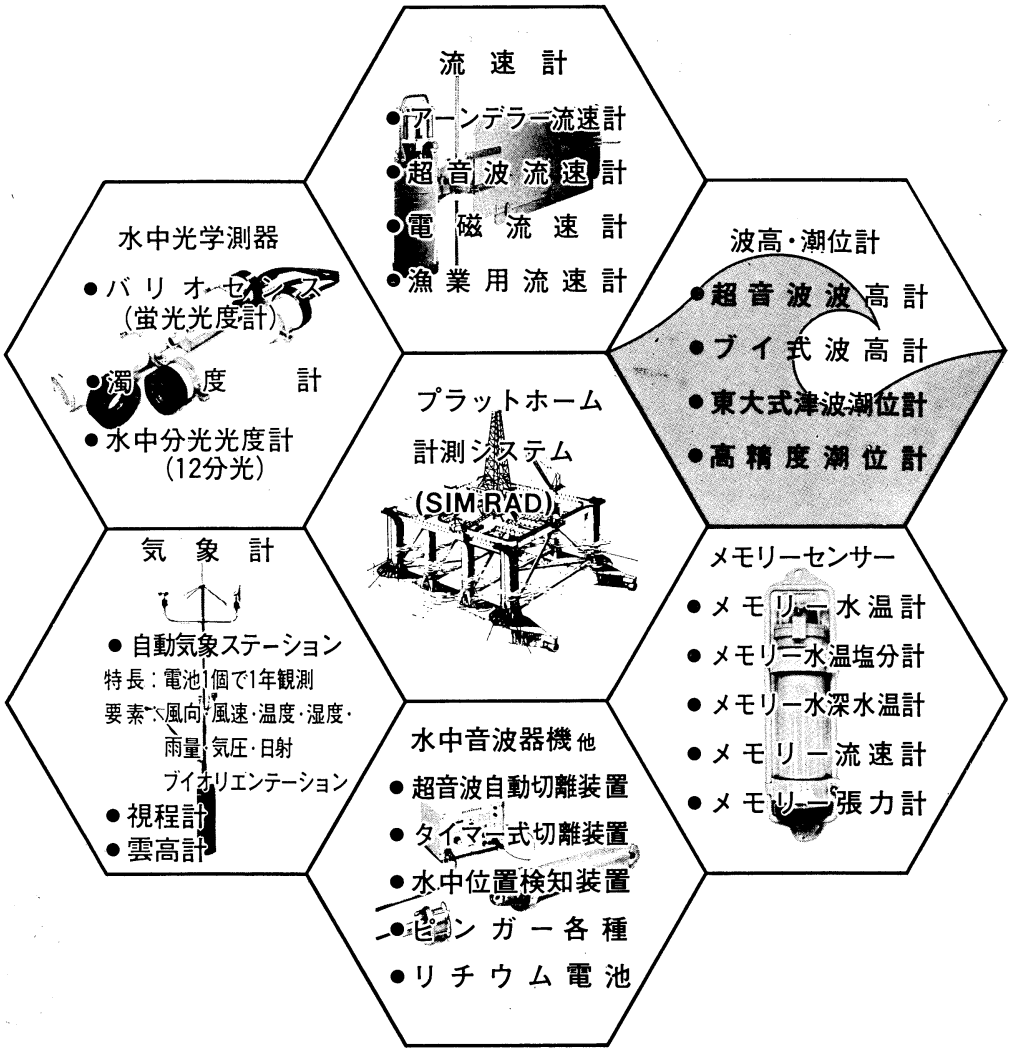

株式会社 ユニオン・エンジニアリング
本　社　神戸市中央区海岸通3丁目1－1
〒650　KCCビル4F　TEL078-332-3381(代)
東京支店　東京都中央区銀座7丁目18
〒104　銀座スカイハイツ602号　TEL03-543-5399

INDUCTIVE SALINOMER MODEL 601 MK IV

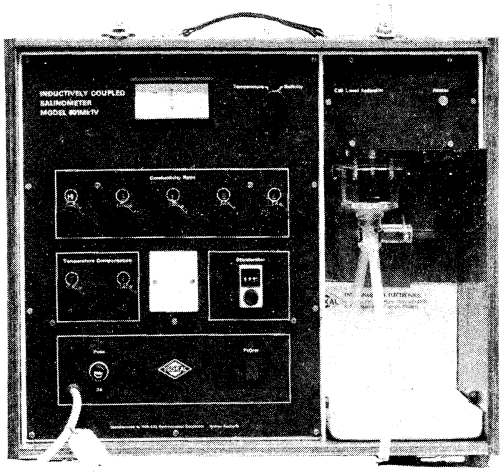

海水の塩分測定の標準器として，既に定評のあるオート・ラブ 601 MK Ⅲ の改良型で，小型・軽量・能率化した高精密塩分計です。試料水を吸上げる際に，レベル検出器により吸引ポンプと攪拌モーターとが自動的に切換えられます。温度はメーター指針により直示されます。

測定範囲	0～51 ‰ S
感　　度	0.0004 ‰ S
確　　度	±0.003 ‰ S
所要水量	約 55 cc
電　　源	AC 100 V 50～60 Hz
消費電力	最大 25 W
寸　　法	52(幅)×43.5(高)×21(奥行)cm

営　業　品　目

転倒温度計 ・ 水温計 ・ 湿度計 ・
採水器 ・ 採泥器 ・ 塩分計 ・
水中照度計 ・ 濁度計 ・ S-T計 ・
海洋観測機器・水質公害監視機器

株式会社 渡部計器製作所
東京都文京区向丘1の7の17
TEL (811) 0044 (代表)　〒 113

昭和57年8月25日 印刷
昭和57年8月28日 発行

う み

第20巻
第3号

定価 ¥1,200

編集者 高野健三
発行者 佐々木忠義
発行所 日仏海洋学会
財団法人 日仏会館内
東京都千代田区神田駿河台2-3
郵便番号:101
電話:03(291)1141
振替番号:東京5-96503

印刷者 小山康三
印刷所 英和印刷社
東京都文京区本駒込6-15-10
郵便番号:113
電話:03(941)6500

Tome 20 N° 3

SOMMAIRE

第 20 巻 第 3 号

目 次